ASSESSMENT OF GAS-SURFACE INTERACTION MODELS FOR COMPUTATION OF RAREFIED HYPERSONIC FLOWS

by

Jose Fernando Padilla

A dissertation submitted in partial fulfillment
of the requirements for the degree of
Doctor of Philosophy
(Aerospace Engineering)
in The University of Michigan
2008

Doctoral Committee:

      Professor Iain D. Boyd, Chair
      Professor Philip L. Roe
      Professor Kenneth G. Powell
      Associate Professor Hong G. Im

ACKNOWLEDGEMENTS

following colleagues for their help or otherwise "moral" support: John, Jon, Jeremy, Tom, Andrew, Leo, Chunpei, Anton, Alexandre, Andy, Dave, Quanhua, Wen-Lan, Matt and Justin. For other colleagues of Boyd's research group, I encourage them in their endeavors. Finally, I acknowledge and thank my parents, siblings and friends for their support.

TABLE OF CONTENTS

LIST OF FIGURES

Figure

LIST OF TABLES

Table

CHAPTER I

INTRODUCTION

1.1 Motivation

Computational simulation of rarefied hypersonic flows plays an essential role in efficient research and development of spaceflight. In the next few decades, spaceflight is expected to become more and more common through the resurgence of manned space exploration and the rise of commercial manned spaceflight. Most of these endeavors will involve traversing the altitude of 100 km above mean sea level. This is an internationally accepted boundary at which spaceflight begins, known as the Kármán line [*FAI* (2003), *Córdoba* (2004)]. It represents the altitude at which sustained aerodynamic lift for cruising flight requires a velocity greater than orbital velocity. The Kármán line is the altitude that the Ansari X PRIZE winner needed to transcend, twice within two weeks [*X PRIZE* (2006)]. The Ansari X PRIZE competition helped to stimulate current commercial reusable launch vehicle (RLV) development efforts. The RLV is considered a milestone toward the ushering in of the potentially lucrative space industry [*Collins* (1990); *DePasquale et al.* (2006)]. Examples of services that would benefit from commercial RLV technology are tourism, package delivery and transoceanic business travel. The National Aeronautics and Space Administration (NASA) and the European Space

Agency (ESA) have recognized the significance of commercial RLV technology and are now playing an active role in stimulating this industry [*Butterworth* (2007)]. In space exploration, NASA is working on sending people back to the Moon and then onto Mars [*Wilson* (2007)]. These manned space exploration activities will be accompanied by the continued servicing of the International Space Station and the manned space ambitions of other national space agencies, such as the Chinese National Space Administration.

Rarefied hypersonic flow appears in spaceflight during critical maneuvers at suborbital altitudes, altitudes near and above the Kármán line but lower than orbital. The flow is rarefied because the associated air density is so low, that the flow can no longer be considered a continuum. The flow is hypersonic because the air density is sufficient to transmit sound waves and the vehicle speed is many times the speed of that transmission. The suborbital spaceflight maneuvers must be handled carefully, particularly for manned flight, because of the threat of an uncontrolled entry into the atmosphere. These maneuvers include atmospheric entry, aero-assist orbit transfer and atmospheric skip. The entry and aero-assist maneuvers can be assisted using auxiliary deceleration devices called ballutes. Related flow conditions, which are rarefied but not necessarily hypersonic, also appear in rocket plumes for suborbital boost, orbit transfers, and in-orbit maneuvers such as spacecraft rendezvous and space station docking. In addition, these flow conditions appear in the associated windtunnel tests with purposes ranging from basic research to space vehicle design.

The knowledge for designing RLV's and other spacecraft is gained from a combination of theory and experiment. Because of the near-orbital velocities generally experienced in suborbital spaceflight there is significant expense and danger associated

with flight and windtunnel testing. These factors are in part mitigated by computer simulation. Computer simulation alone does not obviate the need for physical experimentation, but it can greatly reduce the amount of such experimentation. Although computational simulation of rarefied hypersonic flow and related conditions have been under development for over forty years, there are still many areas where improvements can be made, from practical to fundamental theoretical considerations. In particular, this thesis ultimately focuses on the assessment of numerical models governing the interactions between gas molecules and solid surfaces. Gas-surface interactions are not well understood for rarefied hypersonic conditions, although various models have been developed. For inert, low speed and high density applications, the gas molecules fully accommodate kinetically and thermally with the solid surface, that is, they achieve equilibrium with the surface within microscopic time scales. The assumption of full gas-surface accommodation is not generally valid for rarefied gas flows because of fewer intermolecular collisions above the surface, and thus, fewer reflected molecules that are redirected toward the surface by an intermolecular collision. In addition, for near orbital velocity flows, partial accommodation occurs because of the greater chance that an incident molecule at a higher kinetic energy will escape the surface after its initial encounter with the surface. These interactions govern the transfer of momentum and energy from the gas to the solid surface; and hence, directly affect the aerodynamic forces on the surface. Consequently, the aerodynamics and stability of a suborbital spacecraft are sensitive to the level of gas-surface accommodation. Thus, continued improvement of gas-surface interaction models enables improved suborbital and orbital flight vehicle design and analysis.

In the remainder of this introductory chapter, an overview of computational hypersonic flow research is presented to place in perspective the significance of the kinetic methods, to which gas-surface interaction models apply. The overview begins with a general review of hypersonic flow research; and then, it covers the computational analysis methods while providing an assessment of the present state-of-the-art. Details of the particular numerical method of analysis employed in this thesis are deferred to Chapter 2; in addition, details of gas-surface interaction models are deferred to Chapter 5. After the overview of computational hypersonic flow research, the objective and overview of this thesis are laid out.

1.2 A History of Hypersonics Research

When a flight vehicle is traveling many times faster than the ambient speed of sound, the gas medium flowing past the vehicle is said to be hypersonic. Relative to the vehicle, a hypersonic gas flow travels near and above five times the ambient speed of sound, i.e. Mach 5. The regime of hypersonic flow is not demarcated by a precise Mach number because it appears gradually with an increasing influence of the flow physics associated with faster flow compression. Although Newtonian flow calculations of hypersonic flow appeared in the literature as early as 1931 [*Anderson* (1984)], the initial wave of interest in hypersonics, the general study of hypersonic flow, is associated with the introduction of rocket flight during the late 1940's and the early 1950's. Since the first wave of interest, the number of publications about hypersonics has unsteadily increased, like the stock market, as shown in Fig. 1.1. This graph is obtained from the *Engineering Village* (2007) data base and shows the history of the number of documents published annually, which contain the word "hypersonic" in either the title, the abstract or the subject

description. The data base considers conference papers, journal papers, thesis reports and books. Since 1948, the total number of such documents is 11,892. Although the data base does not contain all engineering documents ever published, it does provide an adequate statistical sample for representing the full population trends.
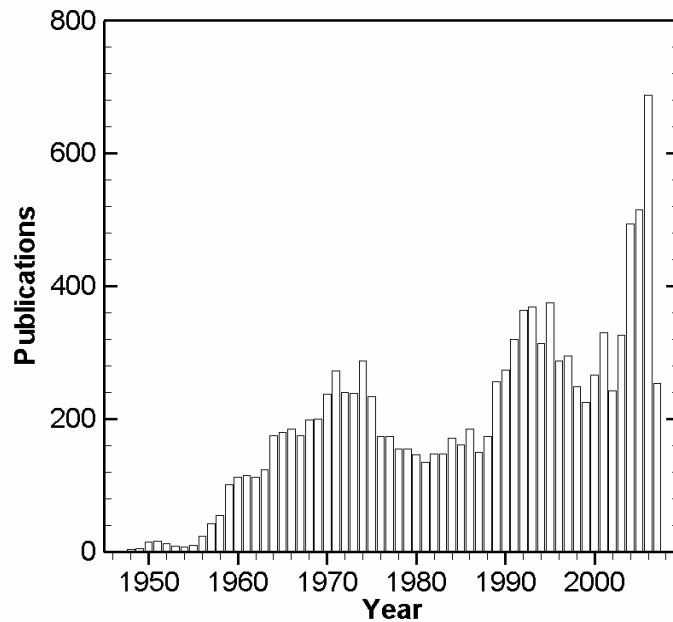
Figure 1.1   History of documents containing "hypersonic" in the title, abstract or subject [*Engineering Village* (2007)]

Figure 1.1 shows an increase in publicly published hypersonics research in the late 1950's and early 1960's. This increase can be attributed to the dawn of the space race between the Soviet Union and the United States, which was instigated by the arrival of space faring rocketry and emphasized 50 years ago by the first man made satellite, Sputnik of the Soviet Union. The increase in publications continues until 1970, where the number of publications hits a plateau. Then, a recession in hypersonics research occurs

5

from the late 1970's to the late 1980's. At this time the space race has ended; hence, the recession reflects the general reduction in the political support for space exploration after the completion of the 1960's space race marked by the achievement of manned missions to the moon by the United States. Nevertheless, hypersonics research is sustained above early 1960's levels during the recession. A part of this sustenance can be attributed to the lowering costs associated with maturing computational methods. This is reflected by the increasing percentage of hypersonics publications involving computational analysis as illustrated in Fig. 1.2. Another part of the sustained output of hypersonics publications can be attributed to the development of the Space Shuttle [*Heppenheimer* (1999)] and to efforts outside the United States to develop a space transportation system on par with the
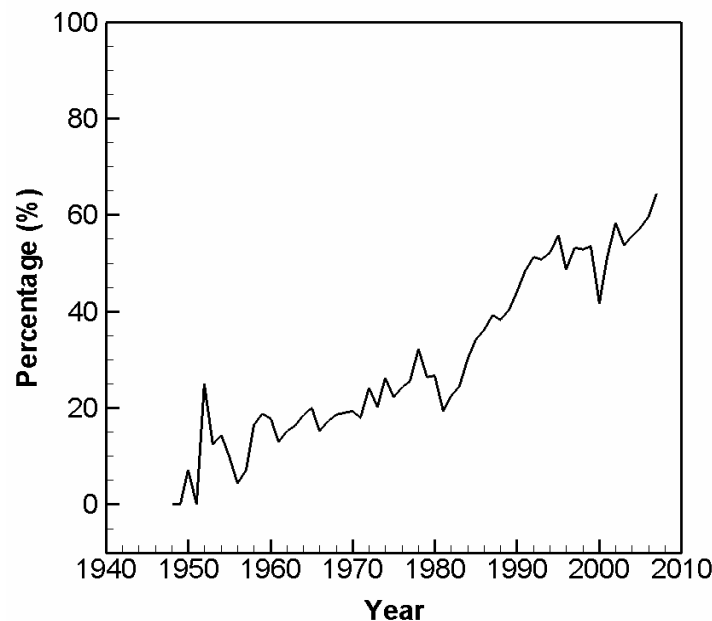
Figure 1.2 **Percentage of documents of Fig. 1.1 containing "computation", "numerical" or "simulation" in the title, abstract or subject [*Engineering Village* (2007)]**

6

Space Shuttle, namely, the French Hermes [*Coue* (2003)] and the Soviet Buran [*Pesavento* (1995)]. The end of the recession in hypersonics research can be attributed to the 1986 US state of the union address given by President Reagan, where he promoted the development of a hypersonic cruise vehicle [*Reagan* (1986)] for defense and commercial applications. This message evidently had a global impact, as the development of the Hermes spaceplane, which had been on the drawing boards since the late seventies by the French space agency, was revived in 1986 to be part of a European space transportation system [*Cazin* (1989)]. In addition, Russia had responded with the development of its own hypersonic cruiser [*Poukhov* (1993)]. This wave of hypersonics research begins waning in the mid 1990's. The reduction in hypersonics research can again be attributed to loss in political interest, this time, due to failures in the ambitious projects and escalations in their respective costs. Nonetheless, the output in hypersonics documents never dips below late 1960's levels. In the latter half of the 1990s, the sustained research can be attributed mostly to further lowering of costs associated with maturing computational capabilities, as reflected by the continuing rise in the percentage of hypersonics publications involving computational analysis shown in Fig. 1.2. This attribution is backed by the fact that the associated windtunnel and flight testing costs did not have a lowering trend and the political climate did not foster ambitious hypersonics developments. Further along the time line, Fig. 1.1 shows a third escalation in hypersonics research occurring after the Columbia Orbiter disaster of 2003. This is accompanied with a continuing rise in the percentage of papers involving computational analysis, an increase of 10% every 10 years, illustrated in Fig. 1.2. If this trend continues, then by 2020, 70% of publications about hypersonics will involve computational

analysis. Thus, the publications history reveals that the level of hypersonics research, based on the number of publicly published papers on hypersonics, reflects the global political climate, failures and advances in spaceflight programs, and the state-of-the-art in research and development technologies. In particular, computational capabilities are seen to play an increasing role in hypersonics research.

1.3 Computational Methods for Hypersonic Flow

The computational capabilities in hypersonics research are given by the existing state-of-the-art in computer technology and in the computational methods. In this section, an overview of computational methods in hypersonic flow analysis is given to place in perspective the relevance of the kinetic methods.

1.3.1 Pre electronic digital computer methods

The earliest computational methods of hypersonic flow research were based on approaches with limited applicability. These methods either drew upon existing theories, by modifying them to suit hypersonic flow conditions, or on experimental data to form an empirical formulation. They are of this nature because they were exploited during the first wave of interest in hypersonic flow, which occurred before digital electronic computing technology had come of age. These methods include, but are not limited to, the Newtonian method, blast wave theory, inviscid compressible flow theory, laminar boundary layer theory and empirical correlations. A review of these methods is given by the books of *Hayes and Probstein* (1959) and (1966), *Anderson* (1989) and *Rasmussen* (1994). Here they are only mentioned in passing in order to lay out the general hypersonics research background. The Newtonian method, which is the earliest and most

famous of these methods, dates back to 1931 when *Epstein* first applied it to hypersonic flow. A modification to this method, making it empirical, was developed by *Lees* in 1955 and is discussed in Chapter 3. Figure 1.3, which is taken from *Cox* (1959), illustrates the limited regions over a blunt slender body where some of these early methods apply. In this example, three methods are employed compositely to approximate the pressure distribution over a blunt slender cone. The region between the shockwave and the surface is here called the shock layer. One major reason these solutions are approximate is that they do not account for viscous interaction, the interaction between the boundary layer and the shock wave, e.g. the effects of the boundary layer on the shock layer. During this era, empirical correlations enabled the consideration of viscous effects by using hand calculations. For example, the drag coefficient of a blunt slender cone is calculated by using an equation fit to experimental data, which accounts for viscous interaction effects [*Whitfield and Griffith* (1964)].
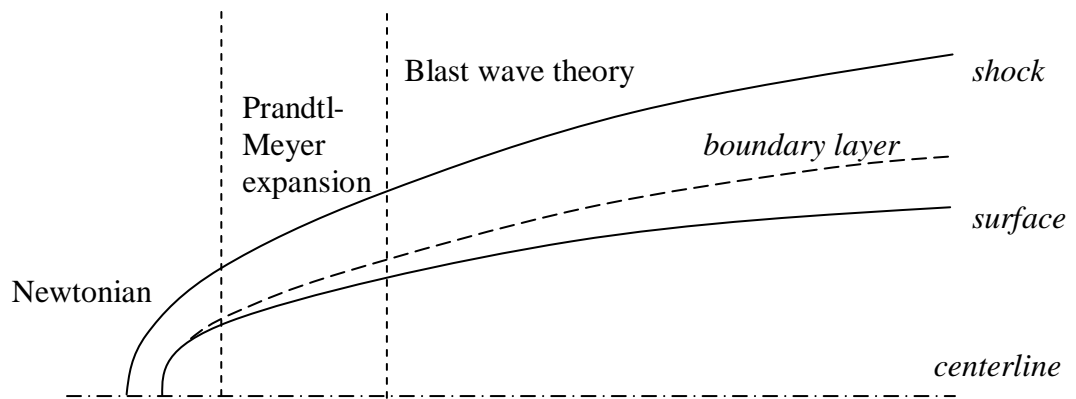
Figure 1.3   Regions of applicability of early numerical techniques for computing pressure distribution over a blunt slender body in hypersonic flow [*Cox* (1959)]

In order to examine heat transfer, the early hypersonic research subscribes to the stagnation point heat transfer solution of laminar boundary layer theory [*Fay and Riddell* (1958)]. Laminar boundary layer theory is also used to estimate the effects of chemical reactions within the shock layer [*Linen* (1962)] on the aerothermodynamics of an idealized flow geometry. In addition, correlation equations are developed to determine stagnation point heat transfer to blunt bodies of revolution with a specified velocity and nose radius [*Detra et al.* (1957)]. Correlation equations such as this enable rapid design estimates. Finally, to model nonequilibrium effects, there are extensions to the equilibrium models. For example, *Freeman* (1958) provides an addendum to Lighthill's ideal dissociating gas model in an effort to account for chemical nonequilibrium.

1.3.2 Continuum computational methods

To overcome the limitations of the early methods, the development of direct solutions to the fundamental conservation equations of fluid flow is desired. This is made practical with digital or transistorized computer hardware and an efficient programming language, which did not arrive until the late 1950's [*Ceruzzi* (2003)]. The maturing of the transistor and the integrated circuit inevitably brought forth the development of high level programming languages; the most popular, from this time, being FORTRAN, which has descendant forms still widely used today. Prior to this time, numerical solutions to partial differential equations were limited to basic mathematical forms, such as the Laplace equation; however, it was then that the mathematical tools behind computational fluid dynamics (CFD) were established by the pioneering efforts of various scientists. A historical perspective on these efforts is presented by *Anderson et al.* (1984). What is notable here is the relevance of computer technology in the development of CFD

solutions. For hypersonic flow problems, this development encompasses a spectrum of flow conditions, which in terms of the advancing complexity ranges from inviscous continuum to nonequilibrium rarefied conditions.

Regarding the continuum computational methods for hypersonic flow, accounts are found in the books by *Anderson* (1989), *Anderson et al.* (1984) and *Rasmussen* (1994), and the review paper by *Cheng* (1993). In brief, it is seen that the Navier-Stokes (NS) equations provide the framework for most of the continuum analysis. In order to solve the NS equations, various numerical methods are available. For a review of the numerical methods refer to *Hirsch* (2007). Because of the complexity of the NS equations, various simplified forms of the equations are developed. Relevant to hypersonic flow, these include the Euler equations, the parabolized Navier-Stokes (PNS) equations and the viscous shock layer (VSL) equations. The Euler equations provide estimations of shock curvature and pressure distributions for hypersonic flow problems. They are suited for code development; for example, *Henderson and Menart* (2006) used the Euler equations to examine equilibrium air chemistry procedures for a Navier-Stokes code. When coupled with boundary layer equations, the Euler equations provide suitable results for laminar conditions with weak viscous interaction [*Mundt* (1992)]; these conditions are associated with moderate to low altitude windward blunt body flows. The PNS and VSL equations are more general and necessary for conditions with strong viscous interaction or fully viscous shock layers. The PNS equations are suitable for shock layer flows where the inviscid portion is primarily supersonic, for example, the windward flow field around slender bodies. The VSL equations are applicable to shock layers with significant

subsonic flow, such as the windward flow against a blunt body. These simplified sets of NS equations are not suitable for handling streamwise flow separation and turbulence.

In addition to the general problem of viscosity there is the related problem of turbulence, which appears in a broad range of high Reynolds number applications. While the NS equations are adequate for accounting for turbulence, using them directly to calculate turbulence, which is known as direct numerical simulation (DNS), is intractable for most practical applications; and thus, extensive modeling is employed. Turbulence modeling is a broad topic which contains, as a sub-topic, simplifications to NS solutions. For a general understanding of the subject, a host of text books are available, such as *Pope* (2000). A recent review of engineering turbulence models for hypersonic flows is provided by *Roy and Blottner* (2006). An example of turbulence in hypersonic flow is a Mars entry space capsule analysis, presented by *Brown* (2002), which indicates that transition to turbulence occurs at the shoulder of the space capsule under continuum conditions.

The NS equations also provide the framework to model certain nonequilbrium conditions. There are various general flow phenomena classified as nonequilibrium. One major class is thermal nonequilibrium, which occurs when the translational, rotational and vibrational temperatures are not all equal. Another class is chemical nonequilibrium, which occurs when there is a finite rate of change in the chemical composition of the gas flow. Chemical nonequilibrium in hypersonic flow is driven by various types of reactions including dissociation, exchange, recombination and ionization reactions. In order to extend the NS equations and their simplified forms for handling thermal and chemical nonequilibrium flow, additional equations are added to the basic system of conservation

equations [*Park* (1990)]. For thermal nonequilibrium there is an additional energy equation associated with each energy mode temperature. For chemical nonequilibrium, there is an additional mass conservation equation associated with each distinct chemical species undergoing a change in concentration.

1.3.3 Kinetic computational methods

Suborbital hypersonic flight vehicles, particularly near and above the Kármán line defined in Section 1.1, experience conditions where the NS equations are erroneous in major regions of the flow field surrounding the vehicles, mainly because of extremely low gas density. In these regions, the dynamics of molecular motion need to be taken into account; hence, the flow is said to encounter continuum breakdown. To accurately describe a discrete gas, it is necessary to harness a molecular description of fluid dynamics. Before proceeding, a few points on related terminology are made here. The term "kinetic" is often used synonymously with "molecular". These descriptions indicate that intermolecular collisions or interactions are taken into account in some form. In addition, because the description of relaxation to equilibrium is generally important when describing fluid dynamics kinetically, the term "nonequilibrium" is also used synonymously with "molecular". Finally, for low gas density conditions, the application of these terms: "kinetic", "molecular" and "nonequilibrium" to gas flows are also used interchangeably with the term "rarefied".

There are a few classes of computational approaches for examining molecular gas dynamics. One class is aimed at solving the Boltzmann equation, the standard governing equation of kinetic theory [*Cercignani* (2000); *Gombosi* (1994); *Vincenti and Kruger* (1965)]; for a historical perspective on kinetic theory see *Gombosi* (1994). In its general

form, the Boltzmann equation is a non-linear integro-differential equation in terms of a function describing the distribution of molecules in position and velocity space. Hence, the Boltzmann equation is solved numerically in practical applications. As early as 1955, Nordsieck developed a Monte Carlo method to evaluate the collision integral of the Boltzmann equation; this method was further developed by various researchers including *Yen* (1984). According to *Ivanov and Gimelshein* (1998), newer methods have appeared that preserve conservative variables by using special quadrature for the collision integral. For example, in 1994 *Rogier and Schneider* published a solution method that uses a finite-difference scheme to evaluate the collision integral and a finite element scheme to evaluate the transport dynamics. This approach is classified as a discrete velocity model of the Boltzmann equation; a solution method that has yet to fully mature [*Cercignani* (2000)].

A second class of approaches to compute nonequilibrium gas flows involves solving simplified forms of the Boltzmann equation, which are able to handle a greater extent of nonequilibrium than the NS equations. Although the NS equations were developed before the Boltzmann equation [*White* (1991); *Gombosi* (1994)], the NS equations are derivable from the Boltzmann equation. This is performed by employing a truncated Chapman-Enskog expansion of the velocity distribution function that has only a small deviation from equilibrium [*Vincenti and Kruger* (1965)]. Consequently, the ability of the NS equations to handle nonequilibrium flow is limited; however, other simplifications of the Boltzmann equations exist that allow greater deviations from equilibrium. Simplified forms that have appeared in aerospace applications include the Bhatnagar-Gross-Krook (BGK) equation [*Vincenti and Kruger* (1965); *Burt* (2006)], the Burnett equations and

Grad's moment equations [*Cheng and Emanuel* (1995); *Chen et al.* (2007)]. While these equations involve solutions with less computational expense than the solution of the Boltzmann equation, their computational expense is generally greater than solution of the NS equations. In addition, their range of applicability is nevertheless limited and they have yet to gain wide spread use.

A third class, called molecular dynamics, involves tracking every molecule of a specified system by using the fundamental laws of physics. This approach was introduced by *Alder and Wainwright* in 1958 and has since been substantially developed. The molecular dynamics approach is employed for molecular scale simulations. When used by itself, molecular dynamics is prohibitively expensive for vehicle aerothermodynamic analysis; however, in relation to aerothermodynamics, it has found an auxiliary use. In 1999, *Yamanishi et al.* employed molecular dynamics for generating a gas-surface interaction database for Monte Carlo simulation.

A fourth class involves kinematically tracking a representative system of molecules, while using probability to select intermolecular collisions. This approach was not developed from the Boltzmann equation; however, it uses the same physical principles behind the Boltzmann equation [*Bird* (1994)]. In 1963, *Bird* introduced an early form of the approach that eventually developed into what is now known as the direct simulation Monte Carlo (DSMC) method [*Bird* (2001)]. The DSMC method has become the standard approach to model flows with continuum breakdown at spatial scales relevant to suborbital space flight aerothermodynamic analysis. Although the DSMC method has been under development for over forty years, there are still many areas where improvements can be made, from practical to fundamental theoretical considerations. It

forms the basis for the computational analysis in this thesis and is further discussed in Chapter 2.

1.4   Objective and Overview

This thesis research focuses on the DSMC method for the analysis of rarefied hypersonic flow aerothermodynamics relevant to the advancement of spaceflight. Several aspects are examined, from the analysis of aerodynamic coefficients to an assessment of gas-surface interaction models. The presentation of the research begins in Chapter 2 with an introductory description of the DSMC method and the particular implementation employed in this work, called MONACO. Then, a description is given of the grid-generation procedures and post processing.

Having described the DSMC method and the associated simulation procedures, the research analysis begins in Chapter 3 with the assessment of aerodynamics modeling using data from rarefied hypersonic windtunnel tests of small scale entry vehicle models. In this analysis, procedures to determine aerodynamic coefficients from MONACO simulations are validated against certain experimental data and an independent DSMC code.

In Chapter 4 the analysis continues with a sensitivity study of aerothermodynamics predictions for the Apollo 6 capsule, at the 110 km altitude return trajectory point. This involves the examination of inter-gas chemistry, a radiative equilibrium wall boundary condition, and partial gas-surface accommodation. At this altitude it is found that changes in the gas-surface thermal accommodation significantly affect the aerothermodynamics; the addition of surface radiative equilibrium condition does not significantly affect the

aerothermodynamics; and the inclusion of chemistry does not significantly affect the aerothermodynamics.

The conclusion to the sensitivity study motivates the detailed examination of gas-surface interaction models presented in Chapter 5. This entails a review of existing models and the analysis of two common models in use with the DSMC method: the Maxwell model and the Cercignani, Lampis and Lord (CLL) model. The two models are scrutinized with the help of relatively recent windtunnel test measurements of boundary layer velocity profiles over a flat plate in rarefied hypersonic flow. The flow is analyzed parametrically with various levels of gas-surface accommodation. The resulting effects on velocity and temperature shock layer profiles and on surface friction and heating are examined. Both models are found to yield similar results; however, the CLL model is physically more realistic and is not significantly more expensive computationally. After analyzing the gas-surface interaction models, the effects of seeded iodine in the windtunnel tests are examined. These effects are found to be insignificant. Finally, the extent of translational and rotational nonequilibrium within the boundary layer of the flat plate is examined by molecular velocity statistics and distribution shapes, and profiles of translational and rotational temperature. Significant thermal nonequilibrium is found near the surface and near the leading edge of the flat plate.

After Chapter 5, appears the thesis conclusion in Chapter 6. Here the important results and conclusions throughout the thesis are summarized. Finally, areas of further research prompted by this thesis are suggested.

CHAPTER II

GENERAL SIMULATION PROCEDURES

2.1　Overview of the DSMC Method

The direct simulation Monte Carlo (DSMC) method was first developed and applied by *Bird* in 1963. It has recently been surveyed by *Oran et al.* (1998) and by *Bird* (2001) himself. It is a computational simulation method grounded in kinetic theory and stochastic processes. It involves kinematically tracking a representative system of molecules, while using probability to select intermolecular collisions and to process boundary conditions. Thus, it is suitable for describing dilute gas flows. A gas is dilute when the mean molecular spacing $\delta_{spacing}$ is at least an order of magnitude greater than the characteristic molecular diameter $\delta_{diameter}$. In a dilute gas, the molecular motions are not significantly affected by intermolecular field forces and collisions between two molecules are quickly forgotten by each molecule. This condition results in molecular chaos, a fundamental assumption behind the Boltzmann equation and the DSMC method. The condition of molecular chaos states that the probability of finding two molecules at the same position and velocity is equivalent to the product of each molecule's probability of being found in that position and velocity [*Bird* (1994)]. In DSMC, this condition allows the treatment of collisions independent of molecular motions within suitable intervals of

space and time; namely, the computational cell size Δs must be less than the local mean-free-path distance λ traveled by molecules between successive collisions and the reference time step Δt must be less than the local mean collision time τ, the mean time of flight spent by molecules between successive collisions. Note that these criteria depend on the knowledge of the local mean values, which vary slightly in a steady state due to the statistical nature of the simulation. In regions of large macroscopic gradients, *Bird* (1994) generally recommends $\Delta s < \lambda / 3$ and $\Delta t << \tau$.

The DSMC method tracks a representative system of simulation molecules through a computational domain while simulating collisions stochastically. The system is merely representative because of the prohibitive cost of performing a simulation with the large number of molecules in a real situation. A typical computer workstation's central processing unit (CPU), such as a 1.5 GHz class CPU, with 1 gigabyte (GB) of random access memory (RAM), can efficiently process a DSMC simulation with up to about 3×10^6 particles. Even at the typical altitude of the International Space Station, 385 km [*Bond* (2002)], the number density of the atmosphere is on the order of 10^{14} molecules / m^3, according to the 1976 United States (US) Standard Atmosphere table [*Lide* (2007)]. At the edge of the atmosphere, ~100 km altitude, where the DSMC method is commonly applied for spacecraft aerothermodynamic analysis, the number density is five orders of magnitude greater at $\sim10^{19}$ m^{-3}. It is clear that we cannot process more than a very small fraction of the molecules present.

During each time step, all particles are translated according to rectilinear kinematics, then certain particles are probabilistically selected for collision to match the correct collision frequency according to kinetic theory. Post-collision velocities are determined

from conservation of energy and momentum and the assumption of isotropic scattering. The intermolecular collisions and associated molecular energy exchange are processed with special subroutines in a DSMC code. Optionally, other subroutines are used to manage chemical reactions, ionization and radiation. *Ivanov and Gimelshein* (1998) provide a review of physical models used in DSMC relevant to rarefied hypersonics. Here a brief overview on the topics relevant to this thesis is presented. The intermolecular collisions are modeled using simplified intermolecular field potentials in order to maintain feasible computational expense. Various models have been developed, each having advantages and disadvantages; the best use of a particular model being application dependent. For computing molecular energy exchange, among translational, rotational and vibrational modes, energy exchange probability models are used. Most of these models are based on the Larsen-Borgnakke (LB) phenomenological model [*Borgnakke and Larsen* (1975)]. For rotational energy exchange, continuous and quantized energy spectrum LB models are available. The quantum or discrete rotational energy models are particularly valuable for low temperature simulations. For vibrational energy exchange, discrete energy models are necessary to provide accurate and physically realistic results. The chemical reaction procedures are based on collision theory from physical chemistry. The original procedures [*Bird* (1979)] used a reaction probability that depended only on the total collision energy (TCE) and is called the TCE model. A modification to these procedures considers coupled vibration-dissociation and called the vibrationally favored dissociation (VFD) model [*Haas and Boyd* (1992)]. For an overview on the effects of ionization and thermal radiation in the gas flow, see for example, *Ivanov and Gimelshein* (1998).

At the domain boundaries are inflow, outflow, symmetry and wall surface conditions that regulate the transport of molecules into and out of the simulation domain. At the inflow boundaries, Maxwellian distributions at the local boundary temperature and velocity are typically employed to insert the molecules into the simulation domain. At the outflow boundaries, a vacuum or background pressure condition can be specified to handle the removal of molecules. The symmetry boundaries assume a mirror image on the other side, thus, they reflect molecules specularly without changing their kinetic and internal energy. Finally, surface boundary conditions require specialized routines to model the gas-surface interactions, and optionally, gas-surface catalysis, surface radiation heat transfer and surface conduction heat transfer.

The ratio of mean-free-path λ to characteristic length l is called the Knudsen number and is used to define flow regimes and to gauge for continuum breakdown. When l is a characteristic dimension of a flight vehicle, such as the body length, the Knudsen number describes the overall vehicle flight condition and is called the global Knudsen number Kn. The global Knudsen number provides definitions for overall flow conditions as follows: continuum $Kn < 10^{-4}$, transitional rarefied $10^{-4} < Kn < 10^{-1}$, rarefied $10^{-1} < Kn < 10$ and collisionless $Kn > 10$. These definitions are indicative of the majority of the gas flow behavior and have pragmatic utility in setting up flow simulations. DSMC can describe gas flows throughout the entire spectrum of global Knudsen number, provided that the flows are dilute. However, DSMC is best suited for the transitional and rarefied flow conditions. These are conditions the Navier-Stokes (NS) equations cannot simulate because of continuum breakdown and are the conditions of primary concern in this thesis. For the continuum regime, DSMC is inordinately expensive and the NS equations are

quite adequate. For the free molecular flow regime, the collisionless Boltzmann equation provides more efficient results for simple geometries. When l is the length scale of a macroscopic gradient, the Knudsen number describes the local flow condition and is suitable for gauging continuum breakdown. The gradient length local Knudsen number is used to partition computational domains in simulations using continuum and kinetic methods in separate regions. For details on using gradient length local Knudsen numbers to gauge continuum breakdown and apply them to hybrid computational methods refer to *Wang and Boyd* (2003) and *Schwartzentruber et al.* (2007).

2.2 Description of the MONACO DSMC Code

This study employs a general, cell-based implementation of the DSMC method called MONACO [*Dietrich and Boyd* (1996)]. The name is not an acronym; rather, it serves as a reminder of a mathematical concept that it employs, Monte Carlo simulation. Since its inception, this particular code has been developed by a number of researchers including *Kannenberg* (1995), *Sun* (2003), *Wang* (2004) and *Burt* (2006). In the respective references, they provide additional descriptions of the DSMC method and MONACO. These researchers implemented the code for a spectrum of applications including rocket plume, micro scale airfoil and hypersonic windtunnel test analysis, and the development of hybrid continuum and particle methods. In this study, the code is employed to simulate space capsule reentry and rarefied hypersonic windtunnel tests. MONACO is written in C [*Deitel and Deitel* (2001); *Kernighan and Ritchie* (1988)] and can be executed on serial or parallel computer systems. The parallel procedures are encoded with the Message Passing Interface (MPI) [*Quinn* (2004)]. For defining the computational domain, MONACO employs structured or unstructured grids, with two or three spatial dimensions in National

Grid Project (NGP) format [*Thompson* (1992)]. Additionally, it provides the option of running two or three dimensional flow simulations, or axisymmetric flow simulations, with the appropriate grid type.

MONACO provides the option of using various procedures for handling the molecular physics, which deal with inter-gas collisions and chemistry, and gas-surface interactions. For gaseous intermolecular collisions, a near-field molecular potential model, described by a molecular shape, regulates the collision dynamics. Currently, the code gives the option of using either the variable hard sphere (VHS) model [*Bird* (1981)] or the variable soft sphere (VSS) model [*Koura* (1992)]. For rotational energy exchange, it uses the variable rotational energy exchange probability model, developed by *Boyd* (1990). For vibrational energy exchange it uses the variable vibrational energy exchange probability model, developed by *Vijayakumar et al.* (1999). The variability of the vibrational energy exchange model is optional, so that simulations can exclude it when it is known that the flow will not be vibrationally activated. MONACO also provides the option of employing chemical reaction procedures, regulated by the TCE or the VFD models, described in the previous section. For the gas-surface interactions, MONACO uses by default the Maxwell model and an isothermal wall temperature distribution.

For part of this thesis study, the wall temperature condition is modified to model a radiative equilibrium wall surface and the accommodation coefficient in Maxwell's gas-surface interaction model is divided among the translational, rotational and vibrational energy modes. A description of these modifications is given in Chapter 4. This thesis research also added the option of using the Cercignani, Lampis and Lord (CLL) gas-surface interaction model in lieu of the Maxwell model. The theoretical principles of both

gas-surface interaction models and their implementation into MONACO are presented in Chapter 5. Finally, the research motivated the addition of procedures to extract probability distributions and associated statistics of velocity at requested points in space or of reflected velocity at requested points on a solid surface, for each gas species involved in the simulation.

2.3   General DSMC Grid Generation Procedure

As with continuum CFD, the generation of the computational grid for DSMC in general plays a major part of the simulation procedure. The difficulty arises in optimizing the grid to minimize simulation expense while maintaining a grid that will result in an accurate solution. The optimization is desired for large simulations. It involves minimizing domain size and optimizing cell density. The former criterion is bypassed when the size of the domain is predefined by the problem, such as in certain internal flow problems. When the domain size is not predefined, a suitable estimate can be made through physical intuition about the flow behavior, consideration to any symmetry in the problem and consideration to the goal of the simulation. The estimate should be made larger than expected in order to contain the relevant flow phenomena, such as a diffuse bow shock about an entry vehicle, so that a well informed decision can be made about reducing the domain size. In the case of the diffuse bow shock, the freestream region need only be large enough to accurately generate the shock; the rule of thumb is to have at least five cells of freestream upstream of the known location of the beginning of the diffuse shock.

For optimizing the cell density in DSMC, the grid cells are distributed so that the spatial constraint, $\Delta s < \lambda$, previously described, is met in the limit as Δs approaches λ;

essentially by setting $\Delta s \approx \lambda$ throughout the computational domain. Because λ is not usually known throughout the flow field, it is estimated in order to generate the initial grid. Without additional information, a characteristic inflow mean-free-path λ_c, such as the freestream mean-free-path, provides a starting point. If the flow is known to expand in the simulation domain, then the cell sizes in the expansion region could be made larger than λ_c in order to reduce computational expense for the initial simulation run. Otherwise, a uniform distribution of cells with $\Delta s \approx \lambda_c$ provides an initial grid. The mean-free-path distribution of the initial simulation then provides the information to generate a grid with an optimum cell density. Usually, the second grid, called the adapted grid, provides a sufficiently efficient and accurate simulation for engineering analysis. The process of redistributing or adapting cells so that their sizes are similar to the local mean-free-path can be done automatically through a specialized computer code. However, when such a code is not available, the adaptation can be done manually with a reasonable success.

The entire process of optimizing the grid for minimal simulation expense can be automated in theory, however, at a significant cost: it requires integrating grid generation procedures into the DSMC code and adding specialized logic for domain size reduction. Integrated grid generation is difficult to develop to the same level of flexibility and efficiency as existing grid generation software, which have extensively optimized procedures and are able to handle automatic cell density adaptation to a given simulation output file [*Owen* (2007); *Ollivier* (2005)]. Full automation is difficult and unnecessary for single simulation cases needing only one iteration of grid adaptation; however, for studies involving: several slightly distinct simulations, complex steady flow problems requiring multiple iterations of adaptation or unsteady flow problems, automation of at

least the adaptation of cells merits pursuit. In this case, the problem of redistributing cells with optimum smoothness in an arbitrary domain can be avoided by limiting grid modifications to the division or synthesis of existing cells. This is pursued, for example by *Wu et al.* (2001). In continuum CFD, the grid optimization problem is distinct and has been given significantly more attention.

In this study, the simulation domains are adapted manually. Three dimensional grids are generated for the simulations studied in Chapters 3 and 4, and two dimensional grids are generated for the simulations analyzed in Chapter 5. For generating these grids, commercial software is employed because it provides consistent and efficient convergence. The particular program employed is *HyperMesh* (2004) as recommended by a research colleague [*Cai* (2005)].

To provide an example of grid adaptation, the grid generation process for the seeded iodine simulation, discussed in Chapter 5, is outlined here. This simulation involves the near-field rarefied hypersonic flow over a flat plate windtunnel test model. It has a specified inflow location from measured data, 2 mm upstream of a flat plate leading edge; however, the inflow height and the downstream domain size are undetermined. The initial simulation uses the domain dimensions displayed in Fig. 6 of the windtunnel test paper by *Cecil and McDaniel* (2005). This domain is divided into rectangular cells with sides Δs equal to the average inflow mean-free-path $\lambda_c = \lambda_{N2, \infty, \text{avg}}$ of the nitrogen: $\Delta s = 0.1$ mm $\approx \lambda_{N2, \infty, \text{avg}}$, as illustrated in Fig. 2.1 (a). This grid is comprised of 35,850 cells and is more than adequate for simulations which assume a pure nitrogen flow. However, for the simulation that includes the seeded iodine, the grid needs to be refined because the

boundary of region shown in Fig. 2.1 (b)
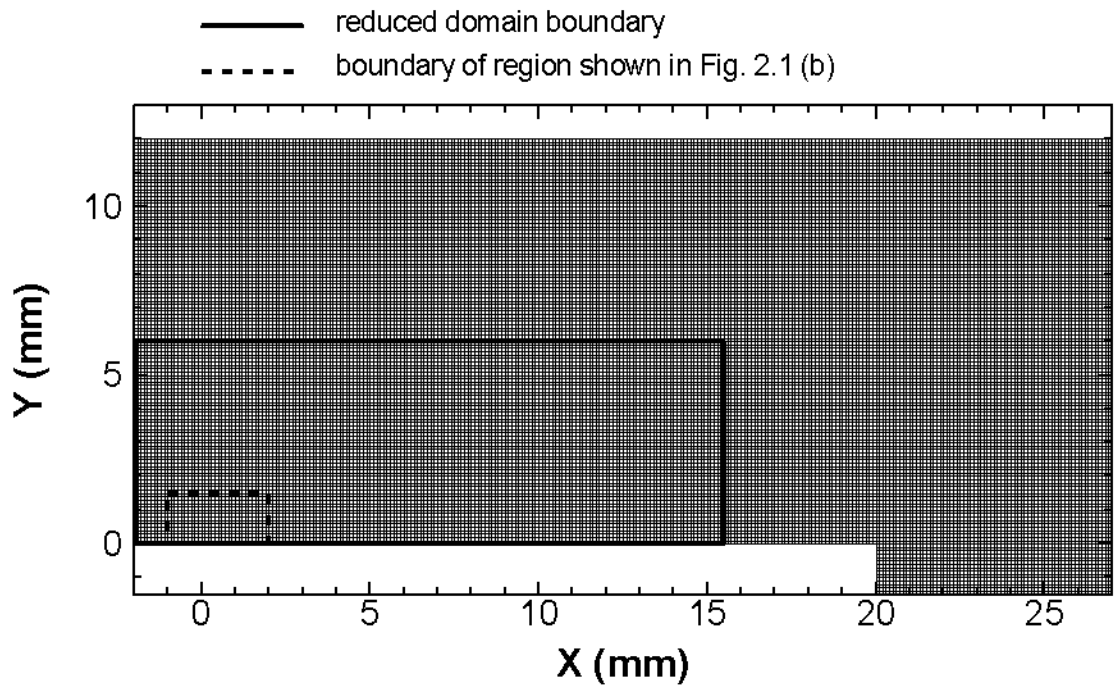
(a) *Initial Grid*
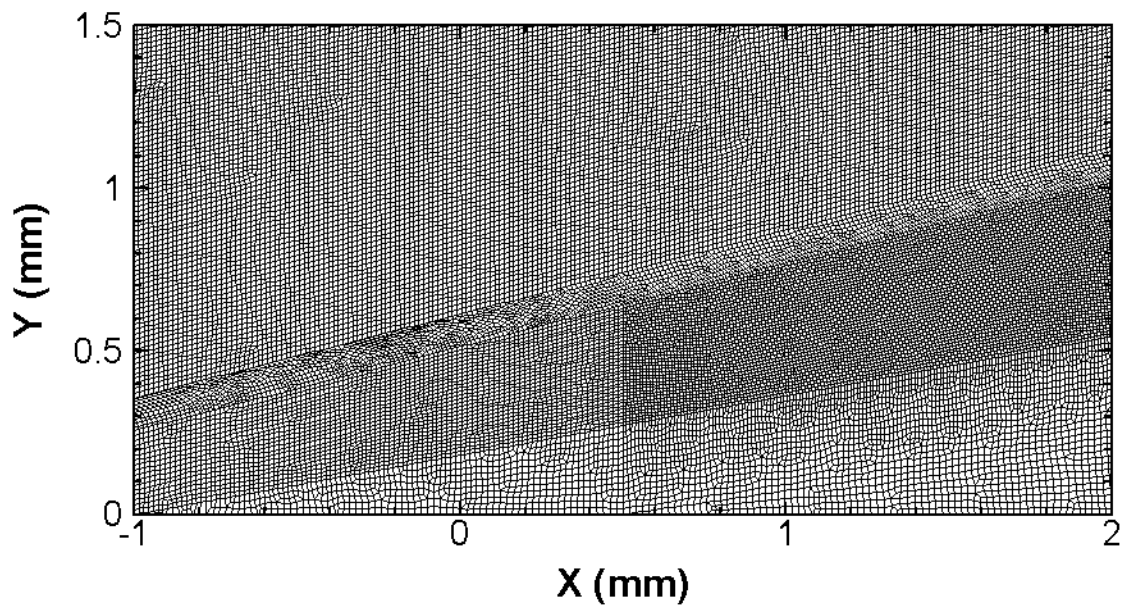
(b) *Close-up of Adapted Grid*

Figure 2.1   Computational grid generation for seeded iodine simulation

iodine mean-free-path is an order of magnitude smaller than the nitrogen mean-free-path. For the refined grid it is estimated that the number of simulation molecules is about 200 million. Hence, the domain size is reduced in order to maintain a reasonable computational expense. The simulation expense of the reduced domain is listed in Table 5.5 of Chapter 5. A mixed set of triangular and quadrilateral cells is used because it results in fewer cells and a smoother cell distribution. The mean-free-path adaptation is performed manually by dividing the domain into several sub-regions and defining the cell densities at the boundaries of each of these sub-regions. Figure 2.1 (b) illustrates a portion of the adapted grid. The entire grid has too many cells to distinguish their distribution within the page margins; hence, a close-up of the adapted grid is shown. The close-up shows a few sub-regions with cell densities matching at their boundaries. The sub-region containing the diffuse oblique shock has the greatest cell density because that is where the iodine mean-free-path is smallest. Behind the shock the flow expands and the associated the computational cell density is consequently lower.

2.4   Overview on Post Processing

A DSMC simulation begins with a transient period from the initial insertion of simulation molecules into the simulation domain. Eventually, for a steady state simulation, the collisional and other physical processes arrive at a statistical steady state. Thereafter, molecular properties are sampled in each cell at specified intervals of time steps and the running average or summation of each sampled property is monitored. When the uncertainties in the running averages are within satisfactory limits, the simulation is terminated. The MONACO DSMC code stores the cell averaged molecular

properties in an unformatted binary file called *MCsample.unf*. This file is converted into *Tecplot* (2004) format with the OXFORD post-processing program.

OXFORD provides the option of examining several of the field and surface properties. Some of the field properties are presented at various places throughout this thesis report. These include the mean-free-path, the translational, rotational and vibrational temperatures, the number density and the Mach number. To provide an example of how the field properties are extracted the equations for the translational temperature are presented. The translational temperature is computed by:

$$T_{tra} = \frac{1}{3}\left(T_{tra,x} + T_{tra,y} + T_{tra,z}\right) \tag{2.1}$$

where each component translational temperature is obtained using

$$T_{tra,i} = \frac{2\sum_s \frac{1}{2} MW_s X_s \overline{\xi'^2_{i,s}}}{R_u} \tag{2.2}$$

where R_u is the universal gas constant and the summation occurs over all species s. MW_s, X_s and $\overline{\xi'^2_{i,s}}$ represent the species molecular weight, mole fraction and mean square random molecular speed along direction i, respectively. Each mean square random molecular speed is determined by the identity

$$\overline{\xi'^2_{i,s}} = \overline{\xi^2_{i,s}} - \overline{\xi}^2_{i,s} \tag{2.3}$$

The set of molecular properties in each computational cell stored in *MCsample.unf*, includes $\sum_t \sum_r \xi_{r,t,i,s}$ and $\overline{\xi^2_{i,s}}$. $\sum_t \sum_r \xi_{r,t,i,s}$ represents the summation over all particles r and samples t at a particular computational cell of the species absolute molecular speed along coordinate direction i. This provides the information to extract $\overline{\xi}^2_{i,s}$ with the aid of

the relation:

$$\overline{\overline{\xi}}_{i,s} = \frac{\sum\limits_{t}\sum\limits_{r}\xi_{r,t,i,s}}{N_{sample}N_p} \tag{2.4}$$

where N_{sample} is the total number of samples taken at a particular cell and N_p is the mean number of simulation molecules in that cell during steady state.

Surface properties that appear in this thesis report, directly or indirectly, are the pressure p, the shear stresses τ_x, τ_y and τ_z, and the Stanton number St. The pressure and shear stresses are used to compute the aerodynamic coefficients of lift, drag and pitching moment: C_L, C_D and C_M, respectively. A further description on the calculation of the aerodynamic coefficients is given in Chapter 3. To provide an example of how the surface properties are extracted, the equations for the Stanton number are presented. The Stanton number is computed by

$$St = \frac{\dot{q}}{\frac{1}{2}\rho_\infty V_\infty^3} \tag{2.5}$$

where ρ_∞ and V_∞ are the freestream density and speed, and $\dot{q}$ is the surface heat flux. The heat flux is determined by

$$\dot{q} = \left(\sum\limits_{s}\overline{\Delta E_s}W_{p,s}\right)\frac{W_p}{\Delta t N_A A_{face}} \tag{2.6}$$

where $\overline{\Delta E_s}$ and $W_{p,s}$ are the species mean total energy transfer and particle weights, respectively. The set of molecular properties at each computational cell stored in *MCsample.unf* also includes $\overline{\Delta E_s}$. W_p, Δt, N_A and A_{face} are the global particle weight, global time step, Avogadro's number and the wall surface cell face area, respectively. In the simulations presented in this thesis, species particle weights are used only for the iodine simulation.

CHAPTER III

ASSESSMENT OF AERODYNAMICS MODELING AND WINDTUNNEL DATA

3.1 Background and Relevance

In the mid to late 1960's, the Apollo program motivated hypersonic windtunnel test studies of centimeter scale models in order to improve our knowledge of spacecraft reentry aerothermodyamics. Some of these windtunnel studies were performed at the Arnold Engineering Development Center (AEDC), Tennessee, in the von Karman Gas Dynamics Facility (VKF) and involved a low density, hypersonic, continuous-flow, arc-heated, and ejector-pumped windtunnel called VKF Tunnel L. One of these studies, executed by *Boylan and Potter* (1967), tested a handful of simple vehicle shapes, and compared the resulting windtunnel data with modified Newtonian and free molecular flow analyses. Because of the simplicity of the vehicle models and the adequacy of the documentation, this windtunnel test study is selected for numerical simulation in order to develop three-dimensional aerodynamic post-processing procedures. The aerodynamic procedures are validated by reproducing the modified Newtonian and free molecular flow results. Subsequently, the aerodynamic procedures are applied to DSMC results, and the DSMC aerodynamic results are compared with the windtunnel results. In addition,

similar numerical simulations are made of the VKF Tunnel L windtunnel tests of the Apollo Command Module [*Boylan and Griffith* (1968)]. These simulations provide a unique assessment that uses aerodynamic analysis within rarefied hypersonic flow conditions of the MONACO DSMC code.

In this chapter, the computer aerodynamic simulation study of the AEDC windtunnel tests described above are presented. First, a description is given of the Newtonian and free molecular flow analyses. Second, the three-dimensional aerodynamic analysis is formulated. Third, three-dimensional simulations of the blunted-cone model are presented. Fourth, three-dimensional simulations of the Apollo command module model are presented. Fifth, axisymmetric simulations are presented to help explain the disagreement between the Apollo windtunnel test results and the DSMC results. Finally, the aerodynamic assessment is summarized and conclusions are formulated about the numerical simulations and the windtunnel tests.

3.2 Analytical Flow Approximations

3.2.1 Relevance

Primitive modeling approaches often provide a stepping stone to the more sophisticated numerical approaches. The conceptual design process, computer program development, and theoretical analysis provide three reasons for using primitive modeling approaches. First, from a conceptual design perspective, primitive approaches provide initial estimates of vehicle performance from where a second design iteration may begin using more sophisticated and expensive methods. Second, from a program development perspective, the less sophisticated approaches provide simple functions to help develop auxiliary functions, such as aerodynamic coefficient integration procedures, that will

eventually be used with more complicated procedures. Third, from a theoretical analysis perspective, the less sophisticated theory often helps identify physical or numerical phenomena and their effects.

In the following sections, the modified Newtonian and free molecular flow primitive modeling approaches are described. They help develop procedures to compute aerodynamic properties from DSMC analysis of the windtunnel tests. The aerodynamic post-processing procedures are developed to expand our ability to evaluate modifications and additions of physical models to the MONACO DSMC code.

3.2.2 Modified Newtonian flow

Numerical models can be selected for gas dynamic simulation based on freestream speed. The AEDC windtunnel tests involved gas flow traveling at thousands of meters-per-second with respect to the vehicle. A Newtonian model for solids immersed in a gas flow is valid for inexpensive analysis of hypervelocity gases such as in the AEDC windtunnel tests. The Newtonian model can be used with a flat panel surface approximation to provide a simple numerical calculation to estimate the vehicle aerodynamic properties. The details on this approach are described in this section.

Over three centuries ago, Isaac Newton made propositions to determine the pressure of simple shapes, such as spheres, submerged in a steady uniform stream of a "rare medium" [*Anderson* (1989); *Cajori* (1934); *Chandrasekhar* (1995)]. Incidentally, the involved mechanics provide a rough estimation of vehicle aerodynamic properties in hypersonic flow. In Newton's model, the flow is comprised of rectilinear streams of particles. The particles are assumed to lose all their normal momentum upon striking the vehicle surface and then move tangential to the surface. Application of Newtonian

dynamics gives an expression for the surface pressure p_{surf} distribution, depending only on the local surface inclination angle relative to the freestream. In dimensionless form, that is, in terms of pressure coefficient C_p, the expression is known as the Newtonian sine-squared law. A modification to the model [*Lees* (1955)], making it semi-empirical and known as the modified Newtonian model, incorporates the value of the maximum pressure coefficient,

$$C_p = C_{p_{max}} \sin^2 \theta_b \tag{3.1}$$

where

$$C_p \equiv \frac{p_{surf} - p_\infty}{\frac{1}{2}\rho_\infty V_\infty^2} \tag{3.2}$$

and

$$-\sin \theta_b = \frac{\mathbf{V}_\infty}{|\mathbf{V}_\infty|} \cdot \mathbf{n} \tag{3.3}$$

$C_{p_{max}}$ is C_p of the maximum surface pressure p_{surf}. The variables p_∞, ρ_∞ and $V_\infty = |\mathbf{V}_\infty|$ are the freestream pressure, density and speed, respectively. θ_b and $\mathbf{n}$ are the body slope angle and the outward surface unit normal vector. The associated geometry is illustrated in Fig. 3.1. In this figure, the vectors $\vec{\xi}_i$ and
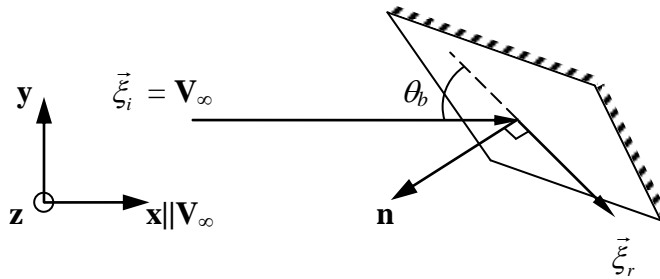
Figure 3.1   Surface element of Newtonian flow

$\vec{\xi}_r$ represent the incident and reflected molecular velocities. $\vec{\xi}_i$, $\vec{\xi}_r$ and **n** lie in the same plane. Newtonian theory assumes the incident molecular velocity $\vec{\xi}_i$ equals the freestream bulk velocity $\mathbf{V}_\infty$. When $180° < \theta_b < 360°$, the surface pressure is set to the freestream pressure, viz. $C_p = 0$. This flow model, with a good estimate of $C_{p_{max}}$, can provide an inexpensive estimate of hypersonic transitional flow aerodynamics for configurations where pressure dominates over shear stress.

3.2.3 Free molecular flow

When the global Knudsen number ($Kn = \lambda_\infty / l$) is greater than roughly 10, the freestream mean-free-path λ_∞ traveled by ambient molecules is much greater than the characteristic length l of the vehicle and collisions between molecules within a few characteristic lengths l from the vehicle become so few that the gas can be considered collisionless. The motion of a collisionless gas is called a free molecule or a free molecular flow. Properties of free molecular flow can be accurately computed by using free molecular flow analysis [*Gombosi* (1994)]. Free molecular flow analysis is suitable, for example, for calculating spacecraft drag above ~132 km where $Kn > 10$ for $l = 1$ m, according to the 1976 US Standard Atmosphere [*Lide* (2007)]. However, in this study free molecular flow analysis is not included to provide accurate results or even conceptual design estimations; rather, it is included to provide physical insight and to serve as an aid in the computer program development for the calculation of suborbital flight aerodynamics, in particular, atmospheric entry aerodynamics. The flow properties of interest in entry vehicle analysis are those that affect the vehicle's performance. These

include the pressure, shear stress and heat flux. Detailed knowledge of these flow properties enables the determination of the entry vehicle aerodynamic properties.

In the classic free molecular flow theory [*Schaaf and Chambré* (1961)], the vehicle is assumed to be immersed in an infinite domain of a collisionless gas having a Maxwellian velocity distribution appropriate to its temperature. Because molecules approaching the vehicle surface do not collide with reflected molecules, the freestream molecules receive no warning about the approaching vehicle and collide with its surface with the freestream molecular velocity. During collision, the molecules accommodate kinetically and thermally to the vehicle surface in a full or partial manner. When they are fully accommodated, they reflect diffusely with a Maxwellian velocity distribution. The degree of kinetic gas-surface accommodation in free molecular flow analysis is governed by the tangential and normal momentum accommodation coefficients, σ_t and σ_n, respectively, where $\sigma_t = \sigma_n = 0$ indicates no accommodation and specular reflection, and $\sigma_t = \sigma_n = 1$ indicates full accommodation and diffuse reflection.

The free molecular flow model is amenable to the derivation of expressions for aerodynamic surface properties. Consider an infinitesimal flat polygonal (triangular, rectangular, etc.) surface element, illustrated in Fig. 3.2, with a local coordinate system
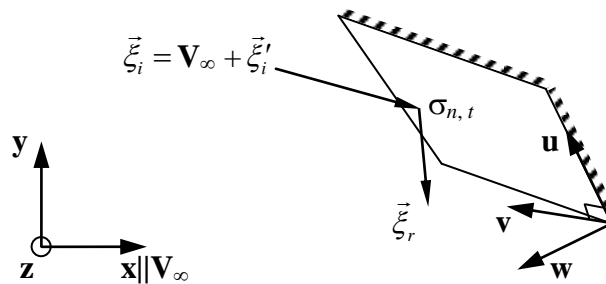
Figure 3.2   Surface element of free molecular flow

defined by the orthonormal set of vectors (**u**, **v**, **w**), where **u** is parallel to one side of the element and the origin is at a corner. Vectors **u** and **v** lie in the same plane as the surface element. The incident molecular velocity $\vec{\xi}_i$ is the sum of the ambient bulk velocity $\mathbf{V}_\infty$ and the incident random molecular velocity $\vec{\xi}_i'$. The surface element's polygonal shape is specified here for simplicity of numerical application, wherein the elements approach infinitesimal size only to a reasonable approximation. It can be shown that the corresponding surface pressure p_{surf} and shear stresses τ_u and τ_v are expressed by the following equations [*Sentman* (1961)]:

$$
\begin{aligned}
p_{surf} = q_\infty \Bigg(&\frac{\sigma_n}{2}\sqrt{\frac{T_w}{T_\infty}}\left\{ \frac{e^{-w_x^2 s^2}}{s^2} - \frac{w_x\sqrt{\pi}}{s}\left[1+erf\left(-w_x s\right)\right]\right\} \\
&-w_x\left(2-\sigma_n\right)\left\{\frac{e^{-w_x^2 s^2}}{s\sqrt{\pi}} - w_x\left[1+erf\left(-w_x s\right)\right]\right\} + \frac{2-\sigma_n}{2s^2}\left[1+erf\left(-w_x s\right)\right]\Bigg)
\end{aligned}
$$

(3.4)

$$
\tau_u = q_\infty \sigma_t u_x \left\{ \frac{e^{-w_x^2 s^2}}{s\sqrt{\pi}} - w_x\left[1+erf\left(-w_x s\right)\right]\right\}
$$

(3.5)

$$
\tau_v = q_\infty \sigma_t v_x \left\{ \frac{e^{-w_x^2 s^2}}{s\sqrt{\pi}} - w_x\left[1+erf\left(-w_x s\right)\right]\right\}
$$

(3.6)

where u_x, v_x and w_x are the components of **u**, **v** and **w** parallel to **x**. T_∞ and T_w are the ambient flow temperature and the local surface temperature. q_∞ is the freestream dynamic pressure and s is the molecular speed ratio:

$$
q_\infty = \frac{1}{2}\rho_\infty V_\infty^2
$$

(3.7)

$$
s \equiv \frac{V}{\xi_{mp}'} = \sqrt{\frac{\gamma}{2}}Ma
$$

(3.8)

$\xi'_{mp} = \sqrt{2k_B T / m}$ is the most probable molecular speed, where k_B is the Boltzmann constant, T is the local flow temperature, and m is the mean molecule mass of the mixture. γ is the ratio of specific heats and Ma is the associated Mach number. In the context of free molecular flow analysis, the freestream or ambient properties determine s. Regarding the gas-surface accommodation, full gas-surface accommodation is assumed for the free molecular flow analysis; that is, unity is assumed for the values of the tangential and normal momentum accommodation coefficients, $\sigma_t = \sigma_n = 1$.

3.3   Aerodynamic Force Integration

Equations (3.4) through (3.6), provide two approaches for computing a vehicle's aerodynamic forces. The first approach involves setting up a conglomerate of elements representing the surface of a vehicle. At a particular element, equations (3.4) through (3.6), the local surface element area and a three-dimensional rotation of coordinate axes result in the lift and drag forces on that surface element. The summation of these forces over the conglomerate of elements yields the total lift and drag forces on the vehicle. A similar procedure is used to compute the vehicle's pitch, yaw and roll moments, with the appropriate moment arms. These procedures enable the calculation of the aerodynamics of a vehicle of arbitrary shape within a free molecular flow. The second approach involves setting up the aerodynamic force integrals in terms of the pressure and shear stresses, the appropriate infinitesimal area elements, and the integration limits corresponding to the vehicle geometry. This approach is tractable for computing the aerodynamic coefficients of simple shapes within a free molecular flow. This can be done

by beginning with the expression for the resultant pressure and shear force dF/dA on an infinitesimal or differential surface element [*Sentman* (1961)]:

$$\frac{dF}{dA} = q_\infty \left(\left[\sigma_t \left(\chi_{Vx} \chi_{Fx} + \chi_{Vz} \chi_{Fz} \right) + \left(2 - \sigma_n \right) \right] \left\{ \chi_{Vy} s^2 \left[1 + erf \left(\chi_{Vy} s \right) \right] + \frac{s}{\sqrt{\pi}} e^{-\chi_{Vy}^2 s^2} \right\} \right.$$
$$+ \frac{\left(2 - \sigma_n \right) \chi_{Fy}}{2} \left[1 + erf \left(\chi_{Vy} s \right) \right] \tag{3.9}$$
$$\left. + \frac{\sigma_n \chi_{Fy}}{2} \sqrt{\frac{T_w}{T_i}} \left\{ \chi_{Vy} s \sqrt{\pi} \left[1 + erf \left(\chi_{Vy} s \right) + e^{-\chi_{Vy}^2 s^2} \right] \right\} \right)$$

where χ_{Vx}, χ_{Vy} and χ_{Vz} are the direction cosines between $\mathbf{V}_\infty$ and $\mathbf{x}$, $\mathbf{y}$ and $\mathbf{z}$, respectively; and χ_{Fx}, χ_{Fy} and χ_{Fz} are the direction cosines between $d\mathbf{F}$ and $\mathbf{x}$, $\mathbf{y}$ and $\mathbf{z}$. The aerodynamic forces are then determined by resolving the resultant force into the drag and lift directions, $(dF/dA)_D$ and $(dF/dA)_L$, respectively, and setting up integrals for the particular geometry and integrating either analytically or numerically. For example, the general integral expressions for the drag and pitching moment about point $(\cdot)$ are written below by Eqns. (3.9) and (3.10), respectively. In Eqn. (3.10), the functions arm_D and

$$F_D = \iint\limits_{\text{surface}} \left(\frac{dF}{dA} \right)_D dA \tag{3.10}$$

$$M_{P(\cdot)} = \iint\limits_{\text{surface}} \left[arm_D \left(\frac{dF}{dA} \right)_D + arm_L \left(\frac{dF}{dA} \right)_L \right] dA \tag{3.11}$$

arm_L represent the variation of the moment arms referenced to point $(\cdot)$ and perpendicular to the drag and lift directions, respectively, with element position.

In this study, the element summation approach is implemented in C code for determining the aerodynamic forces from the pressure and shear stresses computed by DSMC on an arbitrary vehicle shape represented by small surface elements. This implementation of the summation approach is validated using the free molecular flow

analysis by comparing it to the integral equations approach for a blunted-cone, illustrated by Fig. 3.3. The dimensions used for the blunted-cone are those of the windtunnel test model of *Boylan and Potter* (1967). The respective integral expressions for the drag, lift and pitching moment are given by Eqns. (3.12) through (3.14), where: Cartesian, conical and spherical area differentials are used for the cone base, cone frustrum and spherical
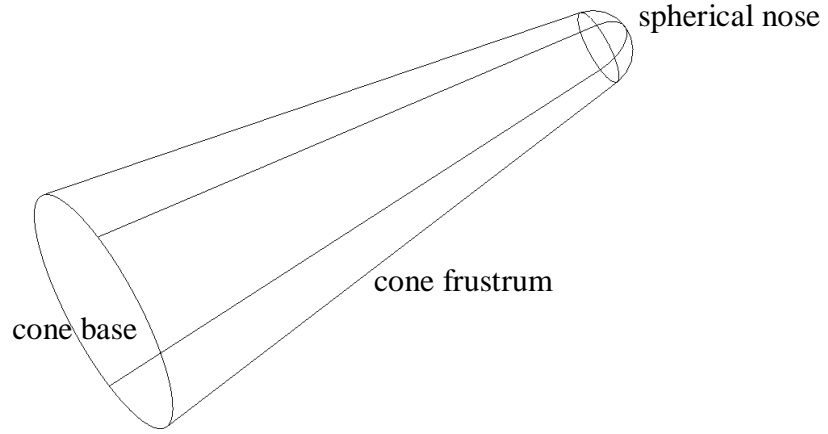
Figure 3.3   Blunted-cone integration regions

Blunted-cone integral equations for the aerodynamic forces and moment

$$F_D = \iint_{\substack{cone \\ frustrum}} \left(\frac{dF}{dA}\right)_D dA + \iint_{\substack{spherical \\ nose}} \left(\frac{dF}{dA}\right)_D dA + \iint_{\substack{cone \\ base}} \left(\frac{dF}{dA}\right)_D dA \qquad (3.12)$$

$$F_L = \iint_{\substack{cone \\ frustrum}} \left(\frac{dF}{dA}\right)_L dA + \iint_{\substack{spherical \\ nose}} \left(\frac{dF}{dA}\right)_L dA + \iint_{\substack{cone \\ base}} \left(\frac{dF}{dA}\right)_L dA \qquad (3.13)$$

$$M_{P(\cdot)} = \iint_{\substack{cone \\ frustrum}} \left[arm_D \left(\frac{dF}{dA}\right)_D + arm_L \left(\frac{dF}{dA}\right)_L \right] dA$$

$$+ \iint_{\substack{spherical \\ nose}} \left[arm_D \left(\frac{dF}{dA}\right)_D + arm_L \left(\frac{dF}{dA}\right)_L \right] dA + \iint_{\substack{cone \\ base}} \left[arm_D \left(\frac{dF}{dA}\right)_D + arm_L \left(\frac{dF}{dA}\right)_L \right] dA \qquad (3.14)$$

nose, respectively. For brevity, the equations are not expanded further. Comparisons are made of the nondimensionalized forces and moment, that is, the force and moment coefficients. For reference, the definitions of lift and drag coefficients and of the pitching moment coefficient about point $(\cdot)$ are listed respectively by the following equations:

$$C_D = \frac{F_D}{q_\infty A_{ref}} \tag{3.15}$$

$$C_L = \frac{F_L}{q_\infty A_{ref}} \tag{3.16}$$

$$C_{M(\cdot)} = \frac{M_{P(\cdot)}}{q_\infty A_{ref} d_{ref}} \tag{3.17}$$

where the reference area is the area of the cone base, $A_{ref} = \pi d_{ref}^2 / 4$, and the reference length d_{ref}, is the diameter of the cone base. Comparisons are also made of the lift-to-drag ratio: $L/D \equiv F_L / F_D = C_L / C_D$.

Equations (3.12) through (3.14) are integrated numerically with *MathCad* (1998) and compared with the implementation of the summation approach applied to a flat panel representation of the blunted-cone. The precise agreement between the two integration procedures is demonstrated in Figs. 3.4 (a) and (b). To generate all the data shown in these figures, the calculations on a 3 GHz personal computer take about 24 seconds by the integral equations and about 100 seconds by the element summation. This indicates that the integral equations approach is generally faster, although it is limited to simple geometries.

Apart from validating the element summation approach, Figs. 3.4 (a) and (b) provide information about the blunted-cone free molecular flow aerodynamics. The variations of

41
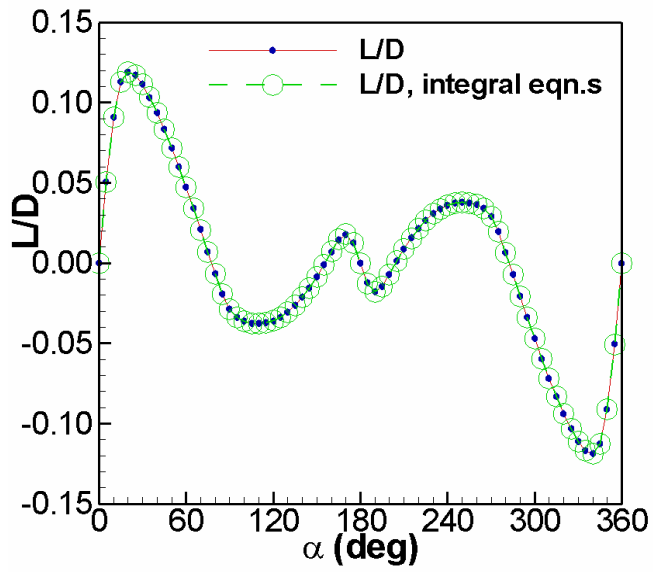
(a) *Lift-to-drag ratio*
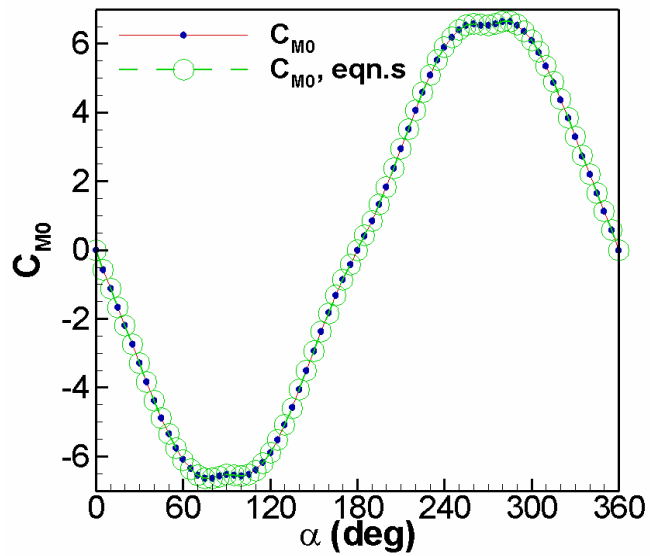
(b) *Pitching moment about point O, the blunted-cone spherical nose tip*

Figure 3.4   Validation of element summation integration procedure against integral equations using free molecular flow analysis for the blunted-cone at $Ma_\infty = 9.56$

L/D and C_{MO} as functions of angle-of-attack are governed by the vehicle shape. They are odd functions about 180° because of the axisymmetry. The *L/D* variation is primarily governed by the lift variation. The angle of maximum *L/D*, which is 20°, is also the angle of maximum lift. The *L/D* becomes negative between 75° and 80° because that is where the blunted-cone begins exhibiting negative lift, which is related to its 9° half angle. The *L/D* increases between 110° and 170° because that is where the cone base becomes exposed to the freestream and produces increasing lift. The sinusoidal behavior of the pitching moment variation can be attributed to the slenderness and symmetry of the blunted-cone. The plateau regions of the C_{MO} curve occur when the cone base becomes exposed to the freestream; and thus, are due to counteracting moment components from the cone base.

3.4   Blunted Cone Simulations

3.4.1 Flow conditions and geometry

Flow conditions and geometry for the blunted-cone windtunnel test [*Boylan and Potter* (1967)] are shown in Table 3.1 and Fig. 3.5, respectively. These conditions include the Reynolds number defined by $Re_{d\infty} = \rho_\infty V_\infty d_{ref} / \mu_\infty$, where μ_∞ is the freestream viscosity. The value of $Re_{d\infty}$ is provided by the *Boylan and Potter* (1967) and reflects the low viscosity of the transitional rarefied flow. The pitching moment for the 9° blunted-cone is taken with respect to point O. More details of the cone's geometry are given by *Boylan and Potter* (1967). Because the windtunnel test model has a global Knudsen number that is within the rarefied transitional flow regime, the DSMC method is suitable for estimating the model's aerodynamics. These conditions provide some of the starting

Table 3.1 **Conditions of blunted-cone windtunnel test**

Property	Value
d_{ref}	1.524×10^{-2} m
Gas	N_2
T_∞	143.5 K
Ma_∞	10.15
$Re_{d\infty}$	233
T_w	600 K
Kn	0.065
n_∞	1.323×10^{21} m^{-3}
λ_∞	9.9×10^{-4} m
V_∞	2478 m/s
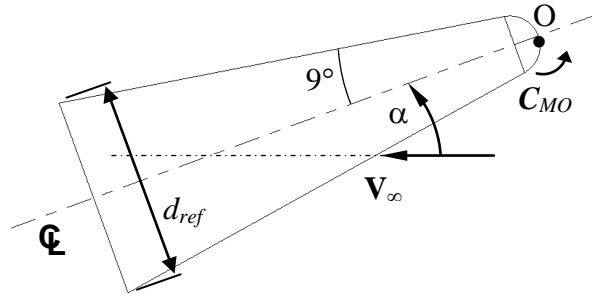
Figure 3.5   Blunted-cone geometry

parameters for the DSMC calculations.

Three-dimensional computational domain boundaries for the DSMC simulations are generated with *Pro/ENGINEER* (2004). They are then exported to *HyperMesh* (2004), a grid generation program, which is used in this case to create an unstructured tetrahedral mesh, with cell-sizes manually adapted to the local mean-free-path, according to the DSMC constraint. Figure 3.6 is an image of the domain boundary surface mesh, with the model at a 20° angle-of-attack. The symmetry of the blunted-cone geometry and the assumed uniform inflow boundary requires simulation of only half of the domain. In this study, three-dimensional simulations are made for the blunted-cone at 0, 10, 20 and 25 degrees angle-of-attack. A distinct mesh is generated for each angle-of-attack case, where each mesh consists of roughly 560,000 tetrahedral cells. For the modified Newtonian and free molecular flow calculations, only the vehicle surface grid is necessary. The surface grids are extracted from the three-dimensional grids employed in the DSMC calculations, and involves only about 1,900 cells.
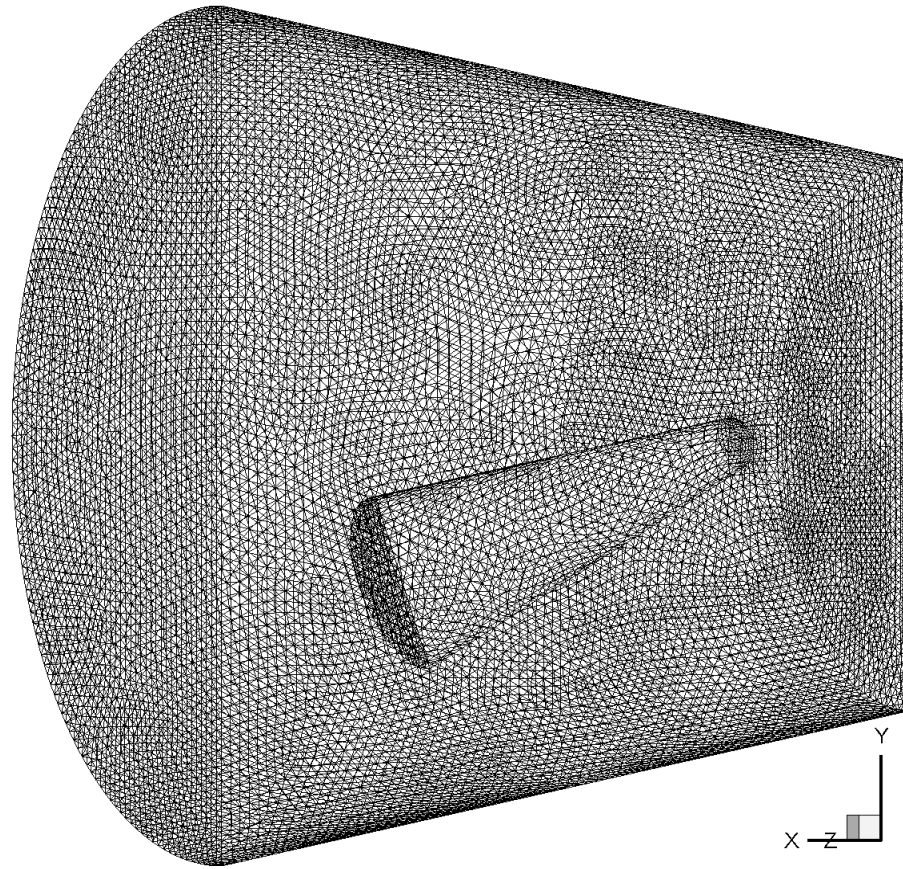
Figure 3.6 **Domain boundary for simulation of blunted-cone at a 20°
angle-of-attack**

3.4.2 Results and discussion

Figure 3.7 illustrates the general character of the flow field for the blunted-cone. The

freestream region is sufficiently large to capture the diffuse shock near the windtunnel

test model and the peak flow temperature is not sufficient to justify activation of nitrogen

dissociation procedures [*Anderson* (1989); *Josyula* (2001)].

The aerodynamic results of the DSMC simulations for the blunted-cone, with two

values of Maxwell's accommodation coefficient a_M, are compared with the simpler flow

models and the available windtunnel data. (Maxwell's gas-surface interaction model as

implemented into the MONACO DSMC code is described in Chapter 5 where gas-

Figure 3.7   Contour plot of translational temperature at symmetry boundary of three-dimensional windtunnel test simulation with blunted-cone at 20° angle-of-attack

surface interaction models are reviewed and a_M is defined.) Figure 3.8 (a) compares the drag coefficient among the computer calculations and the windtunnel tests at various angles-of-attack. In these figures, the DSMC calculations generally yield lift and drag coefficients that lie somewhere between the values given by the modified Newtonian and free molecular flow results. A major reason the modified Newtonian model predicts lower drag is that it neglects shear stress. The free molecular flow model predicts higher drag because it neglects intermolecular collisions. The modified Newtonian analysis for the blunted-cone employed $C_{p_{max}}$ = 1.83, from *Boylan and Potter* (1967). The
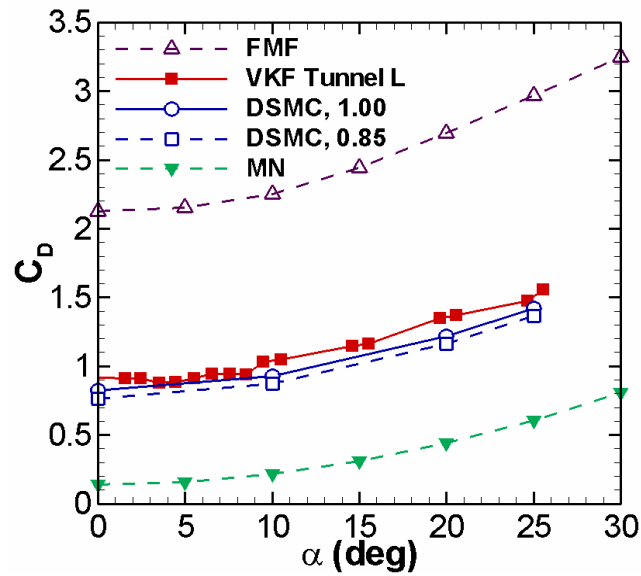
(a) *Drag Coefficient*
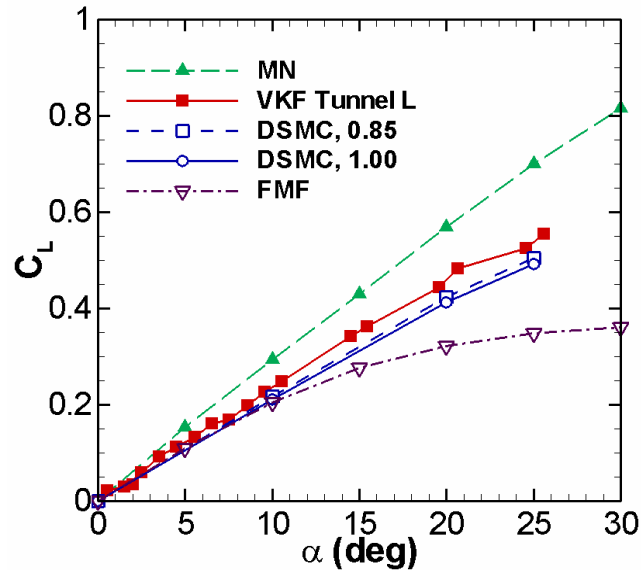
(b) *Lift Coefficient*

Figure 3.8   Variation of blunted-cone drag and lift with angle-of-attack with the modified Newtonian (MN) model, the free molecular flow (FMF) model, DSMC at two values of gas-surface accommodation a_M, and windtunnel results from the AEDC VKF Tunnel L

47

disagreements between the simpler models and DSMC provide a measure on the effects of the neglected phenomena in the simpler models. Figures 3.8 (a) and (b) indicate that shear stress and intermolecular collisions play strong roles in the lift and drag integration, with the drag affected more.

The variation of C_D with α given by the DSMC cases agree well with that of the windtunnel data. The DSMC, with $a_M = 1$, and the windtunnel data are 6.9, 8.7, 7.8 and 7.7% different from the windtunnel data at 0, 10, 20 and 25°, angle-of-attack, respectively. At 0° angle-of-attack, a reduction in the thermal accommodation coefficient by 15% reduces the drag coefficient by 6%, from 0.82 to 0.77. Figure 3.8 (a) shows that the reduction in accommodation uniformly affects the drag at all the angles-of-attack considered. The reduction in drag due to a reduction in a_M is a consequence of reduced backscatter by the introduction of specular reflections in the Maxwell gas-surface interaction model. This reduction moves the DSMC results slightly further from the windtunnel drag data; thus, it indicates that full gas-surface accommodation is the more accurate estimate between the two DSMC cases. Figure 3.8 (b) illustrates the comparisons for the lift coefficient. The DSMC lift trend also agrees well with the windtunnel data. The difference between the DSMC and windtunnel data is about 10% at 10, 20 and 25° angle-of-attack. At zero angle-of-attack, the lift coefficient is zero because of the prescribed symmetry. There, the nonzero windtunnel data is probably due to statistical scatter. The uncertainty of the windtunnel measurements is not reported by *Boylan and Potter* (1967). The reduction in the gas-surface accommodation coefficient does not significantly affect the lift coefficient.

(a) *Lift-to-drag ratio*

(b) *Pitching moment about blunted-cone spherical nose tip*

Figure 3.9   **Variation of blunted-cone lift-to-drag ratio and pitching moment with angle-of-attack with the modified Newtonian (MN) model, the free molecular flow (FMF) model, DSMC at two values of gas-surface accommodation a_M, and windtunnel results from the AEDC VKF Tunnel L**

Figure 3.9 (a) illustrates the comparisons for the lift-to-drag ratio. Again, the DSMC data lie well within the modified Newtonian and the free molecular flow data. The DSMC lift-to-drag ratio is not significantly affected by the 15% reduction in gas-surface accommodation, and there is no significant difference between the DSMC and windtunnel data. The agreement between the DSMC and windtunnel data of the lift-to-drag ratio is closer than that of the individual lift and drag comparisons, c. f. Figs. 3.8 (a) and (b). Taking the ratio of the lift and drag seems to cancel out some of the error given by the individual lift and drag comparisons; hence, separate lift and drag comparisons provide closer scrutiny of the DSMC data evaluated relative to the windtunnel data. Figure 3.9 (b) illustrates the comparisons for the pitching moment. Once again, the DSMC results lie between the simpler model results. The reduction in gas-surface accommodation coefficient does not incur any significant effect on the DSMC results, and the DSMC results agree well with the windtunnel results. At zero degree angle-of-attack the pitching moment is zero because of the prescribed symmetry. From 10 to 25° angle-of-attack, the agreement between the DSMC and windtunnel pitching moment results improve with increasing angle-of-attack. The Percentage differences between the DSMC and windtunnel pitching moment are 11, 5, and 2% for $\alpha = 10$, 20 and 25°, respectively. However, the small improvements are likely within the uncertainty of the windtunnel test data, again not reported by *Boylan and Potter* (1967).

3.5   Apollo Command Module Simulations

3.5.1 Flow conditions and geometry

Flow conditions and geometry for the Apollo Command Module (ACM) windtunnel test [*Boylan and Griffith* (1968)] are shown in Table 3.2 and Fig. 3.10, respectively. Figure 3.10 shows the location of the center-of-gravity with respect to the windward heat-shield apex and defines the angle-of-attack with respect to the leeward vehicle axis of symmetry. The pitching moment for the ACM is taken relative to the center-of-gravity. Further details of the ACM geometry are given by *Boylan and Griffith* (1968).

Table 3.2   Conditions for the ACM windtunnel test

Property	Value
d_{ref}	1.524×10^{-2} m
Gas	N_2
T_∞	142.2 K
Ma_∞	10.20
$Re_{d\infty}$	230
T_w	300 K
Kn	0.067
n_∞	1.280×10^{21} m^{-3}
λ_∞	0.001 m
V_∞	2479 m/s
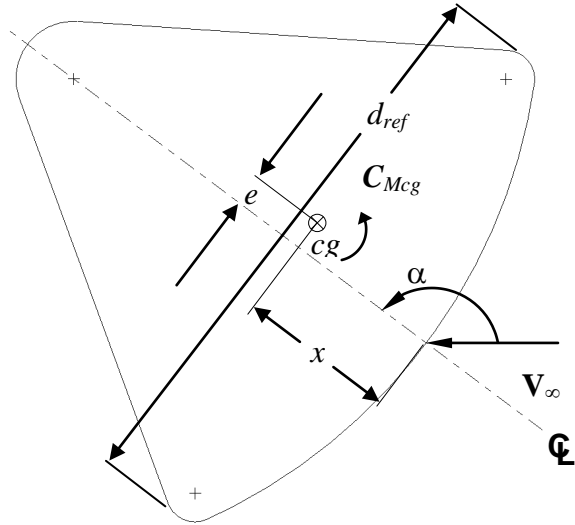
Figure 3.10 ACM geometry

The flow conditions are similar to the blunted-cone windtunnel test. The Knudsen number is well into the transitional rarefied flow regime, so the DSMC method again provides a suitable approach for analysis. The procedures for setting up the numerical simulations are similar to those described for the blunted-cone simulations, Section 3.4.1. Figure 3.11 is an image of the domain boundary surface mesh, with the ACM windtunnel model at an angle-of-attack of 150°. Three-dimensional windtunnel test simulations are

51

made for the ACM at angles-of-attack of 180, 170, 160, 150 and 140°, where a distinct

mesh is generated for each angle-of-attack. Each of these meshes has about 740,000 cells

or 32% more cells than the blunted-cone simulations. The larger number of cells is due to

the larger compression region, which is due to the broader size of the model's front end.

Compression regions or regions of higher density within the shock layer require more

cells in order to handle associated smaller mean-free-paths. The ACM surface meshes,
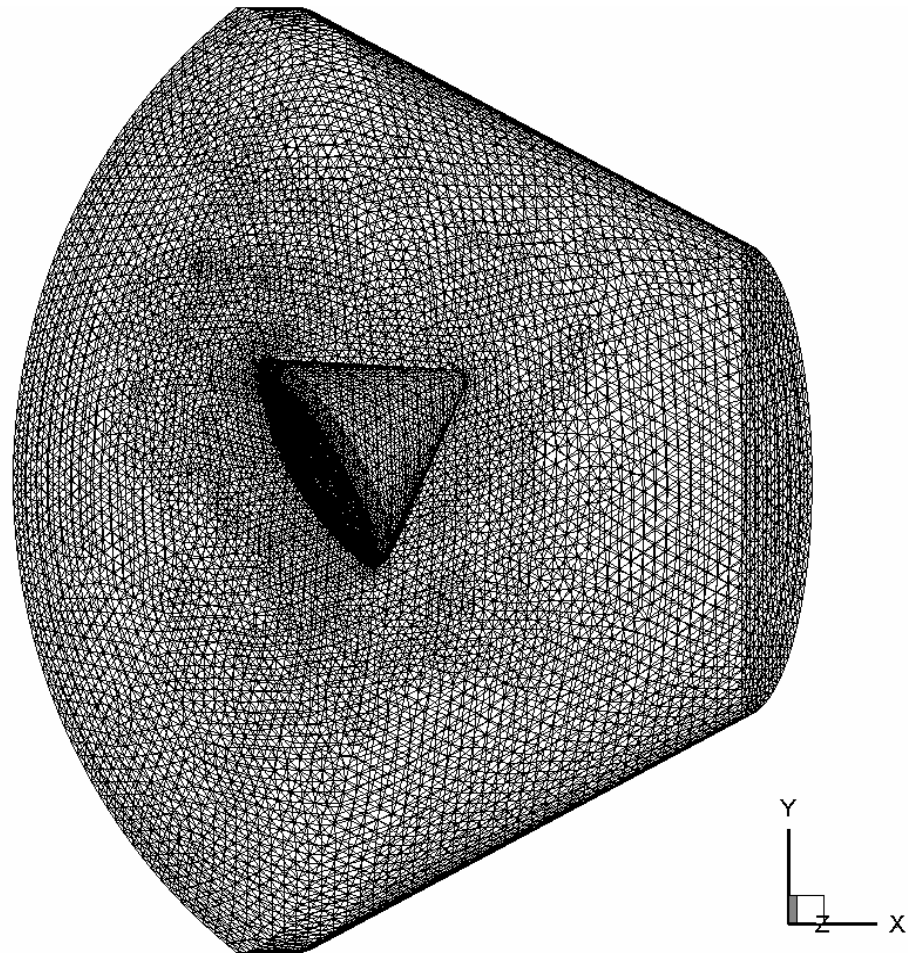
Figure 3.11 Domain boundary for simulation of ACM at a 150° angle-of-attack

employed for the modified Newtonian and free molecular flow calculations, and extracted from the three-dimensional meshes, involve about 8,960 cells.

3.5.2 Results and discussion

The analysis of the ACM windtunnel simulations is similar to the analysis of the blunted-cone simulations. However, for the ACM DSMC calculations only full gas-surface accommodation is employed since a reduction of 15% accommodation is not expected to affect the results significantly. Figure 3.12 illustrates the general character of
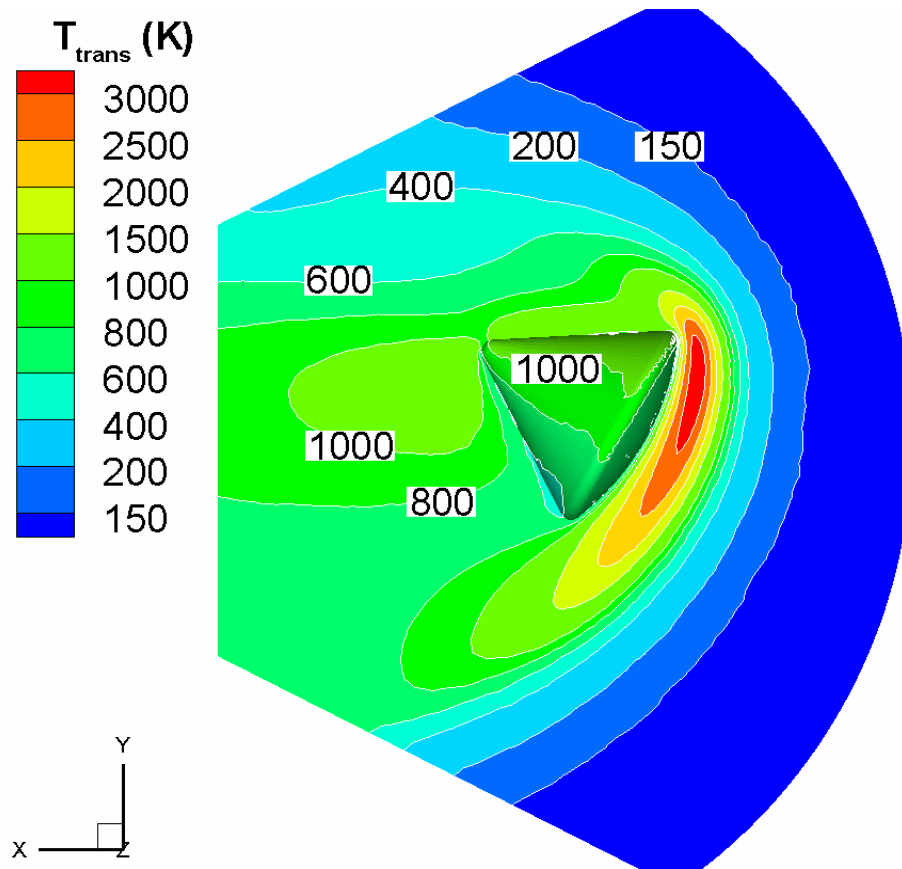
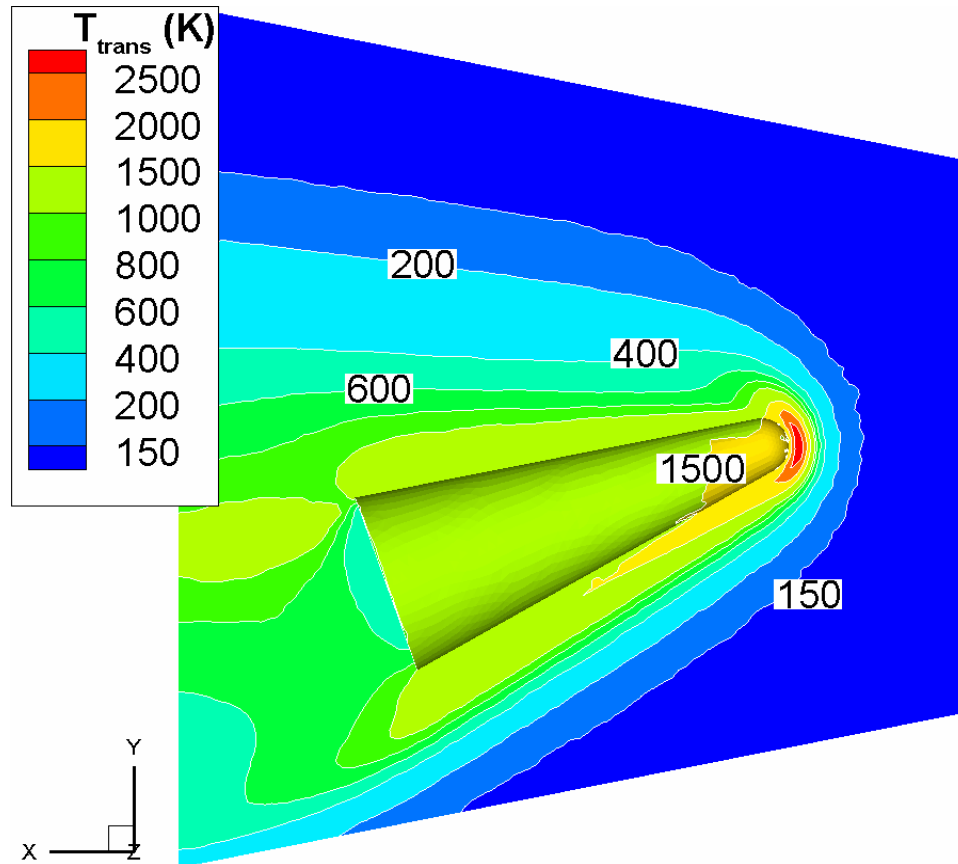**Figure 3.12 Contour plot of translational temperature at symmetry
boundary of three-dimensional windtunnel test
simulation with ACM at 150° angle-of-attack**

the flow field about the ACM. The freestream region is sufficiently large to capture the diffuse shock near the vehicle and the peak flow temperature is again not sufficiently large to justify activating chemical reaction procedures.

Figures 3.13 and 3.14 compare windtunnel and simulation data of C_L, C_D, L/D and C_{Mcg} at various angles-of-attack for the ACM. In these figures, the DSMC calculations generally yield lift and drag coefficients that lie somewhere between the values given by the modified Newtonian and free molecular flow results. The modified Newtonian analysis employed $C_{p_{max}}$ = 1.89, obtained from the DSMC analysis. The windtunnel C_D, C_L and L/D were extracted from separate plots in *Griffith and Boylan* (1968). For the ACM, a second set of DSMC results are plotted. These results are provided by Dr. James Moss (private communication, Dec. 2005) from NASA Langley Research Center using a different implementation of the DSMC method called DS3V [*Bird* (2005)]. The DS3V results corroborate the MONACO procedures. However, the DSMC and windtunnel data do not agree well. At 180°, the DSMC and windtunnel drag coefficients are 12.6% different, almost twice the percentage difference than for the blunted-cone. The windtunnel drag decreases more rapidly with angle-of-attack than the DSMC drag. The windtunnel lift is substantially greater than that predicted by any computational model. Nevertheless, taking the ratio of the DSMC lift and drag coefficients again cancels out some of the disagreement between the DSMC results and the windtunnel data. This again indicates that plotting the lift and drag coefficients separately provides a more stringent examination than plotting the lift-to-drag ratio. In addition, there is closer agreement
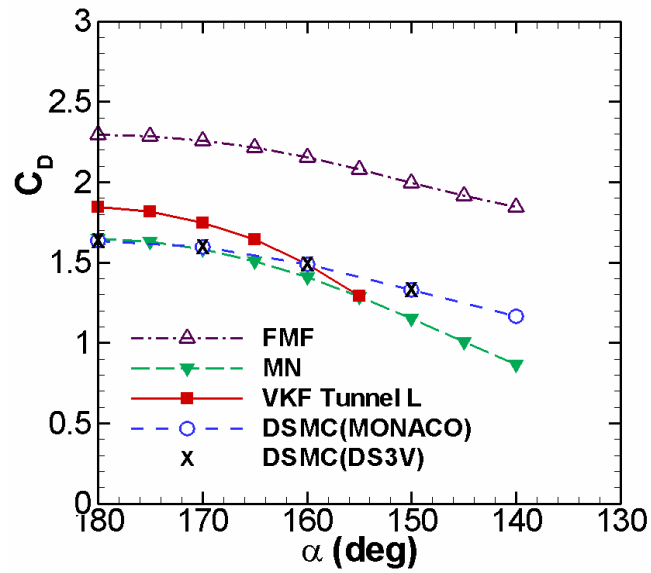
(a) *Drag Coefficient*
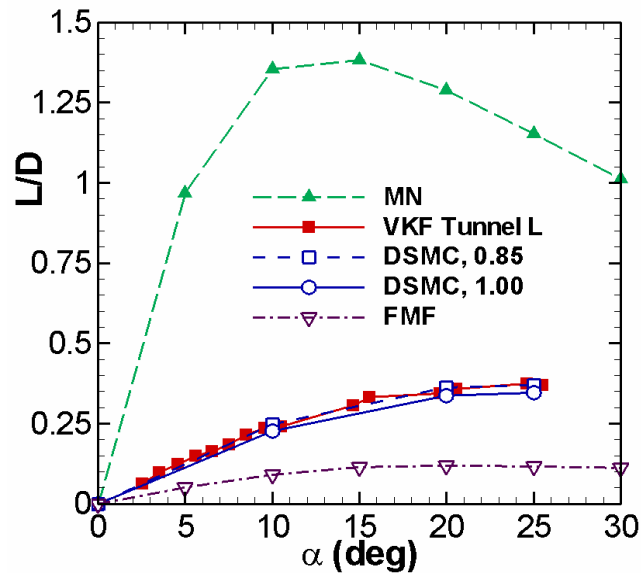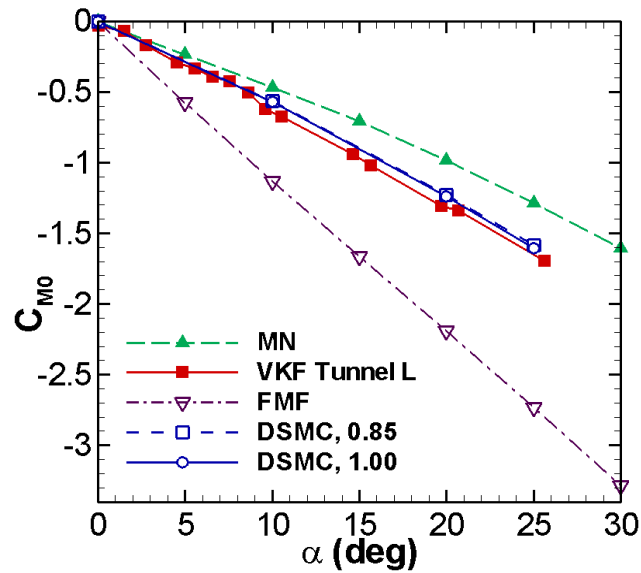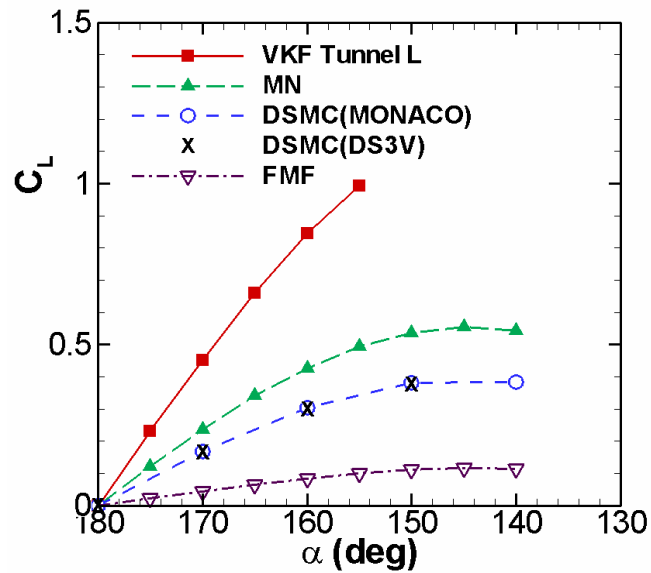

(b) *Lift Coefficient*

Figure 3.13 Variation of ACM drag and lift with angle-of-attack with the modified Newtonian (MN) model, the free molecular flow (FMF) model, two different implementations of the DSMC method: MONACO and DS3V, and windtunnel results from the AEDC VKF Tunnel L
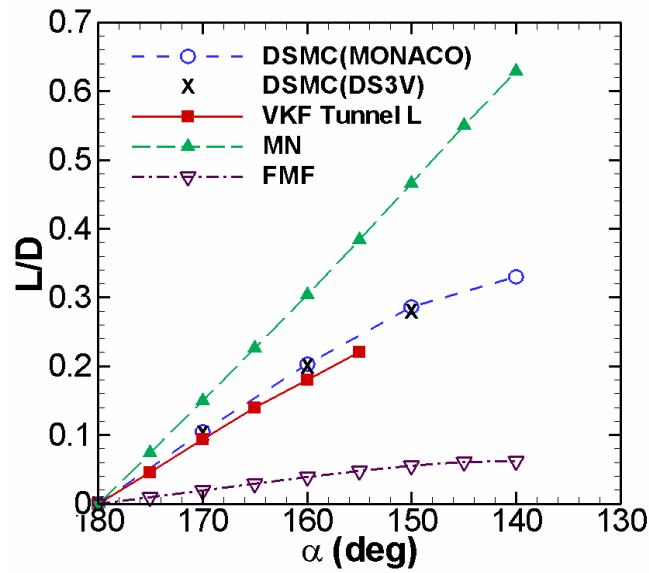
(a) *Lift-to-drag ratio*
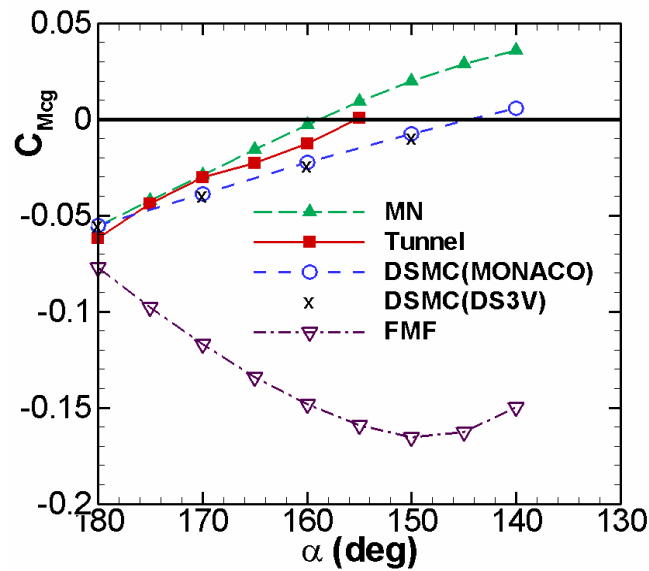
(b) *Pitching moment about ACM center-of-gravity*

Figure 3.14 Variation of ACM lift-to-drag ratio and pitching moment with angle-of-attack with the modified Newtonian (MN) model, the free molecular flow (FMF) model, two different implementations of the DSMC method: MONACO and DS3V, and windtunnel results from the AEDC VKF Tunnel L

between the DSMC and windtunnel pitching moment data than either the drag or lift. However, the agreement is still significantly worse than for the blunted-cone.

3.6 Axisymmetric Simulations

3.6.1 Flow conditions and geometry

To help determine the cause of the discrepancies between the DSMC and windtunnel data of the ACM, a parametric study was performed with inexpensive axisymmetric simulations of the ACM at 180° angle-of-attack. In addition axisymmetric simulations of existing Gemini spacecraft windtunnel data [*Boylan and Potter* (1967)] are examined. In general, when an axisymmetric body's axis of symmetry is parallel to a uniform or axisymmetric inflow boundary, the axisymmetry allows one to simulate the flow with a two-dimensional grid that contains the body's profile. For an axisymmetric space capsule diving into an atmosphere from space, axisymmetric simulations of the capsule at zero inclination angle, relative to the freestream, are an inexpensive way of determining the general character of the flow-field, including an estimate of domain size and chemical activity, from where three-dimensional simulations involving a nonzero inclination angle may begin. They are also an inexpensive way of performing parametric analysis where a physical or geometrical parameter is varied.

In the windtunnel study that tested a handful of simple vehicle shapes [*Boylan and Potter* (1967)], including the blunted cone, a scale model of the Gemini spacecraft was also considered. The conditions of the Gemini model windtunnel test are the same as those for the blunted-cone windtunnel test, except for the vehicle reference length, and consequently, vehicle Knudsen number and Reynolds number. The reference length is the

model diameter of $d = 1.27$ cm. The corresponding vehicle Knudsen number and Reynolds number are $Kn = 0.078$ and $Re_d = 194$, respectively. The reference length or diameter of the Apollo model is 20% larger than that of the Gemini model. Figure 3.15 illustrates the geometry; further details of the Gemini model geometry are given by *Boylan and Potter* (1967) and *Griffith* (Jan. 1967).
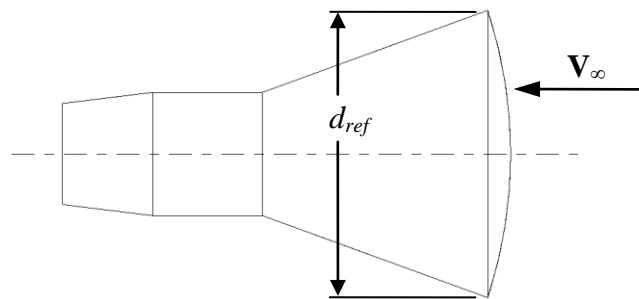
Figure 3.15. Gemini spacecraft model geometry

The two-dimensional computational meshes of the Apollo and Gemini axisymmetric simulations are generated using a procedure similar to the generation of the three-dimensional blunted-cone and Apollo meshes. Each domain boundary is generated with ProE and exported to HyperMesh, where the unstructured quadrilateral cell mesh is created. Figures 3.16 (a) and (b) illustrate these meshes. More cells are required for the ACM because it has a larger compression region. These meshes and their respective DSMC simulation runs are about an order of magnitude less expensive than the three-dimensional cases. Table 3.3 compares the numerical parameters of the three-dimensional and axisymmetric simulations. The simulation expense is sensitive to the extent of the compression region ahead of the vehicle.
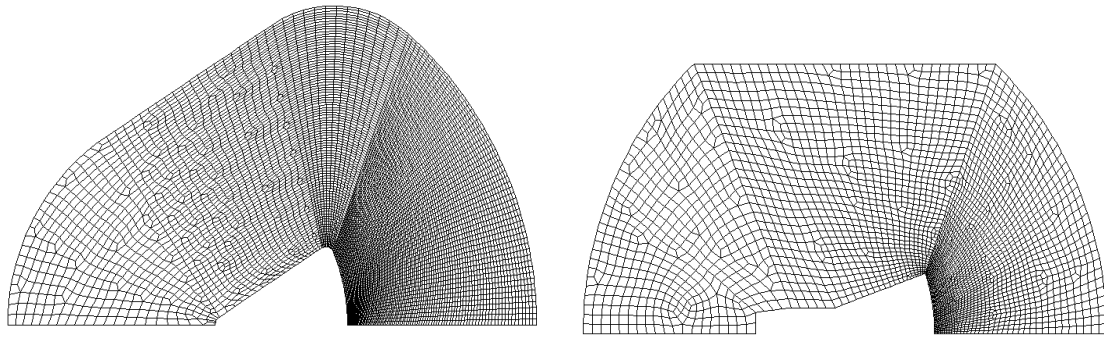
(a) *Apollo Command Module*   (b) *Gemini spacecraft*

Figure 3.16 Images of the axisymmetric simulation meshes

Table 3.3   Comparison of simulation parameters

Simulation	Cells	Particles	Wall time	CPUs[***]
Axisymmetric[*]				
Gemini	3,348	818,000	4 hr	1
Apollo	9,332	1,320,000	3.5 hr	2
3-Dimensional[**]				
Blunted-cone	560,000	12,500,000	8 hr	8
Apollo	740,000	47,500,000	21 hr	20

[*]Quadrilateral Cells
[**]Tetrahedral Cells
[***]1.4–1.8 GHz Opteron or Intel Itanium processors

3.6.2 Results and discussion

The initial purpose of the axisymmetric simulations is to determine whether the windtunnel data was possibly measured inaccurately. This is performed by examining the sensitivity of the computed drag coefficient of the axisymmetric ACM simulation to changes in the reported conditions. In particular, the freestream Mach number and the reservoir temperature are varied in the simulations by ±20%. The corresponding freestream temperature is computed from the Mach number and reservoir temperature,

assuming the flow travels isentropically from the reservoir to the test section. Then, the freestream speed of sound and bulk flow speed are determined. Table 3.4 provides the corresponding results. A 20% decrease and increase in the freestream Mach number results in roughly a 40% increase and a 30% decrease, respectively, in the freestream number density. However changing the freestream Mach number by ±20% only changes the drag coefficient by ±2%. The same variations in reservoir temperature give less than 12% changes in freestream velocity and number density and insignificant changes in drag coefficient. Therefore, the windtunnel flow conditions were measured accurately enough and the disagreement between the computer simulations and the windtunnel data for the drag coefficient must be due to some other problem. Possible explanations include a nonuniform velocity profile at the inflow boundary, windtunnel wall boundary layer effects and nonequilibrium in the freestream.

Table 3.4   Sensitivity of Drag Coefficient of ACM due to changes in Reported Conditions

Baseline Conditions $Ma_\infty = 10.2$ $T_0 = 3,100$ K	V_∞ (m/s) 2479		n_∞ (10^{21}/m^3) 1.279		C_D 1.645	
Variation	V_∞	ΔV_∞	n_∞	Δn_∞	C_D	ΔC_D
Ma_∞ decreased by 20%	2448	−1.3%	1.815	42%	1.620	−2%
Ma_∞ increased by 20%	2497	0.7%	0.9344	−27%	1.679	2%
T_0 decreased by 20%	2217	−11%	1.180	−8%	1.646	0.1%
T_0 increased by 20%	2716	10%	1.357	6%	1.645	0%

The second purpose of the axisymmetric simulations is to help determine whether the difference between the DSMC and windtunnel data is due to windtunnel wall boundary layer interference with the larger diffuse shockwave structure incurred by the ballistic capsule shapes. If the Gemini windtunnel data agrees with DSMC data, then the Apollo

simulation problem is not likely due to the shock–boundary layer interaction. Figure 3.17 displays selected contour plots from the Apollo and Gemini axisymmetric simulations. These plots show that the upstream region contains sufficient freestream to capture the diffuse shock structure near the vehicle and that the peak translational temperature is not large enough to incur nitrogen dissociation.
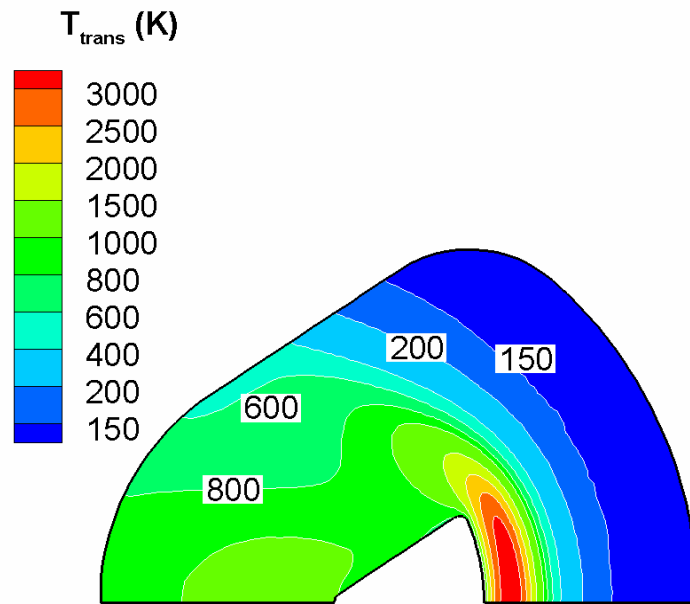
(a) *Apollo Command Module*

Figure 3.17 Translational temperature contour plots of axisymmetric simulations for the examination of the possibility of shock–wall boundary layer interaction
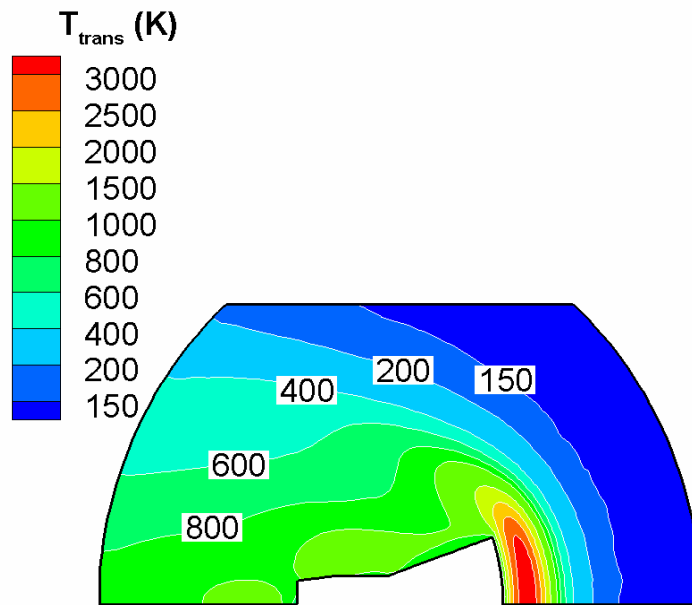
(b) *Gemini Spacecraft*

Figure 3.17 Concluded.

Table 3.5 provides comparisons of the windtunnel and axisymmetric simulation drag coefficients. A result for the ACM from another DSMC code called DS2V, computed by Dr. Moss, is also listed, and again provides additional credibility to the MONACO procedures. For the ACM, the axisymmetric simulation drag coefficient is 1.2% larger than the three-dimensional simulation result. This difference is probably due to differences in grid cell types and cell distributions between the two and three dimensional meshes. The difference between the DSMC results and the windtunnel data is an order of magnitude greater than the difference between the axisymmetric and three-dimensional results, which is about 11%. The three-dimensional simulation drag coefficient at 180°

Table 3.5   Comparison of axisymmetric simulation drag with windtunnel data

Case	C_D	Difference
Apollo		
Windtunnel	1.85	
MONACO	1.65	-11.4%
DS2V	1.66	-10.8%
Gemini		
Windtunnel	1.86	
MONACO	1.72	-7.5%

angle-of-attack, shown in Fig. 3.13 (a), is 1.63. The smaller diameter Gemini model is associated with a smaller disagreement in the drag coefficient, Table 3.5. The ballistic capsule shapes have larger disagreement between the DSMC and windtunnel data than the slender blunted-cone shape. The models with broader front ends have larger diffuse shock structures that are more susceptible to interference with a growing windtunnel boundary layer. Thus, the windtunnel data for these models may be inaccurate because of disregarded wall effects. Unfortunately, available references [*Potter et al.* (1964); *Potter et al.* (1962)] do not provide sufficient details of the windtunnel geometry in order to adequately simulate the windtunnel test to accurately capture the growing wall boundary layer from the nozzle and determine the boundary layer effects on the windtunnel model aerodynamics.

3.7   Chapter Summary and Conclusions

The aerodynamic properties of drag, lift, pitching moment, and lift-to-drag ratio, of entry vehicle windtunnel test models within a hypersonic, rarefied nitrogen gas environment were analyzed using three-dimensional DSMC computations. Modified

Newtonian and free molecular flow models were used to develop procedures to compute the aerodynamic properties computed by the MONACO DSMC code. For the blunted-cone windtunnel model, DSMC and windtunnel aerodynamic data agreed well, and a 15% reduction in gas-surface thermal energy accommodation did not significantly affect the DSMC results. For the Apollo windtunnel test, DSMC and windtunnel data did not agree well. The drag from DSMC was roughly 13% less than that from the windtunnel test. For the Apollo simulations, a second set of DSMC results, generated by a different code, DS2V/3V, provided confidence in the MONACO procedures. Consequently, the possibility of discrepant Apollo windtunnel test results was examined by a couple of axisymmetric simulation studies. First, a sensitivity study demonstrated that the drag coefficient experienced insignificant changes when the reported Mach number or reservoir temperature was perturbed by ±20%. Therefore, the Mach number and reservoir temperature were considered to be measured accurately enough. Second, a Gemini windtunnel test simulation was performed to determine whether the problem was related to windtunnel wall boundary layer interference. This simulation revealed 7.5% disagreement between the DSMC and windtunnel drag coefficient of the Gemini model. The disagreement in drag between the DSMC and windtunnel data of the Apollo was about 50% greater. The Apollo has a 20% larger diameter than the Gemini. Therefore, it is possible that the windtunnel wall boundary layer interferes with the diffuse shock in front of the models. However, simulations including the windtunnel wall boundary are not possible because the available references [*Potter et al.* (1964), *Potter et al.* (1962)] do not provide sufficient details of the windtunnel geometry. In conclusion, aerodynamic integration procedures were validated and a sensitivity study suggested that the 1960's

64

windtunnel results of the ACM are potentially affected by wall boundary layer interference. In the next chapter, an aerodynamic sensitivity study is presented with simulations of Apollo 6 flight conditions.

CHAPTER IV

SENSITIVITY OF AEROTHERMODYNAMICS PREDICTIONS FOR APOLLO 6 RETURN AT 110 km ALTITUDE

4.1   Background

In the mid to late 1960's the Apollo program first tested the Apollo Command Module (ACM) with unmanned flights that achieved various engineering objectives. The first of these occurred in February, 1966, with mission AS-201 [*Grinter* (2005)]. By April, 1968, the last of the unmanned flights, mission Apollo 6 was conducted. Flight data from the Apollo 4 and 6 missions were documented by *Lee and Goodrich* (1972). These missions involved unmanned test flights of the ACM with entry velocities of roughly 10.0 km/s into the Earth's atmosphere. Surface pressure and heating rate history data were gathered by using pressure transducers, radiometers and calorimeters; however, above 80 km the data are too scattered for DSMC code validation. Furthermore, below roughly 90 km, DSMC simulations are exceedingly expensive and the Navier-Stokes equations are applicable with the appropriate slip boundary condition [*Scalabrin* (2007)]. Nevertheless, entry trajectory data provide sufficient information to simulate the Apollo reentry flow above 90 km with the DSMC method and enable a sensitivity study on the

aerothermodynamics by varying physical phenomena in order to gain an understanding of their significance.

Unlike the wind-tunnel test conditions discussed in the previous chapter, the flight conditions involve a gas mixture and shock induced energy levels sufficient to incur chemical reactions. When significant, the chemical activity affects the shock layer flow and, hence, the momentum and energy transferred to the vehicle. The intensity of chemical activity is dependent on the density of the freestream flow; thus, it is relevant to examine whether chemical activity plays a significant role at the rarefied altitudes of the entry trajectory. At these altitudes, it is also relevant to examine the sensitivity of the aerothermodynamics to surface radiation and gas-surface accommodation. On the one hand, a surface radiation boundary condition, instead of an isothermal boundary condition, will result in a more realistic surface temperature distribution, which may or may not significantly affect the vehicle aerodynamics. On the other hand, gas-surface accommodation has a direct effect on the vehicle aerodynamics and varies with flow regime as the vehicle descends hypersonically into the atmosphere from the free molecular to the continuum regime. This variation and its effects are not fully understood. It is necessary to understand these phenomena at rarefied altitudes in order to correctly predict lift-to-drag ratio and trim angle-of-attack, which are prerequisite for trajectory planning and thermal protection design [*Crowder* (1969)]. In this chapter, simulations of the 110 km entry trajectory point of the Apollo 6 mission are examined. This altitude is selected because it involves a reasonable simulation expense for multiple cases. The simulations enable an assessment of the sensitivity of the respective aerothermodynamics to changes in surface radiation, gas-surface accommodation and

chemistry in the flow field due to the diffuse shock layer. To evaluate the effects of the changes in these physical mechanisms, Mach number contours, temperature contours, peak field temperatures, surface heating and aerodynamic coefficients are monitored. This study is presented in the following order: first, a general description of the simulations is given; second, the effects of varying gas-surface accommodation and wall temperature boundary conditions are analyzed; third, the effects of gas chemistry are discussed; and finally, a summary and conclusions are given.

4.2   General Description of the Simulations

Table 4.1 lists the relevant vehicle geometric parameters and freestream flow conditions, which remain constant throughout the sensitivity study. The dimensions of the ACM are based on *Bertin* (1994). However, after a further review of *Boylan and Griffith* (1968), *Hillje* (1967), *Lee and Goodrich* (1972), *Moss et al.* (2006) and *Park* (1990), it is recommended that this geometry be based on *Boylan and Griffith* (1968) in future flight simulations of the Apollo 6. Nonetheless, since this is a sensitivity study of the effects of physical mechanisms on the aerothermodynamics about the entire capsule,

Table 4.1   Flight conditions

Property	Value	Property	Value
d_{ref}	3.91 m	Kn	0.26
h	110 km	Gas [****]	4-species air
α	155°	$n_{N_2,\infty}$ [**]	1.05×10^{18} m^{-3}
V_∞ [*]	9.6 km/s	$n_{O_2,\infty}$	1.54×10^{17} m^{-3}
T_∞ [**]	265 K	$n_{N,\infty}$	5.94×10^{11} m^{-3}
Ma_∞ [***]	28.5	$n_{O,\infty}$	1.28×10^{17} m^{-3}
λ_∞	1.003 m		

[*]V_∞ is taken from the Apollo 6 trajectory;   [**]T_∞ and $n_{i,\infty}$ are taken from NRLMSIS-00
[***]Ma, λ_∞ and $Kn = \lambda_\infty / d_{ref}$ are computed with the above freestream data
[****]This becomes 5-species air when chemical reactions are activated, introducing NO
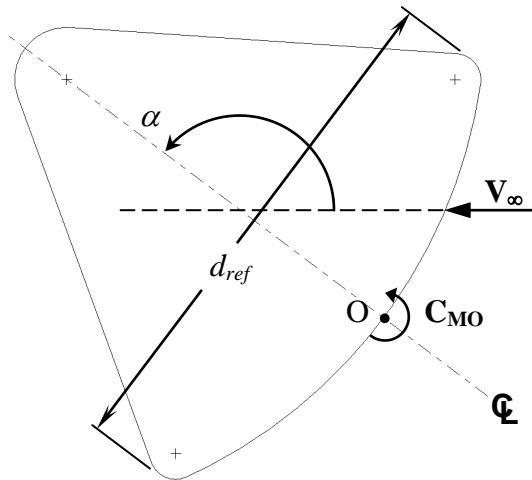
Figure 4.1   ACM reference geometry

the uncertainty in the aft nose radius, opposite to the heatshield, in the wake region does not play a significant role. The vehicle shape, angle-of-attack and pitching moment about the heatshield apex are illustrated in Fig. 4.1. At the 110 km altitude entry trajectory point, the ACM velocity is $\approx$ 9.6 km/s [*Lee and Goodrich* (1972)] and its angle-of-attack is $\approx$ 155° [*Hillje and Savage* (1968)]. Unknown freestream thermodynamic properties are determined with the help of the NRLMSIS-00 Earth atmosphere model [*Picone* (2002)]. The MONACO DSMC code, described in Chapter 2, is employed with the variable soft sphere collision model [*Koura and Matsumoto* (1992)] and the variable vibrational

Table 4.2   Typical Simulation Expense

Property	*Value*
Cells	489,055
Particles	$\approx$33,500,000
Reference time step	1.0×10^{-6} s
Number of time steps	40,000
Processors[*]	16
Wall Time	$\approx$15 hr

[*]1.4–1.8 GHz Opteron or Intel Itanium processors

energy exchange probability model [*Vijayakumar et al.* (1999)]. Several simulations of the ACM at the selected entry trajectory point are made, with varying physical mechanisms. The expense of a typical simulation is shown in Table 4.2. The simulations of the 110 km altitude trajectory point are less expensive than the three dimensional Apollo windtunnel test model simulations presented in Chapter 3, c.f. Table 3.3.

4.3   Sensitivity to Surface Conditions

The sensitivity study begins with a look into the effects of varying gas-surface accommodation and the temperature boundary condition, while maintaining an inert four species air model. The first physical mechanism examined is the gas-surface accommodation. The accommodation is based on the Maxwell gas-surface interaction model, described in Chapter 5. In this chapter, the model is modified to handle independent variation of the gas-surface accommodation for translational, rotational and vibrational energy modes by the accommodation coefficients a_M, a_{E_rot} and a_{E_vib}, respectively. a_M represents the probability of a diffuse reflection. If the molecule reflection is not diffuse, then it is specular. a_{E_rot} and a_{E_vib} represent the probability that the respective energy modes will be in thermal equilibrium with the solid surface, that is fully accommodated. The reflected molecule will have either full accommodation or no accommodation, that is no change, in the rotational and vibrational energy modes. Initially, full accommodation of the translational, rotational and vibrational energy modes is assumed. Then, partial accommodation of each energy mode is considered. This is performed by setting accommodation coefficients of translational, rotational and vibrational energy to 0.85, 0.10 and 0.01, respectively. The reduced accommodation values are selected according to the approximate relaxation time for each energy mode.

The relaxation times are related to the difference in energy between adjacent quantum energy states. The energy spacing of translational states is many orders of magnitude smaller than for rotational states, which are an order of magnitude smaller than for vibrational states. As a result, the relaxation time to reach translational equilibrium is beyond an order of magnitude smaller than the relaxation time to reach rotational nonequilibrium, which is at least an order of magnitude smaller than the relaxation time to reach vibrational equilibrium. Hence, the time it takes a gas molecule's vibrational energy to fully accommodate with the surface must be approximately an order of magnitude greater than the time its rotational energy takes to fully accommodate and so forth. This leads to the estimated ratio of accommodation levels between the energy modes.

In both the full and partial accommodation cases, an isothermal wall temperature is prescribed by assuming that the incident freestream kinetic energy is completely radiated at the surface according to the Stefan-Boltzmann law. That is,

$$\frac{1}{2} \rho_\infty V_\infty^3 = \varepsilon \sigma_{SB} T_w^4 \qquad (4.1)$$

where ε and σ_{SB} are the surface emissivity and the Stefan-Boltzmann constant, respectively. It is further assumed that the surface radiates as a black body, $\varepsilon = 1$. Thus, from Eqn. (4.1), a wall surface temperature of $T_w \approx 830\,K$ is specified for the isothermal wall. The second mechanism examined is the wall surface radiation. This is performed by repeating the previous cases with a simple radiative equilibrium wall boundary condition and comparing the results. In the radiative equilibrium wall boundary condition, the wall temperature is initially set to the isothermal wall temperature of the isothermal wall cases; then, the convective heat flux given by the DSMC method at a surface element,

71

labeled *i*, is assumed to be fully radiated by that element according to the Stefan-Boltzmann law. This assumption provides the wall temperature for the next time step, *n*+1, through

$$\dot{q}_{conv,i}^{n} = \varepsilon \sigma_{SB} \left(T_{w,i}^{n+1} \right)^{4} \tag{4.2}$$

However, when the convective heat flux results in a wall temperature less than the vehicle cabin temperature, assumed to be 300 K, the wall temperature is set to the assumed cabin temperature. In summary, the variations of gas-surface accommodation and wall surface temperature condition comprise four simulation cases. Table 4.3 assigns numbers to the simulation cases. To evaluate the effects of changing these surface conditions on the aerothermodynamics, Mach number contours, temperature contours, peak field temperatures, wall temperatures, aerodynamic coefficients and maximum Stanton number are monitored.

Table 4.3   Simulation cases of various surface conditions

Case	Gas-Surface Accommodation			Wall Temperature
	a_M	a_{E_rot}	a_{E_vib}	
Isothermal Wall				
1	1.00	1.00	1.00	$T_{w,i} = 830$ K
2	0.85	0.10	0.01	$T_{w,i} = 830$ K
Radiative Equilibrium Wall				
3	1.00	1.00	1.00	$T_{w,i}^{n} = \sqrt[4]{\dot{q}_{conv,i}^{n-1} / \sigma_{SB}}$
4	0.85	0.10	0.01	$T_{w,i}^{n} = \sqrt[4]{\dot{q}_{conv,i}^{n-1} / \sigma_{SB}}$

4.3.1 Effects on maximum field and wall temperatures

The sensitivity evaluations begin by looking at the effects on the maximum field and wall temperatures. Regarding the maximum flow field temperatures of the translational, rotational and vibrational energy modes, Table 4.4 below shows that decreasing the gas-

surface energy or thermal accommodation significantly increases the maximum field temperatures by at least 12% to as much as 57% with both the isothermal and the radiative equilibrium wall surface boundary conditions. In addition, larger reductions in rotational and vibrational energy accommodation result in larger increases in maximum temperatures. This effect agrees with the physical consequence of increased reflected gas molecular energy with a reduced gas energy accommodation with the vehicle surface. The increased reflected gas molecular or thermal energy is expressed by the larger maximum temperatures in the flow field. In contrast, switching from an isothermal wall to a radiative equilibrium wall reduces the peak field temperatures and affects them with a much smaller magnitude, from 0.3 to 12%. The reduction occurs because the radiative equilibrium wall condition reduces the initially assumed isothermal wall surface temperature and assumes that all the radiated energy escapes the simulation domain without being absorbed by the gas molecules in this domain.

Table 4.4   Sensitivity of maximum temperatures (K)

Case	Translational	Rotational	Vibrational	Wall Surface
Isothermal Wall				
1	37,023	5,810	2,377	830
2	41,443	7,797	3,352	830
Increase	12%	34%	41%	
Radiative Equilibrium Wall				
3	36,900	5,642	2,091	789
4	41,201	7,540	3,517	755
Increase	12%	34%	57%	− 4.3%
Effect of T_w				
Increase 1 to 3	− 0.3%	− 2.9%	− 12%	− 4.9%
Increase 2 to 4	− 0.6%	− 3.3%	− 1.6%	− 9.0%

Further details on the translational temperature results of these two cases are revealed by Figs. 4.2 (a) through (d). These figures further illustrate the more significant effects of reducing the gas-surface accommodation. The diffuse shock layer's thermal footprint of

(a) Case 1   (b) Case 2

Isothermal Wall

(c) Case 3   (d) Case 4
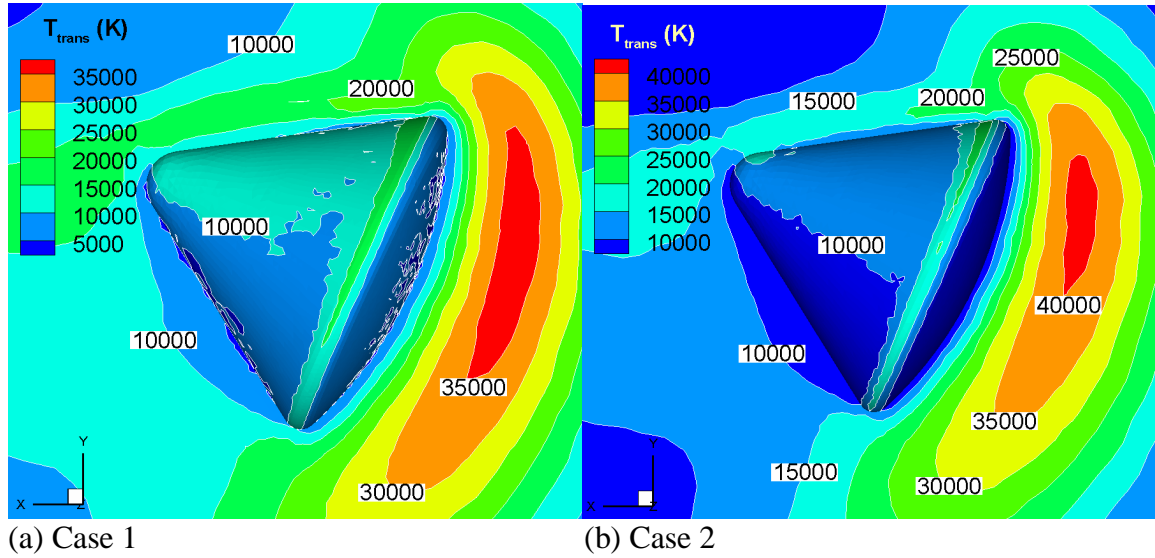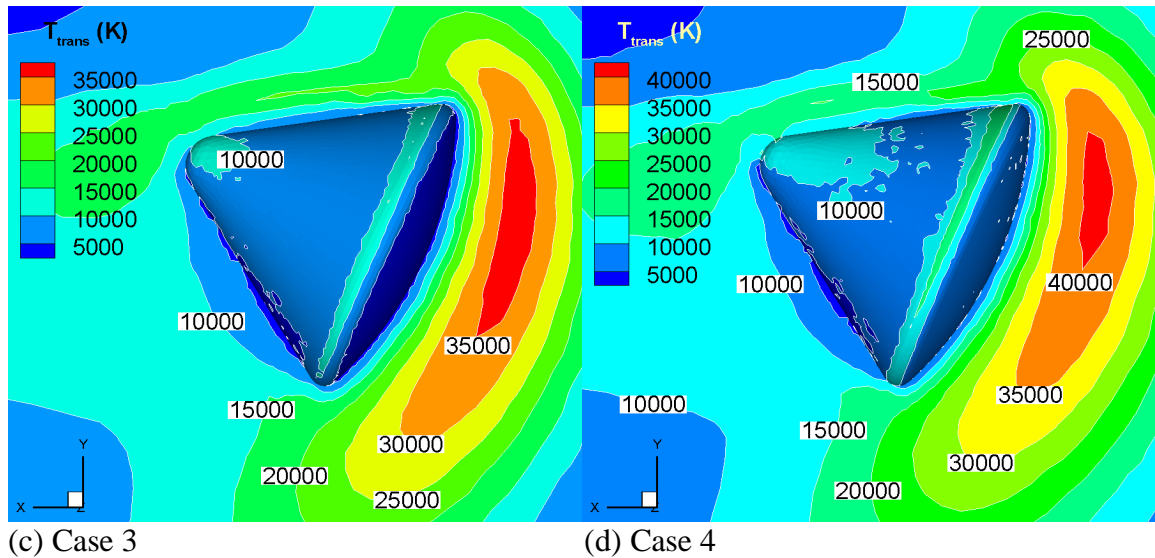
Radiative Equilibrium Wall

Figure 4.2   **Contour plots of translational temperature at symmetry boundary near the vehicle of three-dimensional ACM flight simulations associated with the various cases of wall surface conditions**

translational temperatures above 35,000 K is significantly larger for the cases with reduced gas-surface accommodation. With the radiative equilibrium surface boundary condition, the flow temperature distribution over the leeward facing surface involves lower translational temperatures than the isothermal case. In addition, the flow temperature distribution next to the radiative surface is sensitive to changes in gas-surface accommodation, whereas, with the isothermal surface, this distribution is obviously insensitive to changes in gas-surface accommodation.

Regarding the wall surface temperatures, Table 4.4, above, indicates that the peak surface temperatures are more affected by switching the wall temperature boundary condition more than by reducing gas-surface accommodation, although the effects are within the same order of magnitude. The effects of reducing the gas-surface accommodation, while maintaining a radiative equilibrium wall, on the wall surface temperature distribution are illustrated in Figs. 4.3 (a) and (b). This figure shows the average wall temperature contours based on the average convective heat flux over the specified steady-state period of the simulation. For both accommodation cases, the leeward side of the vehicle is essentially isothermal at the assumed cabin temperature of 300 K. The radiative wall partial thermal accommodation case results in slightly cooler surface temperatures over the heatshield. This effect agrees with the physical consequence of shorter residence times of the hot gas on the surface required for partial thermal accommodation.

It is also relevant to note the effects of changing the surface conditions on property contour plots over the entire computational domain surface of symmetry and on property profiles along a horizontal line upstream of the vehicle. These perspectives provide

75

(a) Case 3   (b) Case 4
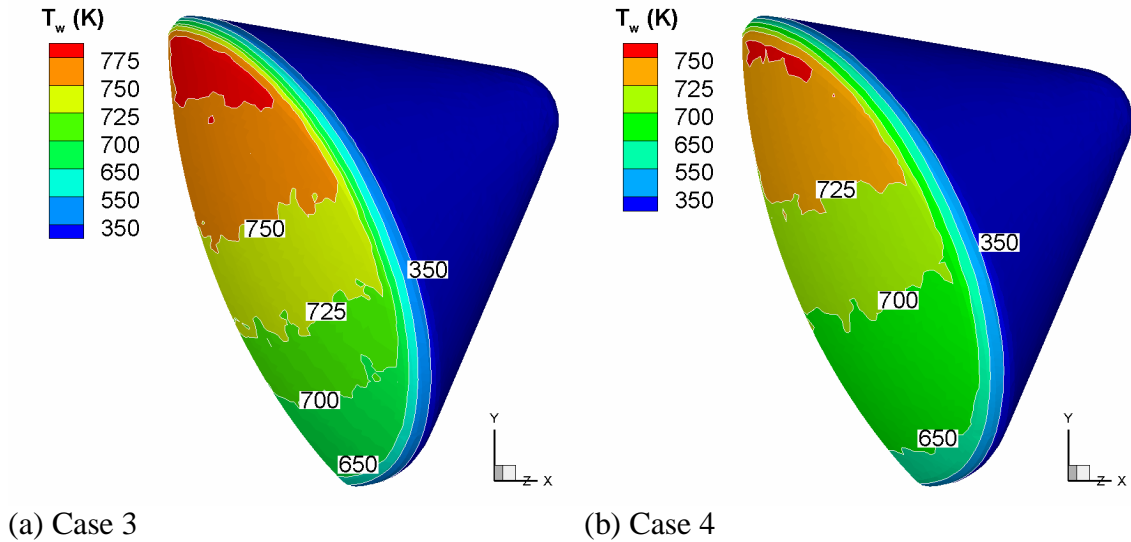
Figure 4.3   Contour plots of wall surface temperature of three-dimensional ACM flight simulations associated with cases having the radiative equilibrium wall

further information on the gas behavior. They also provide information on the vehicle's influence on the upstream flow field, referred to here as the "upstream domain of influence". (This is not to be confused with the domain of influence of the method of characteristics of supersonic continuum flow analysis. Although there are similarities the definition here is not intended to be universal.) This region extends from the vehicle out to the freestream. In continuum hypersonic flow this region is sharply defined by the start of the bow shock, however, in rarefied hypersonic flow the change in Mach number from the freestream value occurs gradually due to a diffuse bow shock. For DSMC simulations above a certain altitude or Knudsen number range, the upstream domain of influence can vary considerably and indicates the size of the required computational mesh upstream of the vehicle. The size of the domain downstream of the vehicle need only be large enough to contain outflow numerical vacuum effects behind the desired geometric region of analysis.

Figures 4.4 (a) through (d) display the entire computational domain surface of symmetry for each case. The upstream domain of influence of the vehicle on the surrounding gas translational temperature is increased when the thermal accommodation is reduced. This effect also agrees with the physical consequence of increased reflected gas molecular energy with a reduced thermal accommodation for the vehicle surface in this flow. The increased reflected gas molecular energy allows larger upstream distances across which information about the vehicle's presence may travel. However, changing the wall boundary condition from isothermal to radiative equilibrium has no significant effect on the upstream domain of influence of the vehicle on the surrounding gas translational temperature. Similar effects are observed on the vehicle upstream domain of influence on the surrounding gas Mach number.

(a) Case 1   (b) Case 2
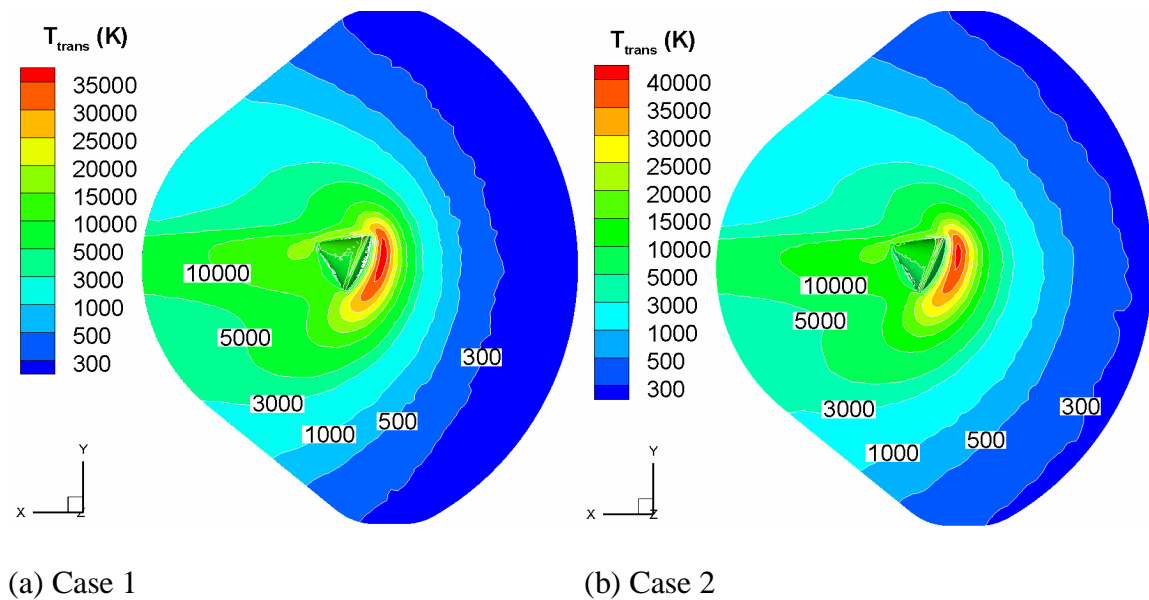
Isothermal Wall

Figure 4.4.   Contour plots of translational temperature at entire symmetry boundary of the three-dimensional ACM flight simulations associated with the various cases of wall surface conditions

77

(c) Case 3   (d) Case 4
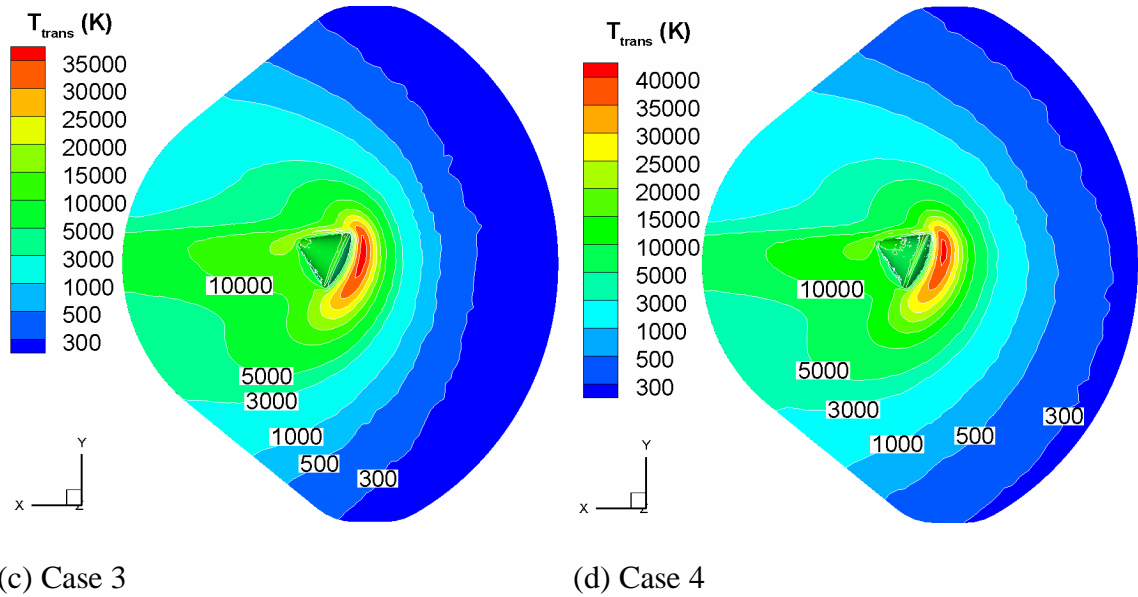
Radiative Wall

Figure 4.4   Concluded

A more detailed perspective is provided by the temperature and Mach number profiles along a horizontal line, defined by $y(x, z) = 1.3$ m, upstream of the vehicle ($x < 0$) and on the plane of symmetry ($z = 0$). (The origin of the coordinate system is labeled O in Fig. 4.1.) The horizontal line is located near the horizontal segment of the stagnation stream line, which changes slightly with each case. The stagnation streamline curves up near the surface to intersect the stagnation point at $y \approx 1.7$ m. The respective profiles are shown in Figs. 4.5 (a) through (d) where x is nondimensionalized by freestream mean-free-path λ_∞ and shifted such that it is zero at the vehicle surface because the horizontal line does not intersect the surface at the origin. The profiles provide a clear perspective on how decreasing the gas-surface thermal accommodation increases the gas energy ahead of the vehicle, including rotational and vibrational modes. The increases in gas energy extend to

the freestream boundaries of the full accommodation cases and, hence, cause the increases in the vehicle upstream domain of influence.
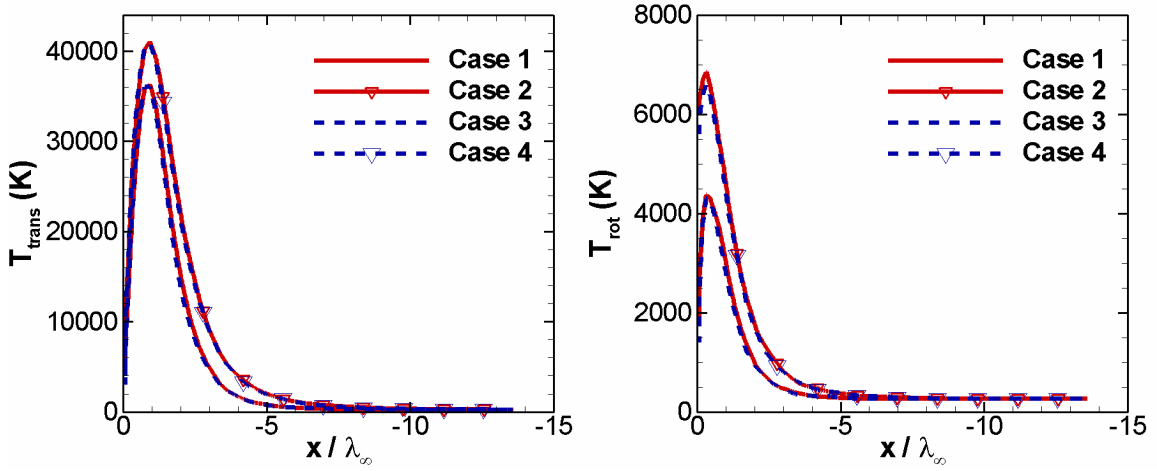
(a) *Translational temperature*

(b) *Rotational Temperature*
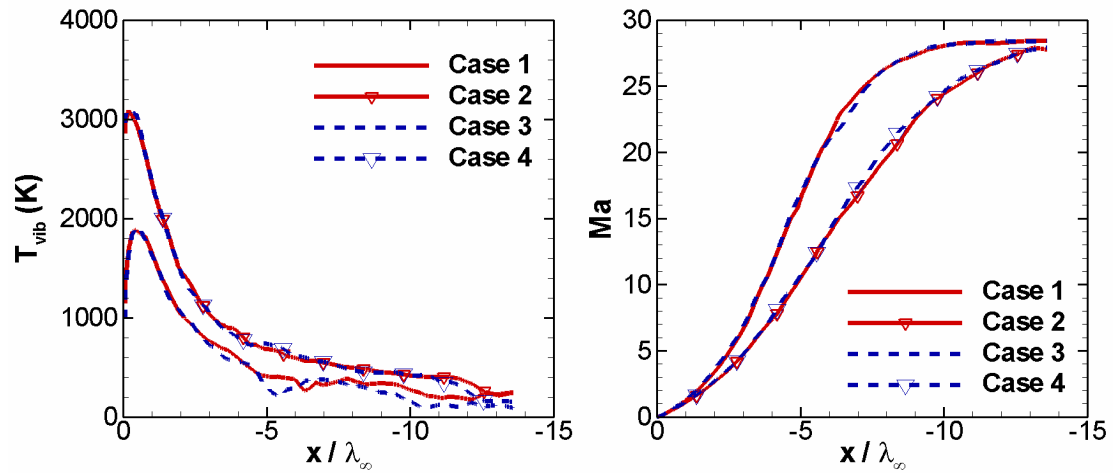
(c) *Vibrational temperature*

(d) *Mach number*

Figure 4.5 **Temperature and Mach number profiles along a horizontal line ahead of the ACM, $y(x<0, z=0) = 1.3$ m, of the three-dimensional flight simulations associated with the various cases of wall surface conditions**

4.3.2 Effects on ACM aerodynamics and surface heating

The sensitivity evaluations continue by looking at the effects of the wall conditions on the ACM aerodynamic coefficients and surface heating. The aerodynamic coefficients of lift, drag and pitching moment, and the maximum Stanton number are computed for each of the surface conditions and listed in Table 4.5. The reductions in gas-surface accommodation cause the aerodynamic forces and moment to increase because of the increase in gas energy about the vehicle, which causes the resultant aerodynamic force to increase in magnitude. Also, the increase in specular reflections, according to the Maxwell gas-surface interaction model, provides an increase in pressure force due to

Table 4.5   Sensitivity of aerodynamics and surface heating

Case	C_D	C_L	L/D	C_{MO}	St_{max}
Isothermal Wall					
1	1.66	0.231	0.139	0.111	0.829
pressure[*]	1.35	0.511		0.085	
shear	0.313	−0.280		0.025	
2	1.69	0.275	0.163	0.113	0.700
pressure	1.41	0.532		0.093	
shear	0.28	−0.257		0.021	
Increase (%)	1.58	18.8	17.0	2.42	− 15.5
pressure	3.77	8.84		6.46	
shear	−2.17	9.98		−3.96	
Radiative Equilibrium Wall					
3	1.67	0.232	0.139	0.111	0.858
pressure	1.35	0.513		0.085	
shear	0.314	−0.280		0.026	
4	1.69	0.274	0.162	0.114	0.712
pressure	1.41	0.531		0.093	
shear	0.278	−0.257		0.021	
Increase (%)	1.33	17.8	16.2	2.27	− 17.0
pressure	3.50	8.01		6.42	
shear	−2.17	9.76		−4.15	
Increase by changing T_w wall condition					
Increase 1 to 3	0.272 %	0.558 %	0.285 %	0.470 %	3.53 %
Increase 2 to 4	0.018 %	− 0.355 %	− 0.373 %	0.326 %	1.70 %

[*]pressure and shear components of C_D, C_L and C_{MO} are listed below the total values, percentage increases in these components are relative to total values of cases 1 or 3 depending on the wall condition

rectilinear impact. The aerodynamic forces are due to the pressure and shear stresses on the vehicle surface. The pressure and shear stresses are affected more by the increased gas energy ahead of the inclined heat-shield than over the leeward side because of the larger density ahead of the vehicle. The drag due to pressure is increased, while the drag due to shear is decreased. The net effect is an increase in the overall drag coefficient.

The increase in lift is partly due to an increase in pressure against the inclined heatshield. In regard to the shear stresses, the increase in lift indicates that the upward component of shear in the small region of the heatshield above the stagnation point is high enough to outbalance the downward component of shear in the larger area below the stagnation point. The larger increase in lift than in drag indicates that there are larger increases in positive vertical shear stress components on the part of the heat shield above the stagnation point, than increases in respective horizontal components in the direction of the drag force. In terms of Maxwell's gas-surface interaction model, the increase in lift is attributed to decreased backward scatter due to decreased diffuse reflections where specular reflections incur a lift force. This occurs throughout the inclined heatshield where the angle between the inward surface normal and the freestream is between zero and ninety degrees.

A significantly larger part of the pitching moment is due to pressure than to shear. The pitching moment due to pressure increases with the reduction in gas-surface accommodation, while the component due to shear decreases. The net effect is an increase in the pitching moment. The increase in pitching moment indicates that the pressure producing pitch-up moments referenced to point O outbalances the pressure producing pitch-down moments. The increased pitching moment means that the vehicle is

further from the trim angle-of-attack for the reduced gas-surface accommodation and greater control-system force is required to maintain the specified angle-of-attack.

The location of maximum Stanton number or heat flux is near the location of the stagnation point. Figure 4.6 below shows contour plots of vertical shear stress and the location of the maximum Stanton number for case 1. The location of the stagnation point is at the vehicle vertical plane of symmetry on the zero vertical shear stress contour, which is zero according to Tecplot contour generation; the cell-centered values come near to but do not actually reach zero. In Fig. 4.6, the stagnation point is at $y \approx 1.60$ m; this varies slightly among the cases. The location of the maximum Stanton number also varies slightly among the cases. The respective vertical coordinate y of each case is within 5% of the average, $y_{stag., avg.} = 1.67$ m. The maximum Stanton number, which is a measure of the heat flux from the gas to the surface, decreases with accommodation because less thermal energy is imparted onto the surface in order to accommodate the thermal energy
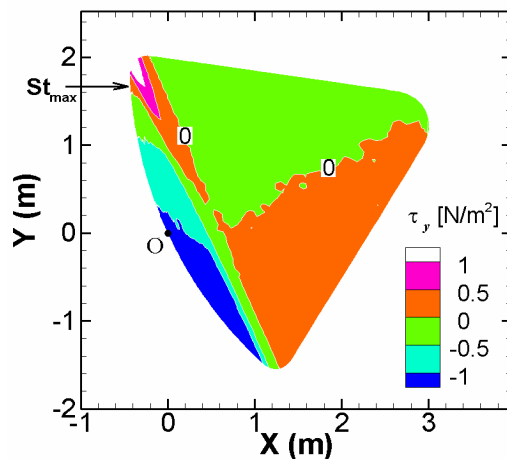
Figure 4.6 **Contour plots of vertical shear stress location of St_{max}, $y = 1.64$ m, from case 1**

of the gas with that of the surface. The decrease in surface heating accompanied by an increase in lift-to-drag ratio (L/D) agrees with studies by *Neumann* (1989), which suggest that increasing L/D decreases peak heating for certain configurations with $L/D < 1$. In the present study, L/D increases by about 17% from case 1 to case 2 and by about 16% from case 3 to case 4; the associated decreases in St_{max} are 16% and 17%, respectively. This demonstrates the sensitivity of the ACM aerodynamics and surface heating to changes in gas-surface accommodation at this flight condition.

In regard to the change in wall boundary condition from isothermal to radiative, the aerothermodynamic properties are affected much less, see the bottom of Table 4.5. As expected, the Stanton number is affected the greatest, though below 4%. The other properties are affected by less than 0.6%.

4.4   Sensitivity to Chemically Reacting Flow

The sensitivity study ends by examining the effects of introducing gas chemistry into the flow field. In this section, the results of case 4 are compared with the same simulation except with chemistry activated, denoted as case 5. For case 5, a set of 19 chemical reactions is activated using the TCE model. These include the dissociation and exchange reactions listed in Table 4.6. These reactions introduce a fifth species, namely, nitric oxide (NO). The dissociation reactions are written in an abbreviated form such that each reaction represents five reactions corresponding to each identity of species M. The recombination reactions, which are the reverse of the dissociation reactions, are excluded because the extremely small chance ($\sim 10^{-10}$) that a ternary collision will occur and lead to a recombination reaction within these flow conditions. The expense of the simulation is

Table 4.6   Chemical reaction mechanism

Dissociation Reactions	Exchange Reactions
$N_2 + M \rightarrow N + N + M$	$NO + O \rightarrow O_2 + N$
$O_2 + M \rightarrow O + O + M$	$N_2 + O \rightarrow NO + N$
$NO + M \rightarrow N + O + M$	$O_2 + N \rightarrow NO + O$
	$NO + N \rightarrow N_2 + O$
$M = N_2, O_2, NO, N$ or O	

similar to the inert case. Indeed, only a small quantity of chemical reactions occurs. During each time-step, there are about 33.6 million simulation particles. Among these particles only about 10,800 collisions occur throughout the simulation domain and only about 0.3% of these result in a chemical reaction.

The sensitivity evaluations of the influence of chemistry are processed by examining peak field and wall temperatures, and profiles of field temperatures, Mach number and species number densities. The peak field temperatures, exhibit 5% reductions due to the chemistry, as listed in Table 4.7. The peak wall surface temperature is not significantly affected. The small or insignificant changes are a consequence of the small quantity of chemical reactions due to the low pressure of the rarefied flow.

Table 4.7   Sensitivity of maximum temperatures (K) to flow chemistry

Case	Translational	Rotational	Vibrational	Wall Surface
4 (no chemistry)	41,201	7.540	3,517	755
5 (chemistry)	39,183	7,128	3,437	754
Increase	– 4.9 %	– 5.5 %	– 4.2 %	– 0.13 %

Property profiles along the line, $y(x<0, z=0) = 1.3$ m , described in Section 4.3.1, provide a more thorough observation. Figures 4.7 (a) through (d) are profiles of translational, rotational and vibrational field temperatures, and of Mach number. These

show that under these conditions chemical reactions only affect small regions near the peak field temperatures and do not significantly affect the velocity field.
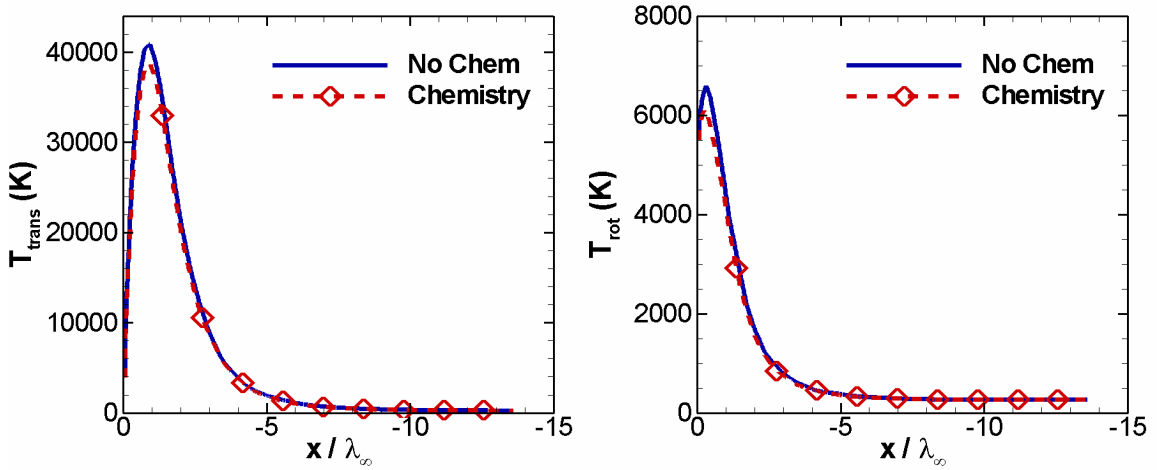
(a) *Translational temperature*

(b) *Rotational Temperature*
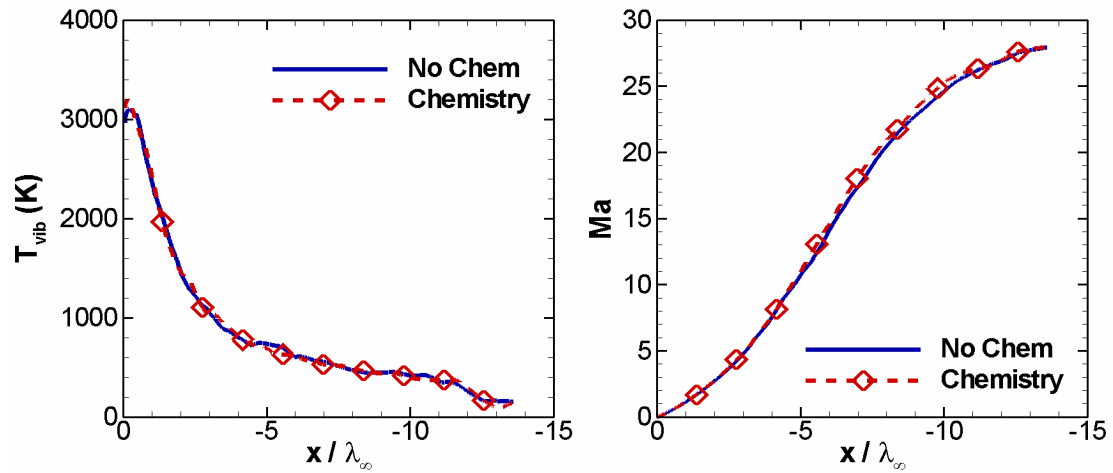
(c) *Vibrational temperature*

(d) *Mach number*

Figure 4.7 **Temperature and Mach number profiles along a horizontal line ahead of the ACM, $y(x<0, z=0) = 1.3$ m, of the three-dimensional flight simulations associated with cases 4 (no chemistry) and 5 (chemistry)**

Figures 4.8 (a) through (d), illustrate species number density profiles, excluding monatomic nitrogen for brevity. Increase in monatomic oxygen density suggests significant dissociation. The rise of nitric oxide density reveals a significant quantity of

(a) *diatomic nitrogen*

(b) *diatomic oxygen*

(a) *monatomic oxygen*

(b) *nitric oxide*
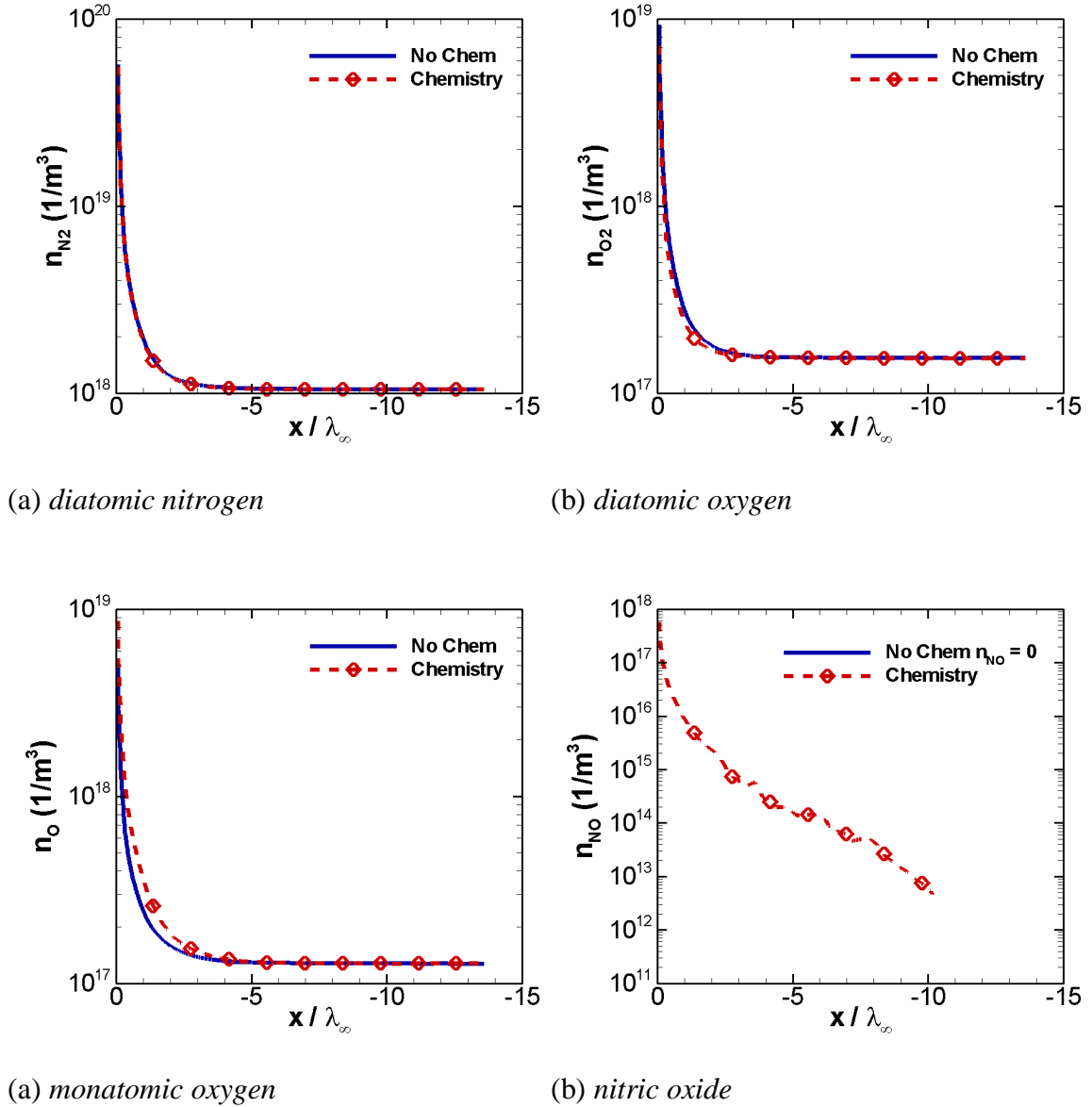
Figure 4.8   Species number density profiles along a horizontal line ahead of the ACM, $y(x<0, z=0) = 1.3$ m, of the three-dimensional flight simulations associated with cases 4 (no chemistry) and 5 (chemistry)

exchange reactions. Thus, the species profiles show evidence of diverse flow chemistry, nevertheless, the low pressures do not foster a sufficient quantity of reactions to significantly affect the ACM surface heating.

Finally, a comment is made about the sensitivity of flow chemistry on the vehicle aerodynamics and surface heating. The DSMC simulation with flow chemistry, case 5, produces the same aerodynamic coefficients and surface heating as case 4, to the indicated level of precision shown in Table 4.5 above. In conclusion, cases 4 and 5 of the three-dimensional DSMC simulations reveal that chemical reactions at the 110 km entry trajectory point of Apollo 6 play no significant role on the ACM aerodynamics and surface heating.

4.5   Chapter Summary and Conclusions

A sensitivity study was executed on the aerothermodynamics of the Apollo Command Module (ACM) at the 110 km entry trajectory point of the Apollo 6 mission. The study examined the significance of three physical mechanisms: gas-surface accommodation, surface radiation and flow chemistry. To evaluate the effects of the changes in these physical mechanisms, Mach number contours, temperature contours, peak field temperatures, surface heating and aerodynamic coefficients were monitored. The first two mechanisms were examined by four simulation cases entailing two gas-surface accommodation conditions and two surface temperature conditions. With an isothermal wall, it was found that decreasing gas-surface energy accommodation for the translational, rotational and vibrational components simultaneously from full to 85%, 10% and 1%, respectively, increases maximum field temperatures by 12%, 34% and 41%

for the translational, rotational and vibrational energy modes, respectively. In addition, this reduction in gas-surface accommodation significantly increased the vehicle's upstream domain of influence and significantly affected the ACM aerodynamics: lift increased by 18% and peak surface heating decreased by 18%. Similar changes were observed when reducing the gas-surface accommodation while maintaining a radiative equilibrium wall condition. In contrast, switching the surface boundary condition from isothermal to radiative equilibrium, while maintaining a constant gas-surface accommodation, did not significantly affect the flow field temperatures and upstream domain of influence. In addition, it only slightly affects the vehicle aerothermodynamics: the lift and maximum Stanton number were increased by about 1%. Nonetheless, the radiative equilibrium condition did provide more realistic wall surface temperature distributions for the simulations with little computational expense.

To examine the sensitivity of the aerothermodynamics to flow chemistry, one of the inert simulations was rerun with MONACO chemistry procedures activated. It was shown that chemical reactions only affected the diffuse shock region near the peak field temperatures, which were reduced by 5%. Because of the high temperatures a diverse set of chemical reactions did occur, nevertheless, the low pressures did not foster a sufficient quantity of reactions to significantly affect the ACM surface heating and aerodynamics. Because of the rapid rise in density and pressure with reduction in altitude from 110 km, chemistry may still play a significant role in DSMC aerothermodynamic analysis at lower altitudes, hence, the significance of chemistry is yet a relevant question at lower altitudes, although the DSMC simulations are significantly more expensive there.

In conclusion, the sensitivity study of the 110 km entry trajectory point of the Apollo 6 revealed that: changes in the gas-surface thermal accommodation significantly affect the aerothermodynamics; the addition of surface radiative equilibrium does not significantly affect the aerothermodynamics; and the inclusion of chemistry does not significantly affect the aerothermodynamics. Thus, because of the significance of gas-surface interactions found under these reentry conditions and because the behavior of gas-surface interactions under rarefied hypersonic conditions is not well understood, the remaining research in this thesis was directed toward improving the understanding and simulation of gas-surface interactions under hypersonic rarefied conditions. The next chapter presents an effort toward this goal.

CHAPTER V

ASSESSMENT OF GAS-SURFACE INTERACTION MODELS

5.1   Introduction

The previous chapter demonstrated the significance of gas-surface interactions on the aerothermodynamics of space capsule reentry. Aerothermodynamics is governed by the momentum and energy transferred from the incoming gas flow onto the surface of the vehicle. These transfers are governed by the collisions between the gas molecules and the solid surface. The collision process between a gas molecule and a solid surface is termed a gas-surface interaction. In kinetic theory, the gas-surface interaction forms a boundary condition between the gas molecules and the solid surface. For scales relevant to kinetic theory, the gas-surface interactions are usually modeled with parameters having macroscopic character, in order to have manageable and efficient calculations. The smallest gas-surface interaction spatial scale considered in this study is on the order of 10 μm, based on the minimum computational mesh cell size adjacent to the surface. Gas-surface interaction models for macroscales can also be augmented by special use of molecular dynamics [*Tsuboi and Matsumoto* (2001)].

Although various gas-surface interaction models have been proposed over the past century and a half, the validity of these models remains tenuous for hypersonic rarefied flow conditions. The study in this chapter employs numerical simulation, using the Direct Simulation Monte Carlo (DSMC) method, to scrutinize two of the most common gas-surface interaction models used with the DSMC method: the Maxwell model, and the Cercignani, Lampis and Lord (CLL) model. In the literature, comparisons of flow field properties between DSMC and laboratory data of rarefied hypersonic flow are uncommon. Hence, this study is also intended to generate new comparisons of this kind. In particular, the study compares shock or boundary layer properties between DSMC and existing windtunnel data of rarefied hypersonic flow near the leading edge of a flat plate. These comparisons involve the assessment of the prediction capabilities of the gas-surface interaction models through parametric analysis of boundary layer velocity profiles. In addition, the study examines probability distribution plots of the molecular velocity components at specified points in the flow field, and of molecular angle of reflection at specified points on the solid surface. The study is presented in the following order: first, a review of gas-surface interactions models is presented; second, a mathematical description of the two common models is laid out; third, comparisons are made between DSMC and compressible boundary layer theory; fourth, the parametric analysis is presented using contour plots, molecular velocity distributions and boundary layer velocity profiles; fifth, an examination of the effects of seeded iodine is reported; sixth, an analysis of nonequilibrium within the boundary layer is presented; seventh results are presented of DSMC Apollo 6 flight simulations using the Maxwell and CLL gas-surface interaction models; and finally, the results and conclusions are summarized.

5.2 A Chronicle of Models since Maxwell

Historically, the first gas-surface interaction model for kinetic theory is the model developed by *Maxwell* (1879). It considers two kinds of interactions, the specular and diffuse interactions, which are the result of a molecule encountering a perfectly reflecting or a perfectly absorbing surface, respectively. A specular interaction or reflection occurs when an incident molecule collides with the molecular structure of a solid surface in such a way that it rebounds elastically as if hitting a flat surface. This type of collision occurs when the gas molecule collides with a peak of the solid surface molecular structure, assuming the gas and solid molecules are rigid elastic spheres. The collision results in an inversion of the surface normal component of the molecule's incident velocity and no change in its tangential components. Thus, the angle of reflection is the same as the angle of incidence. A diffuse interaction occurs when an incident molecule interacts with the molecular structure of the solid surface in such a way that it attains thermal equilibrium with the surface and then evaporates from the surface according to the Maxwellian velocity distribution at the local surface temperature. The Maxwell model considers a fraction a_M of the incident molecules to be temporarily absorbed by the surface and then reflected diffusely from the surface; the remaining incident molecules are assumed to reflect specularly.

Scattering distributions, that is, probability distribution plots of gas-surface reflection or scattering angle θ_r, the angle between the surface horizon and the molecular velocity upon departure from the surface, illustrate the scattering trends of gas molecules reflected from the solid surface. Polar plots of the scattering distribution predicted by the Maxwell model, for a beam of molecules targeted onto a solid surface at a specified angle of

incidence, has a sharp oval due to the specular reflections, as shown by Figure 5.1 (a), along with a circular shape due to the diffuse reflections, as shown by Figure 5.1 (b).

<div align="center">(a) specular component   (b) diffuse component</div>
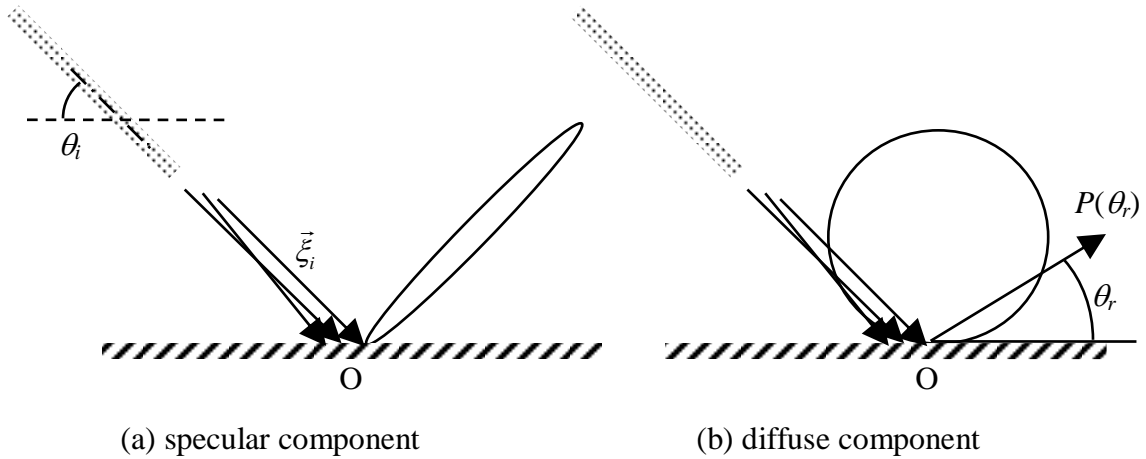
Figure 5.1   **Schematic polar plots illustrating scattering distribution predicted by Maxwell's model for a beam of molecules targeted onto a flat surface at a specified angle-of-incidence** θ_i

The composite distribution will then be a circular shape with a protruding peak. If the molecules in the beam are all traveling at the same velocity, then the peak is a line at the specular angle of reflection. However, contrary to the expected distributions given by the Maxwell model, molecular beam experiments, e.g., *Schaaf* (1963), *Hinchen and Foley* (1966), and *Knetchel and Pitts* (1969), have shown scattering distributions to be petal-shaped rather than a composition of a circle and a sharp oval. Partly because of molecular beam experimental findings, various models have been developed to match the observed scattering distributions. Some of these models also aim at handling non-uniform gas-surface accommodation, i.e., accommodation dependent on local surface properties such as inclination angle. For convenience, interaction parameters unique to the model are commonly employed, in order to examine the model parametrically against laboratory results.

Because Maxwell's model proved suitable for low speed experiments, such as *Millikan* (1923), the development of gas-surface interaction models received little attention from the inception of Maxwell's model until satellites began orbiting the Earth and the problem of free molecular drag brought attention to them. In 1959, *Schamberg* proposed a surface interaction model for analyzing free molecular flow drag on satellites traveling at "hyperthermal" speeds, speeds exceeding the mean thermal speed of the rarefied gas by six times. This model contains three interaction parameters: the energy accommodation coefficient, a special exponent to relate incident and reflected directions, and the "beam width" angle. It is an improvement over Maxwell's model in that it explicitly considers local gas-surface interaction conditions; however, it is cumbersome and it assumes a uniform re-emission speed for all directions.

A couple of years later, at the second international symposium on rarefied gas dynamics, *Nocilla* (1961) reported a model intended for free molecular flow conditions where the velocity distribution of reflected particles is assumed to follow a shifted or "drifting" Maxwellian. Then in 1963 at the same biennial symposium, *Nocilla* followed up with a report showing that his model fit closely to laboratory results of scattering distributions at certain conditions. His model is fitted by varying the reflected molecular speed ratio and reflected bulk velocity angle relative to the surface normal; an equation for the energy accommodation coefficient in terms of these parameters is listed near the end of that report. Although this model makes improvements in mathematical construction, Nocilla's model has a major gap by having no correlation between the incident and reflected velocity distributions.

In 1968, *Hurlbut and Sherman* reported an update to Nocilla's model by connecting the incident and reflected distributions. They assume a drifting Maxwellian for the incident velocity distribution, and relate the incident distribution to Nocilla's reflected distribution by equating the inbound and outbound number fluxes. This model, known as the Hurlbut-Sherman-Nocilla (HSN) model, utilizes the energy accommodation coefficient, reflected molecular speed ratio and reflected bulk velocity angle for parametric analysis. In a 1992 report, *Hurlbut* lays out relations for the normal and tangential momentum accommodation coefficients in terms of these parameters. Nevertheless, the way the model connects the incident and reflected fluxes does not generally agree with the principle of detailed balance for gas-surface interactions.

Knowledge of the standard interaction parameters allows accurate calculations of aerodynamic and heat transfer coefficients for bodies in free molecular or collisionless flow. For rarefied flows involving a significant amount of intermolecular collisions, it is necessary to have knowledge of the re-emitted molecular property distributions. Each gas-surface interaction model mentioned hitherto provides distributions; however, only Maxwell's model generally satisfies the reciprocity principle, defined in Section 5.3.2. Under the assumption of local equilibrium, the distributions need to satisfy the principle of reciprocity, which is the principle of detailed balance for gas-surface interactions. A couple of reports that provide theoretical descriptions of the principle are given by *Kuščer* (1971) and *Wenaas* (1971). This principle is fundamental to a formal mathematical approach for relating the reflected distributions to the incident distributions called scattering kernel theory, formally presented for example in the publications of *Cercignani* (1969) and *Kuščer* (1971). At the cost of some restrictions to the model,

conformation to the reciprocity principle allows for the application of the H-theorem to gas-surface interactions, a symmetrized scattering kernel and a simplified boundary condition.

In 1971, *Cercignani and Lampis* initially proposed a model, known as the CL model, which satisfies the fundamental scattering kernel principles. The CL model involves the tangential momentum and normal kinetic energy accommodation coefficients, and performs respectably against laboratory results [*Cercignani and Lampis* (1971); *Cercignani and Frezzotti* (1989)] under certain high speed rarefied flow conditions. Although it compares well only within a limited range of laboratory conditions, the CL model is theoretically sound and relatively simple. A couple of newer kernels intended to extend the applicability of the CL model are given by *Cercignani et al.* (1995) and *Cercignani and Lampis* (1997). However, these two kernels employ interaction parameters that lack clear physical meaning and provide only marginal improvements in limited comparisons with laboratory experiments. Evidently, a desired empirical interaction model is in terms of empirical factors or parameters with clear physical interpretations; two or three of these parameters allow the kernel to have reasonable agreement with laboratory results over a sufficient range of conditions. In this sense, the original CL model has not yet been surpassed as the best empirical interaction model for engineering analysis and remains suitable for theoretical studies *Sharipov* (2001).

Twenty years after the CL model was initially published, a transformation of the CL model for use with the DSMC method was laid down by *Lord* (1991). This transformation is referred to as the CLL model. The transformation extends the CL model to handle rotational energy exchange between the gas and the surface. Later, *Lord* (1991

and 1995) further extended the model to handle vibrational energy exchange and a broader range of scattering states. One of these states is diffuse scattering with partial thermal energy accommodation. Indeed, there is no physical reason why an incident molecule has to reflect specularly with a single encounter with the molecular structure of the surface. The CLL model has now gained wide acceptance; examples of recent applications are reported by *Ketsdever and Muntz* (2001), *Santos* (2006) and *Utah and Arai* (2002).

The DSMC method, which reached common acceptance by the 1980s, relies on gas-surface interaction models at the surface boundaries of the computational domain. For sufficiently low Knudsen and Mach numbers, the diffuse scattering model suffices. Outside these conditions, such as the initial phase of spacecraft reentry, it is necessary to implement a more sophisticated model for the reasons mentioned above. Probably the two most common models presently in use with the DSMC method are Maxwell's model and the CLL model. It is these two models which are examined in this study. Before proceeding further into the present study, a couple of newer developments are briefly described to complete this chronicle.

The gas-surface interaction models mentioned so far are based on macroscopic description. They depend on only a few interaction parameters with values determined by fitting the models to experimental results. With the continual improvement of advanced computing systems, the ability to delve into a more detailed phenomenological description is beginning to become tractable. Two approaches have been taken based on separate theoretical grounds. *Agbormbai* (1988 and 2001) has made efforts toward maturing an approach based on statistical mechanics. This approach conforms with

reciprocity, involves ensemble mathematics, enables the specification of a surface energy distribution and is suitable for DSMC. It involves an ajustable parameter to handle the scattering from specular to diffuse. It is considered as a generalized Cercignani approach. However, the approach has been shown to give unrealistic scattering distributions [*Lord* (1991)] and has yet to fully mature and gain popularity. *Yamanishi et al.* (1999) have developed a multistage gas-surface interaction model for DSMC. In this approach, scattering parameters are determined from independent molecular dynamics (MD) simulations. In the DSMC simulation, some of the MD based scattering parameters are employed with model equations to determine translational and rotational energy exchange between gas molecules and the solid surface, which enables the calculation of reflected velocity in the plane defined by the surface normal and the incident molecule direction. To determine the respective out-of-plane scattering, the procedure employs a model potential energy surface derived from other MD based scattering parameters. Molecules then scatter away from the surface, scatter onto another section of the surface or are "physisorbed" by the surface. The physisorbed molecules are assumed to eventually emerge diffusely from the surface. For maintaining equilibrium between a stationary equilibrium gas and a solid surface, diffuse reflection is imposed because the approach does not generally satisfy reciprocity. With a good molecular dynamics database the model has been shown to closely agree with laboratory scattering experiments. This model also has yet to commonly appear in engineering applications.

5.3   Mathematical Description of Two Modeling Concepts

The various gas-surface interaction models that have been proposed since Maxwell's model have resulted in a couple of well established concepts presented here. These

concepts are used in describing the two common gas-surface interaction models examined in this study.

5.3.1 Interaction parameters

Parameters employed in gas-surface interaction models are called interaction parameters. For larger than the nanometer scale, these parameters are relevant to a macroscopic description; typically, they are accommodation coefficients. An accommodation coefficient is a numerical description about the degree to which a flow of gas accommodates kinetically or thermally with a solid surface, while interacting with the surface. The accommodation coefficient of molecular property Q is defined in terms of incident and reflected fluxes as follows [*Schaaf and Schambré* (1961); *Gombosi* (1994)]:

$$a_Q = \frac{\Phi_i^Q - \Phi_r^Q}{\Phi_i^Q - \Phi_w^Q} \tag{5.1}$$

where Φ_i^Q and Φ_r^Q are the incident and reflected fluxes of Q, respectively, and Φ_w^Q is the reflected flux of Q corresponding to full accommodation. Common examples of Q are the total energy E, normal momentum $m\xi_n$, and tangential momentum $m\xi_t$. The total energy, normal momentum and tangential momentum accommodation coefficients are defined, with the usual notation, by $\alpha \equiv a_E$, $\sigma_n \equiv a_{m\xi_n}$ and $\sigma_t \equiv a_{m\xi_t}$, respectively.

5.3.2 Scattering kernel

In kinetic theory analysis, the gas-surface interaction model is used as a boundary condition. A formal mathematical construct for a gas-surface interaction model is the scattering kernel formulation, outlined for example by *Cercignani* (1972). A scattering kernel $K\left(\vec{\xi}_i, \vec{\xi}_r\right)$ represents the probability density that an incident molecule with

velocity $\vec{\xi}_i$ is reflected with velocity $\vec{\xi}_r$ at essentially the same time and place. It bridges the velocity distribution functions, $f_i(\vec{\xi}_i)$ and $f_r(\vec{\xi}_r)$, of the incident and reflected molecules, respectively, through the following integral transform:

$$\xi_{n,r} f_r(\vec{\xi}_r) = \int_{\xi_{n,i} < 0} |\xi_{n,i}| f_i(\vec{\xi}_i) K(\vec{\xi}_i, \vec{\xi}_r) d\vec{\xi}_i \qquad (5.2)$$

where each gas-surface interaction is independent of others and the average interaction time is small relative to the temporal evolution of *f*. In addition, the scattering kernel satisfies the following three criteria: positivity, normalization and reciprocity. These criteria are expressed mathematically as follows:

$$K(\vec{\xi}_i, \vec{\xi}_r) \geq 0 \qquad (5.3)$$

$$\int_{\xi_{n,r} > 0} K(\vec{\xi}_i, \vec{\xi}_r) d\vec{\xi}_r = 1 \qquad (5.4)$$

$$|\xi_{n,i}| f_M(\vec{\xi}_i) K(\vec{\xi}_i, \vec{\xi}_r) = |\xi_{n,r}| f_M(\vec{\xi}_r) K(-\vec{\xi}_i, -\vec{\xi}_r) \qquad (5.5)$$

where f_M is the Maxwellian velocity distribution in equilibrium with the solid surface:

$$f_M(\vec{\xi}) d\vec{\xi} = (2\pi R_G T_w)^{-\frac{3}{2}} \exp\left(-\frac{\xi^2}{2 R_G T_w}\right) d\vec{\xi} \qquad (5.6)$$

The product $f(\vec{\xi}) d\vec{\xi}$ is the probability of any given molecule to have velocity $\vec{\xi}$ within the range $\vec{\xi}$ and $\vec{\xi} + d\vec{\xi}$. The reciprocity condition [*Wenaas* (1971); *Kuščer* (1971)], Eqn. 5.5, is the equilibrium condition for gas-surface interactions. It must be satisfied when the flow is in equilibrium with the solid surface.

5.4 Mathematical Description of Two Common Models in Use with DSMC

5.4.1 Maxwell model

The most common model in use with the DSMC method is the Maxwell model. It has a scattering kernel which satisfies positivity, normalization and reciprocity, and is written as follows [*Cercignani* (1969)]:

$$K_M\left(\vec{\xi}_i, \vec{\xi}_r\right) = \left(1 - a_M\right)\delta\left(\vec{\xi}_i - \vec{\xi}_{r,specular}\right) + a_M f_M\left(\vec{\xi}_r\right)\left|\vec{\xi}_r \cdot \mathbf{n}\right| \tag{5.7}$$

where $\vec{\xi}_{r,specular}$ is the molecular velocity of specular reflection. a_M is Maxwell's fraction as described in Section 5.2. It is an accommodation coefficient that indicates the probability of a diffuse reflection and does not represent a ratio of fluxes. In the implementation for the MONACO DSMC code, a reflected molecule's internal energy for a diffuse reflection is computed based on thermal equilibrium with the local surface temperature. For a specular reflection, the molecule's internal energy for a specular reflection is assumed unchanged. In other words, in MONACO $a_{E\_int} = a_M$ for the Maxwell model.

5.4.2 Cercignani, Lampis and Lord model

As discussed in section 5.2, the best analytical gas-surface interaction model, which has been shown to match some laboratory scattering distributions, is the CL model because it involves well defined interaction parameters, namely, parameters that can be expressed in the form of Eqn. (5.1), and it involves a well defined mathematical framework, namely, the scattering kernel construction. The CL model interaction parameters are the accommodation coefficient for the tangential momentum $\sigma_t \equiv a_Q$,

where $Q = m\vec{\xi} \cdot \mathbf{t}$, and the accommodation coefficient for the normal part of the kinetic energy $\alpha_n \equiv a_Q$, where $Q = \frac{1}{2}m\left(\vec{\xi} \cdot \mathbf{n}\right)^2$. The scattering kernel has the following form:

$$K_{CL}\left(\vec{\xi}_i, \vec{\xi}_r\right) = \frac{\left[\alpha_n \sigma_t \left(2 - \sigma_t\right)\right]^{-1}}{2\pi\left(R_G T_w^2\right)} \xi_{n,r} \exp\left(-\frac{\xi_{n,r}^2 + \left(1 - \alpha_n\right)\xi_{n,i}^2}{2\alpha_n R_G T_w}\right)$$
$$\times \exp\left(-\frac{\left[\vec{\xi}_{t,r} - \left(1 - \sigma_t\right)\vec{\xi}_{t,i}\right]^2}{2\sigma_t \left(2 - \sigma_t\right)R_G T_w}\right) I_0\left(\frac{\sqrt{1 - \alpha_n}\,\xi_{n,r}\xi_{n,i}}{\alpha_n R_G T_w}\right) \tag{5.8}$$

where $\xi_{n,i} < 0$; $\xi_{n,r} > 0$; $0 \le \sigma_t \le 2$; $0 \le \alpha_n \le 1$; I_0 is the modified Bessel function of the first kind and of zeroth order; and $\vec{\xi}_t$ is the sum of the tangential components of velocity.

The CL kernel, the scattering kernel of the CL model, is implemented into DSMC code by a simple algorithm, with a level of complexity not much greater than the implementation of the Maxwell model. Lord originally made the transformation to this algorithm with the help of a graphical representation of the CL model [*Lord* (1991)]. This algorithm forms the basic Cercignani, Lampis and Lord (CLL) model and is commonly implemented into DSMC. Table 5.1 presents the algorithm. These equations are employed by the MONACO DSMC code. In these equations, $\alpha_t \equiv a_Q$, with $Q = \frac{1}{2}m\left(\vec{\xi} \cdot \mathbf{t}_i\right)^2$, where $\mathbf{t}_i$ is any surface tangent vector. In other words, α_t is the accommodation coefficient for the part of the kinetic energy along any tangent to the surface; it is assumed independent of direction along the surface.

Table 5.1 **Algorithm equations of the CLL model: reflected molecular velocity components relative to local surface unit vectors**

Normal Component	Tangent 1 Component	Tangent 2 Component
$r_1 = \sqrt{-\alpha_n \ln x_1}$	$r_3 = \sqrt{-\alpha_t \ln x_3}$	$r_5 = \sqrt{-\alpha_t \ln x_5}$
$\theta_2 = 2\pi x_2$	$\theta_4 = 2\pi x_4$	$\theta_6 = 2\pi x_6$
$\xi_{n,m} = \left\lvert \xi_{n,i}/\xi'_{mp,w} \right\rvert \sqrt{1-\alpha_n}$	$\xi_{t,m} = \left\lvert \xi_{t1,i}/\xi'_{mp,w} \right\rvert \sqrt{1-\alpha_t}$	$\xi_{t2,r} = \xi'_{mp,w} r_5 \cos\theta_6$
$\xi_{n,r} = \xi'_{mp,w} \sqrt{r_1^2 + \xi_{n,m}^2 + 2 r_1 \xi_{n,m} \cos\theta_2}$	$\xi_{t1,r} = \xi'_{mp,w}\left(\xi_{t,m} + r_3 \cos\theta_4\right)$	

Auxiliary: x_i are random numbers uniformly distributed between 0 and 1;

$$\xi'_{mp,w} = \sqrt{2 R_G T_w}\,; \qquad \alpha_t = \sigma_t\left(2 - \sigma_t\right)$$

5.5 Flat Plate Windtunnel Test Simulations Using the Two Models

5.5.1 General description

To examine the gas-surface interaction models, this research involves computer simulations of existing windtunnel tests examining rarefied hypersonic flow over a flat surface or plate. The windtunnel tests, reported by *Cecil and McDaniel* in 2005, use planar laser induced fluorescence (PLIF) of seeded iodine, within a free jet expansion of nitrogen, to measure boundary layer flow properties. For details of the windtunnel test section apparatus, including the geometry of the flat plate windtunnel model refer to the paper by *Cecil and McDaniel* (2005).

The computer simulations of the flow-field are performed assuming two-dimensional flow. In addition, they use rectangular spatial domains that cover a region near the leading edge of the flat plate, which includes an adequate number of windtunnel test measurement locations. Each domain is divided into quadrilateral cells or a mixture of triangular and quadrilateral cells to form two-dimensional computational meshes. The

cells have sizes on the order of the local mean-free-path, according to the DSMC constraint. Throughout each mesh, a uniform particle weight W_p is assigned. The meshes are generated with *HyperMesh* (2004) and converted to MONACO readable format with an in-house grid-conversion code.

To simulate Cecil and McDaniel's experiment, pure nitrogen is initially assumed. The corresponding input parameters are listed in Table 5.2. The variables introduced in the table are: the number of rotational energy degrees of freedom ζ_{rot}, the number of vibrational energy degrees of freedom ζ_{vib}, the characteristic temperature of vibration θ_{vib},

Table 5.2   Physical input parameters for pure nitrogen DSMC simulation of flat plate windtunnel test

Species Data		*Collision Cross-Section Data*	
Species	N_2	$\delta_{diameter}$	4.11×10^{-10} m
MW	28.01	ω_{11}	0.7
ζ_{rot}	2.0		
ζ_{vib}	0.0		
θ_{vib}	3390 K		
T^*	91.5 K	*Solid Surface Data*	
$Z_{rot,\infty}$	18.1	T_w	300 K

the characteristic temperature of the intermolecular potential T^*, the maximum rotational collision number $Z_{rot,\infty}$, and the viscosity index of the VHS collision model ω_{11} for collisions between nitrogen molecules.
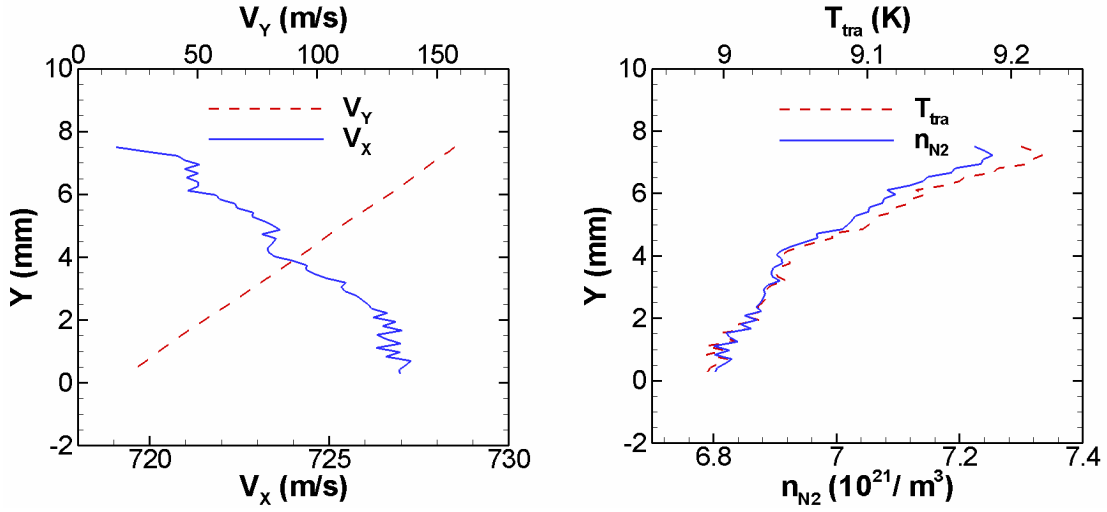
(a) *Velocity*   (b) *Temperature and number density*

**Figure 5.2   Nonuniform inflow conditions for DSMC simulation
of flat plate windtunnel test**

The inflow properties are shown in Figs. 5.2 (a) and (b). The inflow velocity profiles are provided by Cecil and McDaniel. The translational temperature and number density inflow profiles are calculated from the inflow velocity profiles and the windtunnel test reservoir temperature and pressure, $T_0 = 300$ K and $p_0 = 1.79$ atm, respectively. This calculation assumes that the reservoir contains an ideal gas and that it is expelled isentropically as a free jet expansion. The global Knudsen number, based on the inflow center-line (ICL) mean-free-path ($\lambda_{ICL} \approx 0.08$ mm) and the flat plate length, is about 0.004, which is in the transitional rarefied regime.

Using these flow conditions, simulations are made with the Maxwell gas-surface interaction model, at various values of Maxwell's fraction, $a_M = 0, 0.25, 0.50, 0.75$ and 1.00. Simulations are also made with the CLL gas-surface interaction model, at various values of tangential momentum accommodation, $\sigma_t = 0, 0.25, 0.50, 0.75$ and 1.00, with

full normal kinetic energy accommodation, $\alpha_n = 1.00$. In addition, the sensitivity to normal kinetic energy accommodation is examined with similar levels of accommodation, $\alpha_n = 0$, 0.25, 0.50, 0.75 and 1.00, while maintaining zero tangential momentum accommodation, $\sigma_t = 0$. Each of the simulations with the CLL model assumes full internal energy accommodation, $a_{E\_int} = 1$. All of the pure nitrogen simulations require computational parameters similar to those summarized in Table 5.3.

Table 5.3   **Typical computational properties of a pure N$_2$ simulation of the flat plate windtunnel test**

W_p	1.0×10^{12}	Time-step size	1.0×10^{-8} sec
Particles	~1,915,000	Time-steps	75,000
Cells	19,067	Wall time	~3.5 hr
Processors[*]	4		

[*]1.4GHz AMD Opteron 240 or 2.8GHz AMD Opteron 254, 1GB RAM per processor

5.5.2 Comparisons with compressible boundary layer theory

Before presenting the comparisons between DSMC and the windtunnel data, comparisons between DSMC and continuum compressible boundary layer theory, for two-dimensional flow, are shown in order to illustrate the need for a kinetic computational method. The validation demonstrates the merit of selecting the DSMC method based on the global Knudsen number, first mentioned in Section 5.5.1 as 0.004, which is in the transitional rarefied regime. Comparisons between the computational methods involve the boundary layer velocity and temperature profiles and the following surface properties: skin friction and Stanton number. As discussed in Chapter 1, there are various continuum approaches that can be used to estimate these flow conditions; however, it is beneficial to begin with a simple approach. Here estimations are made using continuum boundary layer theory for two-dimensional compressible flow. Because

of time constraints, the comparisons are limited to the compressible boundary layer theory. This boundary layer theory is expected to yield different results. The degree of these differences is determined in this section.

The two-dimensional compressible boundary layer theory is founded on a set of boundary layer assumptions for compressible flow. These assumptions reduce the Navier-Stokes equations to a simplified set of partial differential equations called the compressible boundary layer equations. These equations are amenable to further reduction, through a mathematical transformation, to a set of ordinary differential equations; thus enabling more efficient numerical solution. The transformation reduces the two-dimensional problem, in terms of spatial coordinates x and y, into a one-dimensional problem, in terms of a similarity variable y_s. The independent variables, x and y, of the compressible boundary layer equations are transformed into similarity variables, x_s and y_s, via the Dorodnitsyn et al. transformation [*Anderson* (1989)]:

$$x_s = \int_0^x \rho_e u_e \mu_e dx \tag{5.9}$$

$$y_s = \frac{u_e}{\sqrt{2x_s}} \int_0^y \rho dy \tag{5.10}$$

where the subscript e indicates that the quantity is associated with the edge of the boundary layer. In addition, the dependent variables, x velocity V_x and total enthalpy h, are converted into the similarity functions, $f = f(x_s, y_s)$ and $g = g(x_s, y_s)$, via the following defining equations:

$$\frac{\partial f}{\partial y_s} = \frac{u}{u_e} \tag{5.11}$$

$$g(x_s, y_s) = \frac{h}{h_e} \tag{5.12}$$

For a flat plate, the form of the momentum and energy boundary layer equations further reduce such that the similarity functions become functions of only one variable: $f(y_s)$ and $g(y_s)$. The compressible boundary layer equations for a flat plate are then a set of ordinary differential equations as follows:

$$\frac{d}{dy_s}\left(CR\frac{d^2f}{dy_s^2}\right)+f\frac{d^2f}{dy_s^2}=0 \tag{5.13}$$

$$\frac{d}{dy_s}\left(\frac{CR}{Pr}\frac{dg}{dy_s}\right)+f\frac{dg}{dy_s}+\frac{u_e^2}{h_{o_e}}\frac{d}{dy_s}\left[CR\left(1-\frac{1}{Pr}\right)\frac{df}{dy_s}\frac{d^2f}{dy_s^2}\right]=0 \tag{5.14}$$

where Pr and CR are the Prandtl number and the Chapman-Rubesin parameter, respectively. They are defined by the following equations:

$$Pr=\frac{\mu c_p}{k} \tag{5.15}$$

$$CR=\frac{\rho\mu}{\rho_e\mu_e} \tag{5.16}$$

To arrive at Eqns. (5.13) and (5.14), the edge properties u_e, T_e and p_e and the wall temperature T_w are assumed constant, and the diffusion term in the energy equation is neglected. For further details of the derivation and method of solution refer to *Anderson* (1989) and *White* (1991). In this section, the similarity solutions are converted back to physical variables in order to allow comparison with the DSMC solutions.

Comparisons between the boundary layer theory and DSMC for the boundary layer velocity and temperature profiles are illustrated by Figs. 5.3 (a) and (b), respectively. The DSMC results with full gas-surface accommodation are chosen because the continuum theory assumes full accommodation. As expected it is seen that the boundary layer profiles disagree substantially. The continuum theory results in a substantially larger

boundary layer size. In addition, the continuum theory has no slip or temperature jump at the surface. These conditions delay boundary layer growth, and thus, are a cause of the smaller boundary layer size given by DSMC. The profile shapes are also distinct. For the velocity profiles, compressible continuum theory yields a linear shape, whereas DSMC gives a nonlinear shape. The smaller boundary layer size determined by DSMC also
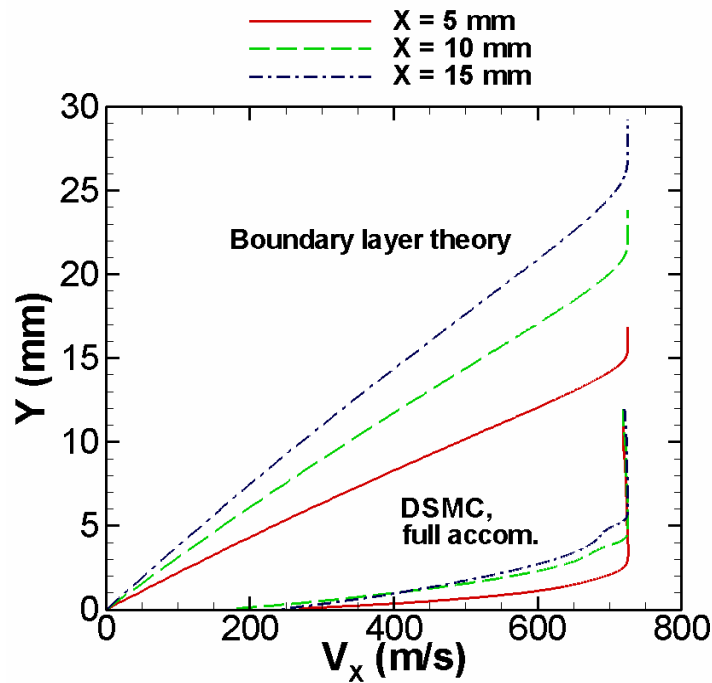
(a) *x velocity*

Figure 5.3   Comparison of windtunnel flat plate boundary layer profiles at three locations downstream from the leading edge. Profiles computed from continuum compressible boundary layer theory and DSMC.
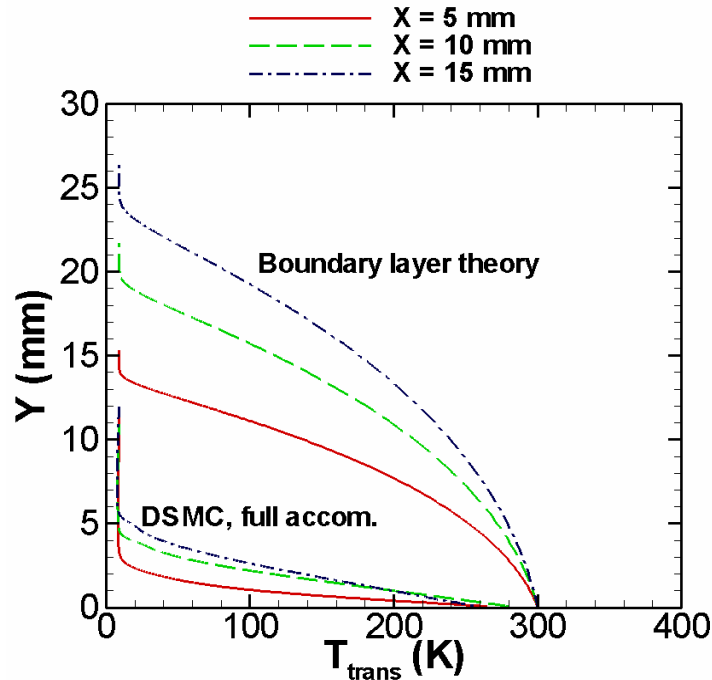
(b) *Translational Temperature*

Figure 5.3   Concluded.

indicates that DSMC involves a lower viscosity than in the continuum theory. For the temperature profiles, both approaches result in nonlinear shapes; however, the compressible boundary layer theory again results in a substantially larger boundary layer. The larger thermal boundary layer is indicative of a larger thermal conductivity. Clearly, it is necessary to account for rarefied effects in this analysis, where the global Knudsen number is in the rarefied transitional regime at 0.004.

Comparisons between the boundary layer theory and DSMC for surface properties of skin friction coefficient and Stanton number are illustrated in Figs. 5.4 (a) and (b). As expected, there are substantial differences between the two computational approaches. For the skin friction, however, similar trends are observed beyond 2 mm from the leading edge.   For the Stanton number, there is little similarity between the continuum boundary

110
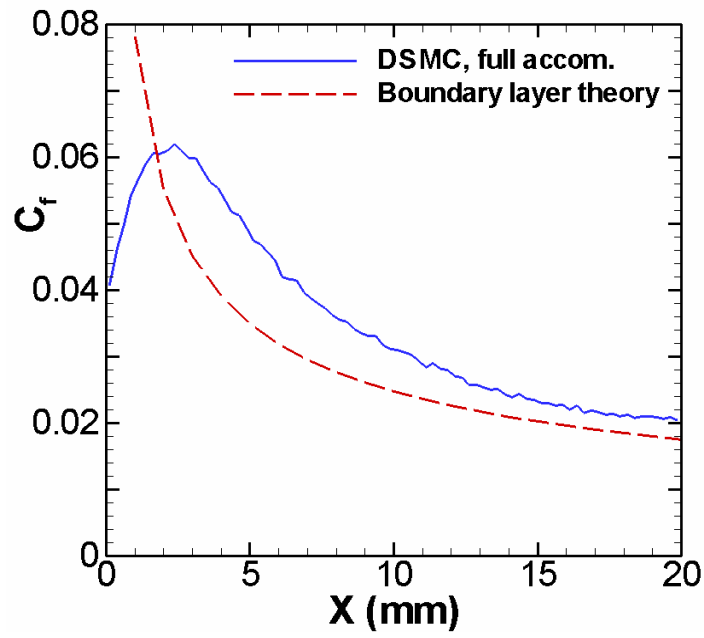
(a) *Skin friction coefficient*
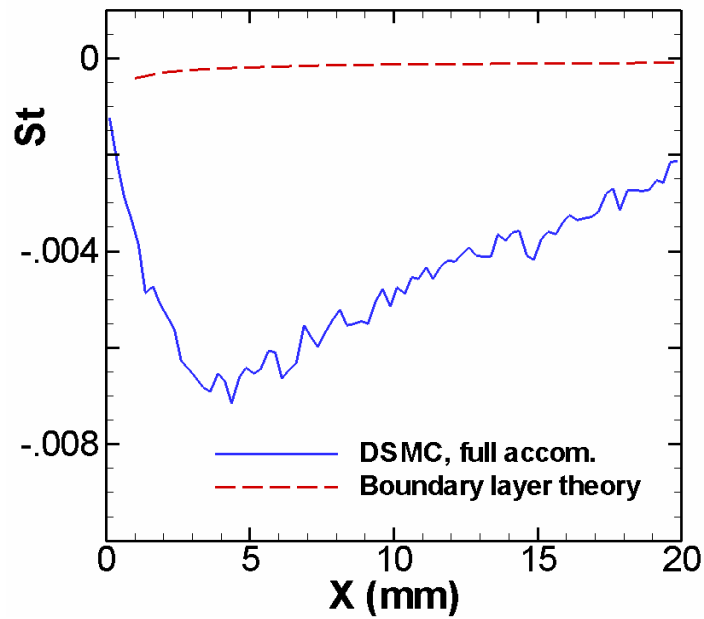
(b) *Stanton Number*

Figure 5.4   Comparison of windtunnel flat plate surface properties between continuum compressible boundary layer theory and DSMC

layer theory and the DSMC method. This again shows the need to account for rarefied effects in these transitional rarefied conditions.

5.5.3 Contour plots

The variation of Maxwell's fraction a_M from fully specular to fully diffuse results in a variation in boundary layer size from non-existent to maximum extent. Part of this variation is illustrated by the half and fully diffuse cases in Figs. 5.5 (a) and (b). These figures also illustrate the nonuniform inflow boundary through streamlines of bulk flow velocity. A similar variation in boundary layer size is given by the parametric analysis with the CLL model involving the variation in tangential momentum accommodation σ_t, with full normal kinetic energy accommodation $\alpha_n = 1$, except that the boundary layer does not completely disappear at $\sigma_t = 0$.

(a) $a_M = 0.5$ (b) $a_M = 1.0$
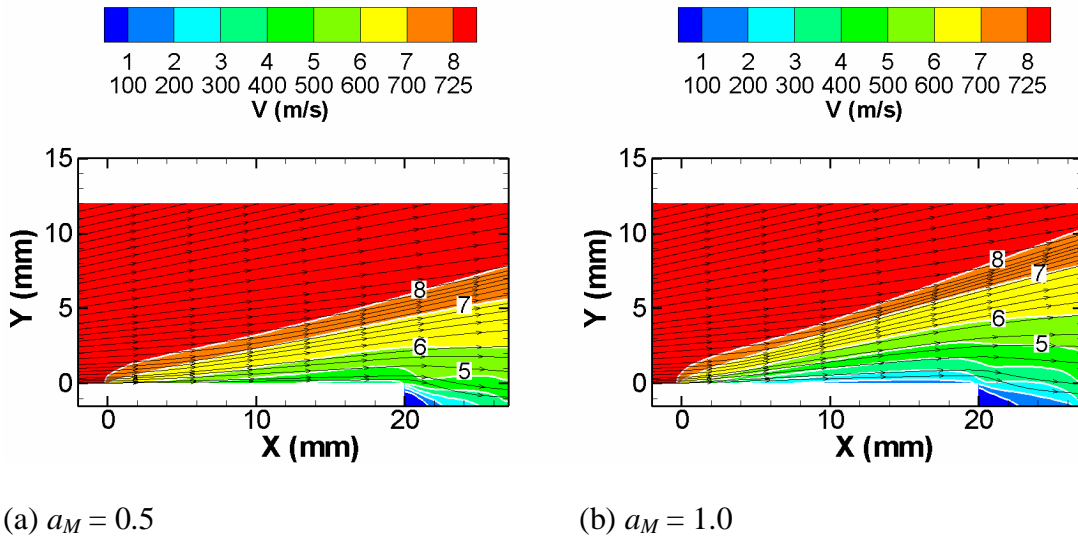
Figure 5.5   Contour plots and streamlines of flow speed at two values of Maxwell's fraction

5.5.4 Effects of gas-surface accommodation on molecular probability distributions

Molecular distribution plots provide a detailed perspective of the effects of the different gas-surface interaction models and of varying the gas-surface accommodation. Molecular velocity distributions at two locations over the flat plate surface are examined. The molecular velocity distributions at $x = 0$ mm are unaffected by changes in gas-surface interaction model or gas-surface accommodation. These distributions are shown in Fig. 5.6 (a). These distributions correspond to the first computational cell over the flat plate surface, which begins at $x = 0$ mm and ends at $x = 0.25$ mm; this cell and all other cells next to the surface are about 0.1 mm high. They are unaffected by changes in accommodation because the associated computational cell is within the first mean-free-path over the flat plate. Molecular velocity distributions at $x = 5.0$ mm are shown below
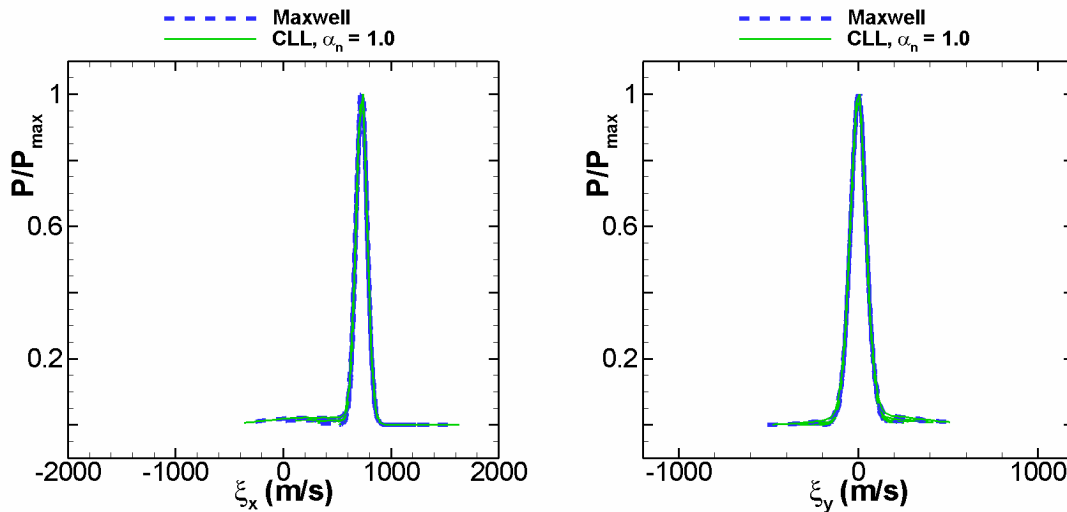
(a) Distributions of computational cell containing point $(x, y) = (0.0, 0.0)$ mm

Figure 5.6   2D DSMC molecular velocity probability distributions of two gas-surface interaction models at various levels of gas-surface accommodation: $a_M, \sigma_t = 0, 0.25, 0.5, 0.75$ and 1.0
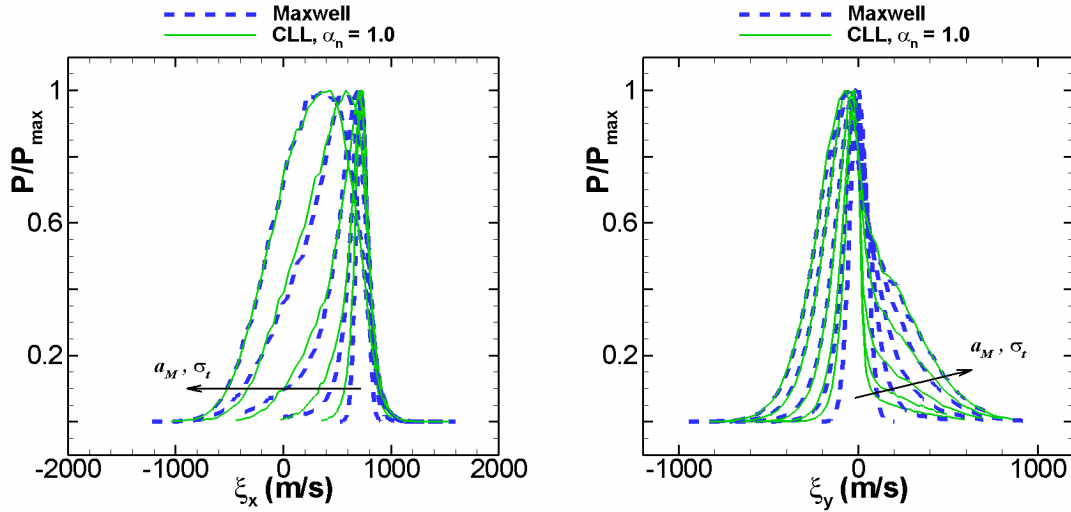
(b) Distributions of computational cell containing point $(x, y) = (5.0, 0.0)$ mm

Figure 5.6   Concluded.

in Fig. 5.6 (b). This figure illustrates that the degree of translational nonequilibrium next to the surface is proportional to the level of gas surface accommodation. It also shows that the Maxwell and CLL models give identical results only for full gas-surface accommodation, $a_M = \sigma_t = 1.0$. At partial levels of gas-surface accommodation, the models yield similar ξ_x distributions. However, the ξ_y distributions, at $\xi_y > 0$, are significantly different.

The molecular surface scattering plots are also examined at the two positions $x = 0$ and 5.0 mm over the flat plate surface. These are probability distribution plots of reflected molecule scattering angle θ_r. Figures 5.7 (a) through (d) present the distributions. The scattering plots show the essential differences between the Maxwell and CLL gas-surface interaction models. The Maxwell scattering distributions have unrealistic peaks due to the specular angle at partial levels of accommodation; the associated diffuse component of the scattering distribution is evident by the circular segments. The CLL scattering

(a) *x* = 0 mm

(b) *x* = 5.0 mm
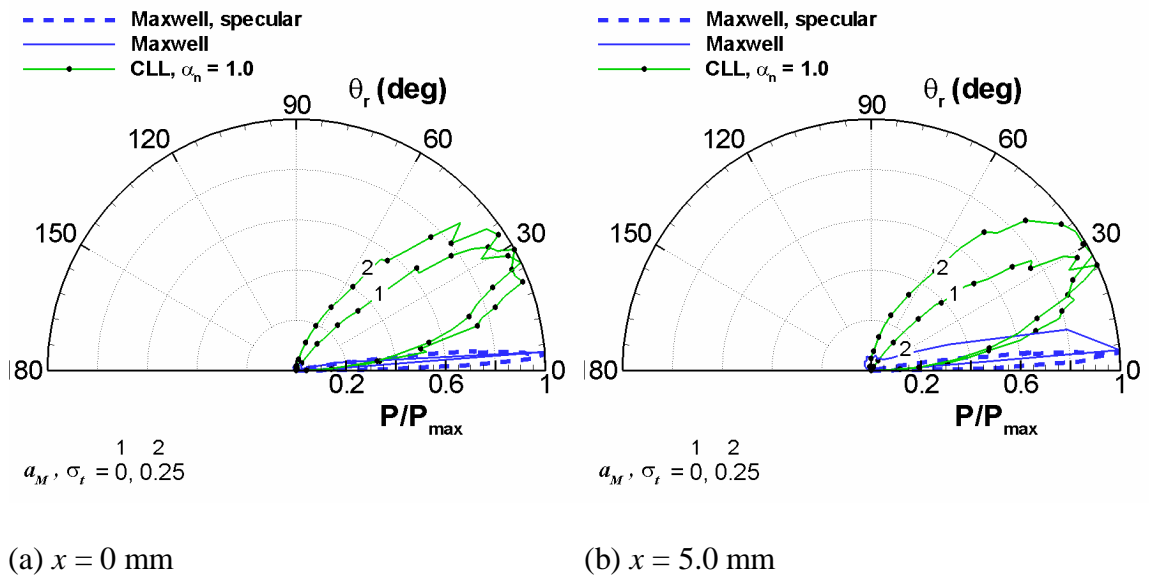
0 and 25% accommodation

(c) *x* = 0 mm

(d) *x* = 5.0 mm
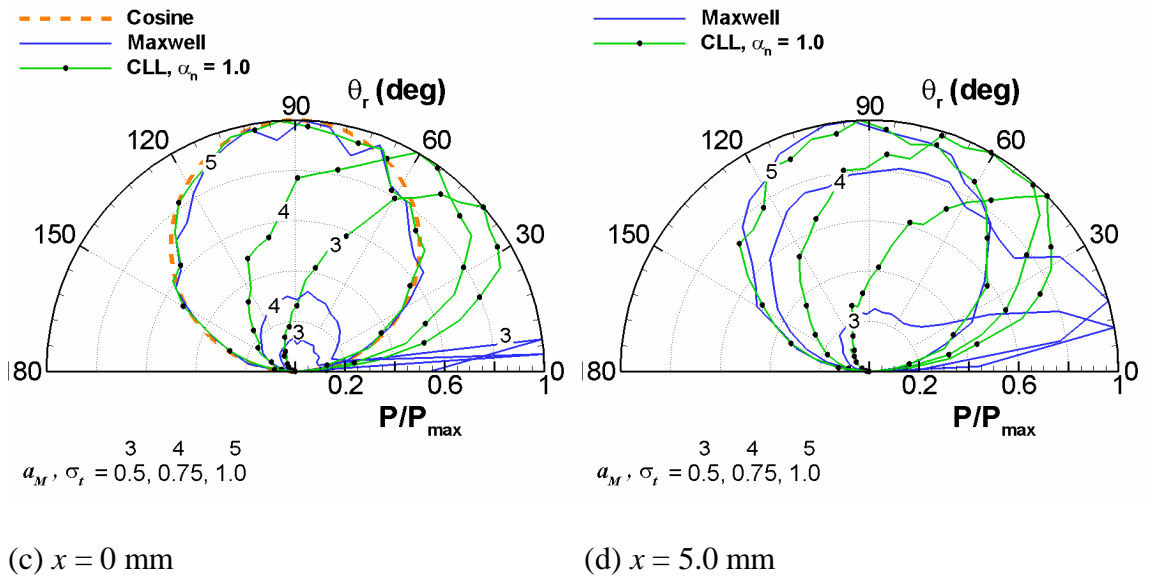
50, 75 and 100% accommodation

Figure 5.7   2D DSMC probability distributions of reflected molecular velocity angle of two flat plate surface faces, *y* = 0 mm, of two gas-surface interaction models at various levels of gas-surface accommodation

distributions are petal-shaped, similar to observations of reflected rarefied molecular beams from clean flat surfaces [*Schaaf* (1963); *Hinchen* (1966)]. As required, the scatter plots further confirm that both models are equivalent at full accommodation. There, they yield the Lambert or cosine distribution of optics theory, which also applies to the random distribution of gas-surface scattering angles. These plots also show variations in scattering due to variations in accommodation and position x along the flat plate surface. The Maxwell distributions have abrupt changes with increasing accommodation and position; in contrast, the CLL distributions vary smoothly with accommodation and position. Using the CLL model the changes due to position are remarkably more subtle.

5.5.5 Effects of gas-surface accommodation on boundary layer velocity profiles

For each of the simulations, data are extracted along vertical slices corresponding to the locations where PLIF measurements were taken, $x = 0, 2.5, 5, 7.5, 10, 12.5, 15, 17.5$ and 20 mm from the leading edge. These data include x and y velocity components. Figures 5.8 (a) through (e) present some of the comparisons between the MONACO parametric results and the PLIF data. Various observations are made about the results.

Figure 5.8 (a) compares the DSMC and measured velocity profiles at the leading edge of the flat plate. The fact that the simulations match the experimental data here indicates that the correct inflow conditions are employed. Furthermore, Figs. 5.8 (a) through (e) indicate that the data agree in the freestream region above the boundary layer.

The boundary layer is where the flow-field is affected by different gas-surface interaction models and different levels of gas-surface accommodation. When full gas-surface accommodation conditions are specified, by setting all accommodation

116

coefficients equal to one, the Maxwell and CLL models provide the same boundary layer profiles, as expected from the definition of the models. In addition, the Maxwell and CLL models yield essentially the same results for $a_M = \sigma_t = 0.5$ and 0.75. However, the
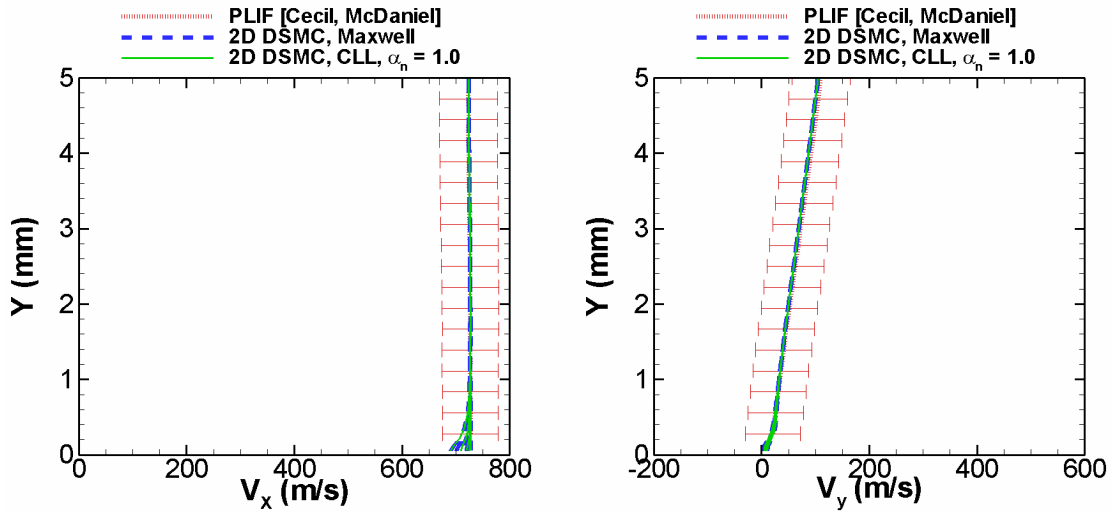
(a) *Boundary layer profiles at x = 0 mm*
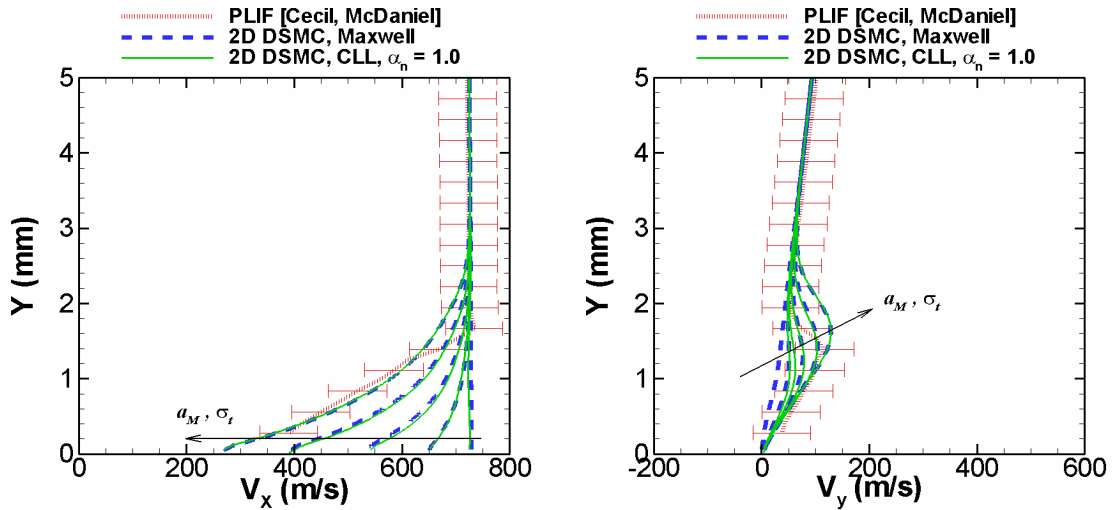
(b) *Boundary layer profiles at x = 5 mm*

Figure 5.8   Comparison of boundary layer velocity profiles between flat plate windtunnel tests and DSMC simulations with different gas-surface interaction models at various levels of accommodation

117

the Maxwell and CLL models differ significantly at $a_M = \sigma_t = 0$ and 0.25. Hence, the Maxwell and CLL models are equivalent when $a_M = \sigma_t \geq 0.5$ for these flow conditions, while $a_{E\_int} = \alpha_n = 1.00$ in the CLL model.

The simulations involving full gas-surface accommodation, $a_M = \sigma_t = 1.0$, give the
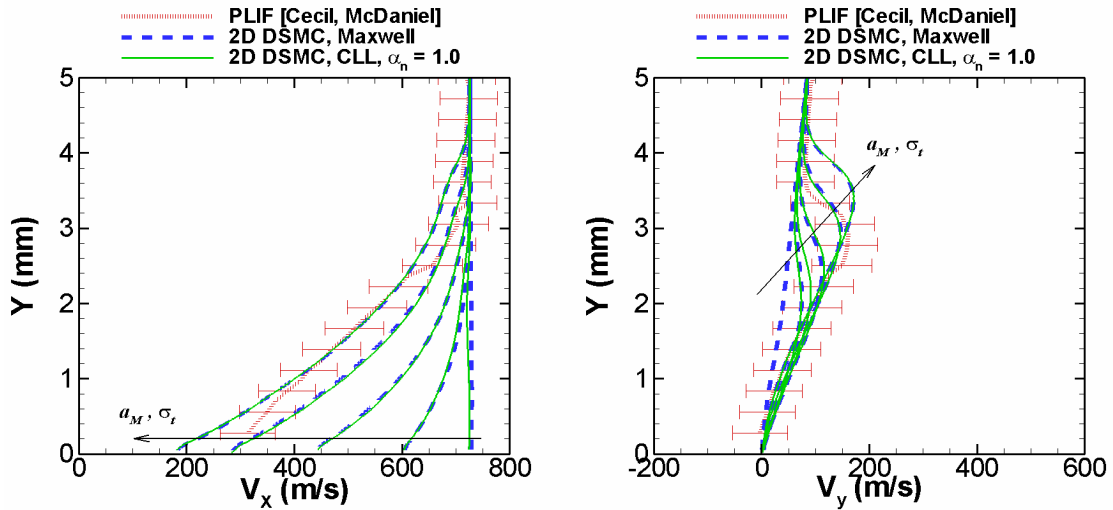
(c) *Boundary layer profiles at x = 10 mm*
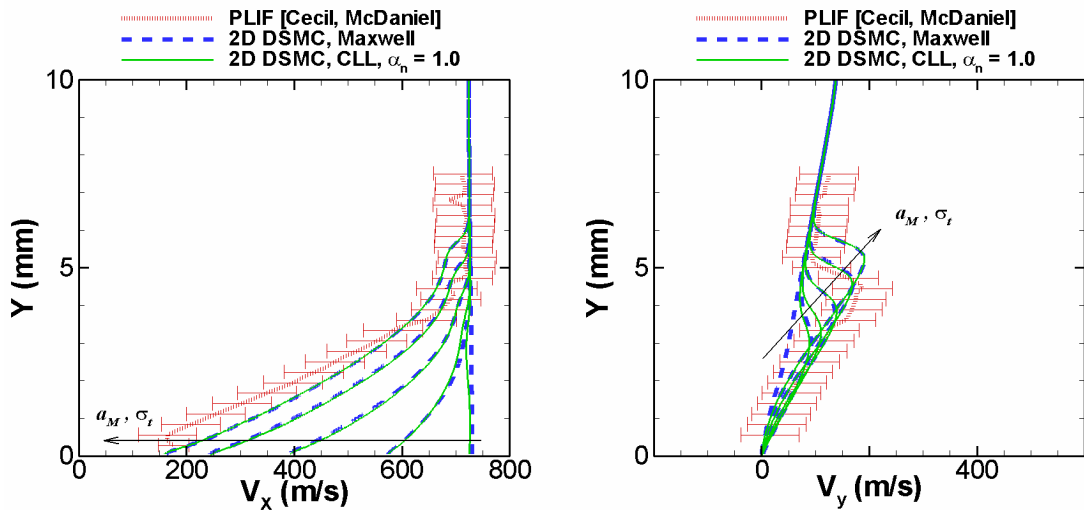
(d) *Boundary layer profiles at x = 15 mm*

Figure 5.8   Continued
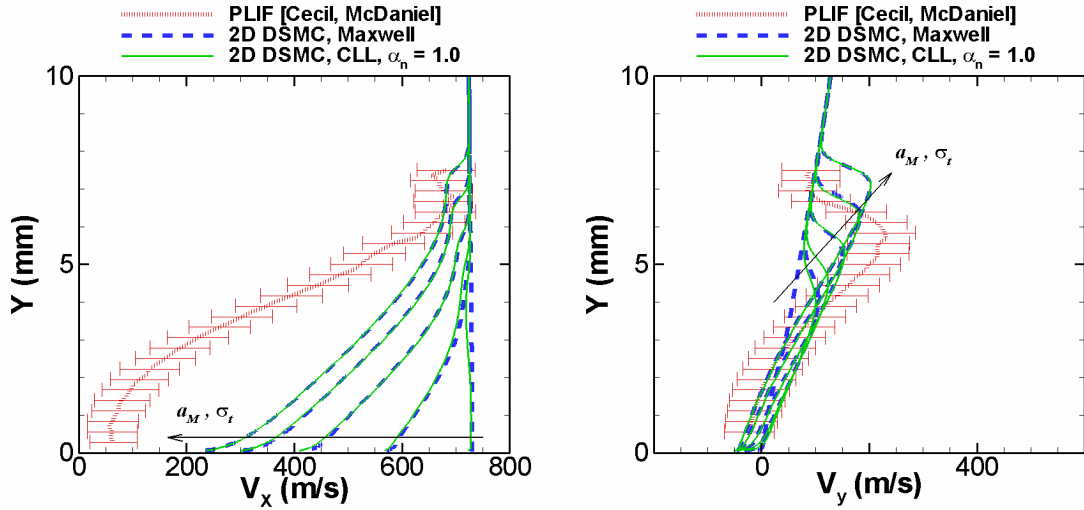
(e) *Boundary layer profiles at x = 20 mm*

Figure 5.8   Concluded

overall best agreement with the measured data for the V_x profiles, except at the transition

from the boundary layer to the freestream, which is affected by the diffuse shock. The V_x

DSMC results, even for the diffuse case, disagree with the measured data at $x \geq 15$ mm.

This is due to an adverse pressure gradient believed to be caused by windtunnel test flow

phenomena, beyond the specified computational domain, and thus, not captured by the

simulation. The simulations with $a_M = \sigma_t = 0.75$ provide the overall best agreement with

the measured data for the V_y profiles, and the V_x profiles in the transition from the

boundar layer to the freestream. Hence, the level of accommodation that provides the

overall best agreement among both the V_x and V_y profiles is a compromise between 0.75

and 1.0. Simulations with the average accommodation, $a_M = \sigma_t = 0.875$, result in profiles

lying in the middle, in accord with the linear variation of the profiles with

accommodation, when the accommodation level is greater than 0.5. Hence, the overall

best agreement, among the considered accommodation levels of the a_M or σ_t sensitivity studies, occurs when $a_M = \sigma_t = 0.875$.

The large prediction of accommodation is a reasonable prediction from two perspectives. From physical reasoning, it makes sense that gas-surface accommodation is incomplete at rarefied hypersonic conditions because of the relatively short average residence times of the gas-molecules with the flat surface. Conversely, full gas-surface accommodation occurs for conditions with continuum densities and low velocities. The degree of accommodation decreases with increase in incident velocity and decrease in gas density; and also smaller surface roughness. The accommodation of this flow condition is expected to be relatively high because of the relatively high gas density, similar to density of air at 60 km altitude according to US 1976 standard atmosphere [*Lide* (2007)]. The large prediction of accommodation is also reasonable from laboratory or flight measurements. Measurements from satellites, which are exposed to gases with higher velocities and much lower densities, show the gas-surface accommodation to be near full [*Minton et al.* (2004); *Moe* (2005) and *Moe et al.* (1998)]; in particular, *Moe* (2005) reports that satellites measure energy accommodation that is near unity at about 155 km perigee altitude. Furthermore, *Cook et al.* (1996) measured large levels of momentum accommodation in experiments involving rarefied molecular beams of nitrogen and hydrogen with incident velocities of over 1000 m/s, and small incidence angles ($< 45°$) with finer surfaces or at any incidence angle with rougher surfaces.

The sensitivity study of normal kinetic energy accommodation coefficient α_n, confirms that V_x, the tangential component of velocity, is not significantly affected. The variation of α_n does affect V_y, the normal component of velocity, but to an order of

magnitude smaller extent than the same variation of σ_t. This study indicates that it is possible to improve the agreement in V_y, between the CLL simulation with $\sigma_t = 1.0$ and the measured data, by significantly reducing α_n; however, there is no indication in the experiments found in literature, or even in physical reasoning, that low normal kinetic energy accommodation would occur along with full tangential momentum accommodation σ_t. In 1994, *Gombosi* states that the normal accommodation is relatively unknown and usually assumed equal to unity. Hence, this case can not be favored over the $\sigma_t = 0.875$ case.

5.5.6 Seeded iodine simulations

The simulations involving pure nitrogen provide good agreement with the PLIF windtunnel test data using a proper specification of gas-surface accommodation, within the boundary layer region not affected by the adverse pressure gradient. However, because the PLIF data reflects the velocity of the seeded iodine, it is possible that the PLIF data itself is unrepresentative of the nitrogen flow in the windtunnel test. Because the accuracy of the gas-surface accommodation prediction is sensitive to the accuracy of the measured data, simulations are run to examine whether the seeded iodine accurately represents the nitrogen flow velocity. The iodine input parameters for these simulations are listed in Table 5.4. The values of T^*, $Z_{rot,\infty}$, $\delta_{diameter}$ and ω_{22}, for iodine, are taken from a report by *Boyd et al.* (1994). The subscripts 1 and 2 on the VHS collision model viscosity index ω_{ij} represent N_2 and I_2, respectively. ω_{ij} represents the viscosity index for collisions between species i and j.

Table 5.4   **Iodine input parameters for seeded iodine DSMC simulation**
                  of flat plate windtunnel test

Species Data		Collision Cross-Section Data	
Species	I_2	$\delta_{diameter}$	8.80×10^{-10} m
MW	253.81	ω_{22}	0.945
ζ_{rot}	2.0	ω_{12}	0.8
ζ_{vib}	1.8		
θ_{vib}	306.9 K		
T^*	557.0 K	Solid Surface Data	
$Z_{rot,\infty}$	75	T_w	300 K

The inflow properties for nitrogen are the same as in Figs. 5.2 (a) and (b). The inflow profiles for iodine are also the same, except for the number density. The inflow number density for iodine is determined by multiplying the nitrogen number density by the mixing ratio of iodine to nitrogen. The windtunnel tests held this value at roughly 3.5×10^{-4} [*Cecil and McDaniel* (2007)]. Because of the small mixing ratio of iodine to nitrogen, a species weighting factor is assigned to the iodine, $W_{p,iodine} = 3.5 \times 10^{-4}$, in order to reduce statistical scatter of the iodine results. It is given a value equal to the mixing ratio so that the number of simulated iodine molecules is equal to the number of simulated nitrogen molecules passing through the computational domain. The MONACO procedure enabling trace species weighting factors is credited to *Burt* (2006).

With these flow conditions, a simulation is made with full gas-surface accommodation. For simplicity, the Maxwell gas-surface interaction model is used with $a_M = 1.00$. This simulation requires the computational parameters summarized in Table 5.5. They are vastly more expensive than the pure nitrogen simulations; the added expense comes from the necessity of smaller cell sizes due to the smaller mean-free-path of the iodine. In fact, to keep the simulation manageable the simulation domain is reduced by roughly 75%, as illustrated by Fig. 2.1 in Chapter 2.

Table 5.5 **Computational properties of N_2 and seeded I_2 simulation of the flat plate windtunnel test**

W_p	2.0×10^{10}	Time-step size	5.0×10^{-9} s
Particles	~62,800,000	Time-steps	150,000
Cells	514,809	Wall Time	~35 hr
Processors[*]	30		

Figures 5.9 (a) and (b) illustrate the computational domain and contour plots of mean-free-path for each species. The origin of the *xy* coordinate system is at the leading edge of the flat plate. The iodine mean-free-path is roughly an order of magnitude smaller throughout the computational domain. This is a consequence of the dependency on molecular weight and collision cross-section of the variable hard sphere mean-free-path in a gas mixture [*Bird* (1994)]. Even though the mixture mean-free-path is essentially unchanged with the introduction of seeded iodine, the mean-free-path of the iodine itself, which is about an order of magnitude smaller than the nitrogen mean-free-path, reduces the required computational cell sizes in order to correctly simulate the iodine progression through the flow field.
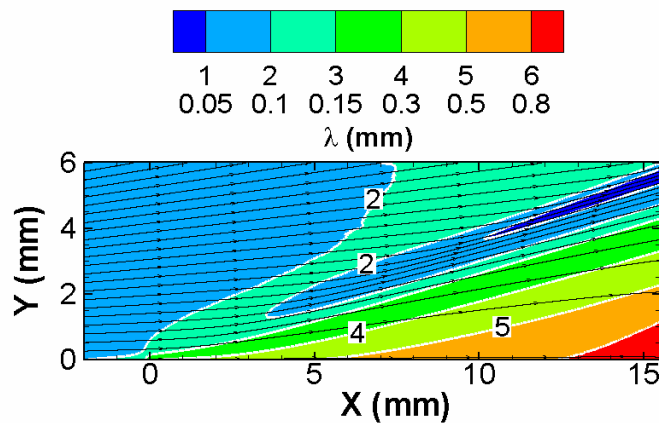
(a) *Nitrogen*

Figure 5.9 **Contour plots of mean-free-path, with flow speed streamlines, for nitrogen and iodine at full gas-surface accommodation**
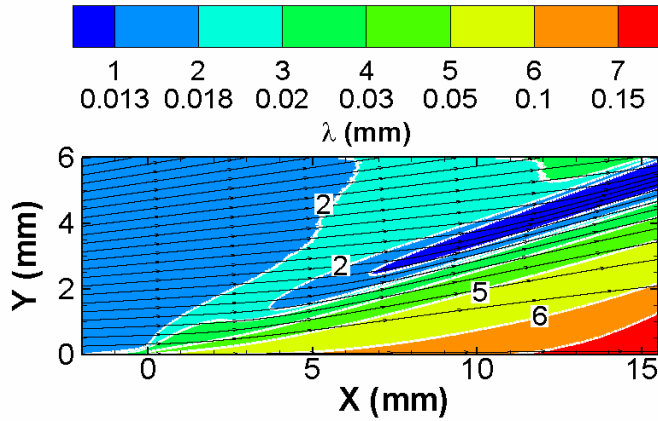
(b) *Iodine*

Figure 5.9. Concluded.

Figures 5.10 (a) and (b) illustrate the flow characteristics with contours and streamlines of flow speed for each species. They indicate that the iodine velocity field is very similar to the nitrogen velocity field. They also show that these velocity fields are similar to the pure nitrogen velocity field with full gas-surface accommodation presented in Fig. 5.5 (b) near the leading edge. This is expected from the small ($\sim10^{-4}$) mixture ratio
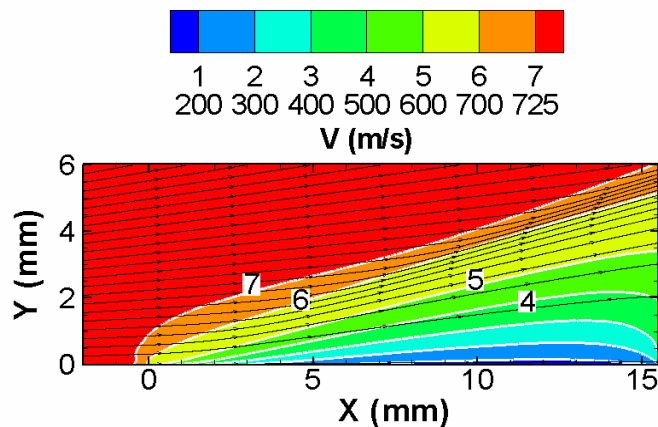
(a) *Nitrogen*

Figure 5.10 Contour plots and streamlines of flow speed for nitrogen and iodine at full gas-surface accommodation
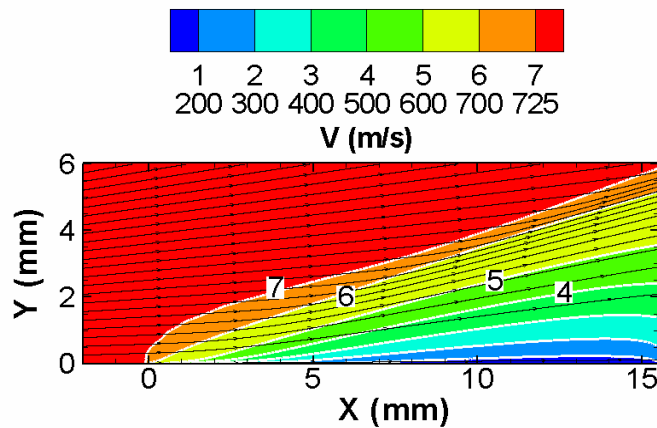
(b) *Iodine*

Figure 5.10 Concluded.

of iodine to nitrogen and corroborates the windtunnel PLIF measurement procedure. The figures also expose the effect of the outflow boundary on the flow field. Beyond $x \approx 12.5$ mm, the contours are affected by presence of the simulation outflow boundary and the results there do not represent the windtunnel test.

Figures 5.11 (a) through (f) compare boundary layer velocity profiles among pure nitrogen simulations, nitrogen with seeded iodine simulations, and windtunnel test measurements. The simulation and windtunnel test data agree within the freestream as required for a correct simulation. The profiles match at $x = 0$ mm, except very near the surface where the simulation profiles exhibit the beginning of the boundary layer and the iodine component indicates a larger slip velocity due to the larger molecular weight of the iodine. At $x = 0$ mm, the pure and component nitrogen profiles are identical. This again is due to the small mixture ratio of iodine to nitrogen.

At $x > 0$, several observations about the comparisons are made. The component nitrogen profiles are almost identical to the pure nitrogen profiles. There are slight

differences near the "knee" of the V_y profiles, where the diffuse oblique shockwave lies. These differences occur for $x > 2.5$ mm or within 28 and 150 nitrogen and iodine respective local mean free path distances from the leading edge and are due to the presence of iodine in the mixture simulations.
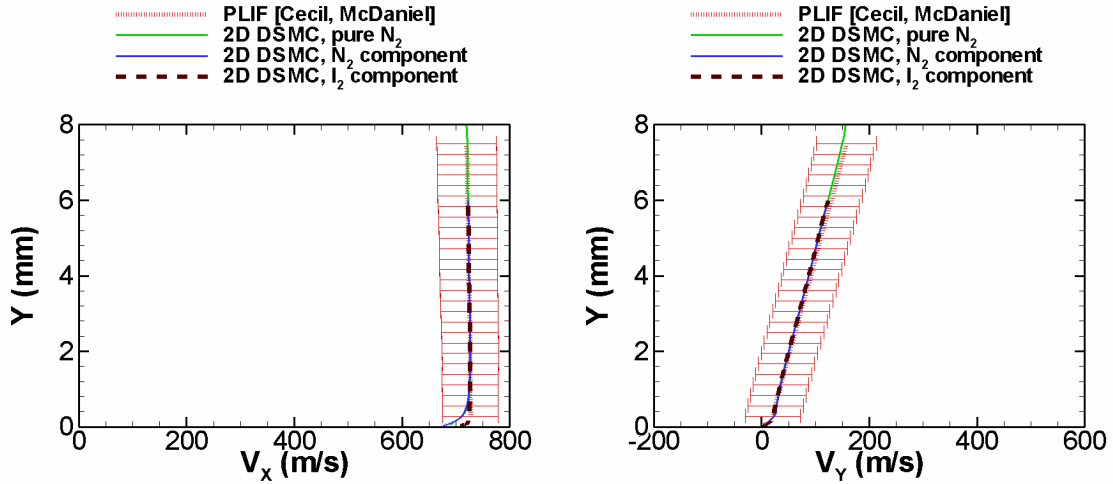
(a) *Boundary layer profiles at x = 0* mm
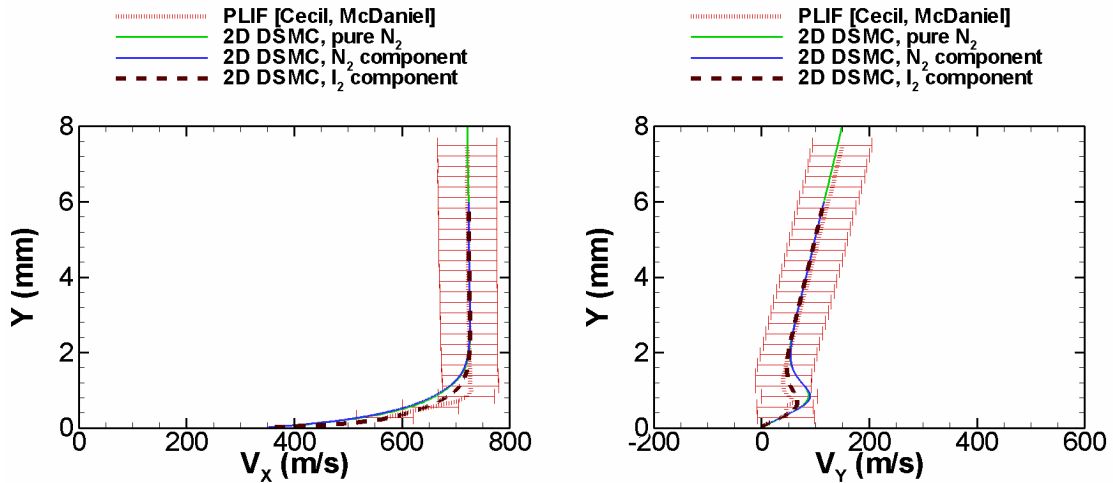
(b) *Boundary layer profiles at x = 2.5* mm

Figure 5.11 Comparison of boundary layer velocity profiles among pure nitrogen and nitrogen-seeded iodine MONACO simulations, with full gas-surface accommodation, and PLIF windtunnel test data

The shock is observed near the edge of the boundary layer and is more pronounce in the V_y profiles than in the V_x profiles. This is expected by the acute angle of the oblique shock. The V_y plots illustrate that in the boundary layer V_y is accelerated to a value greater than V_y in the freestream and that the oblique shock bridges these velocities.

(c) *Boundary layer profiles at x = 5.0 mm*

(d) *Boundary layer profiles at x = 7.5 mm*
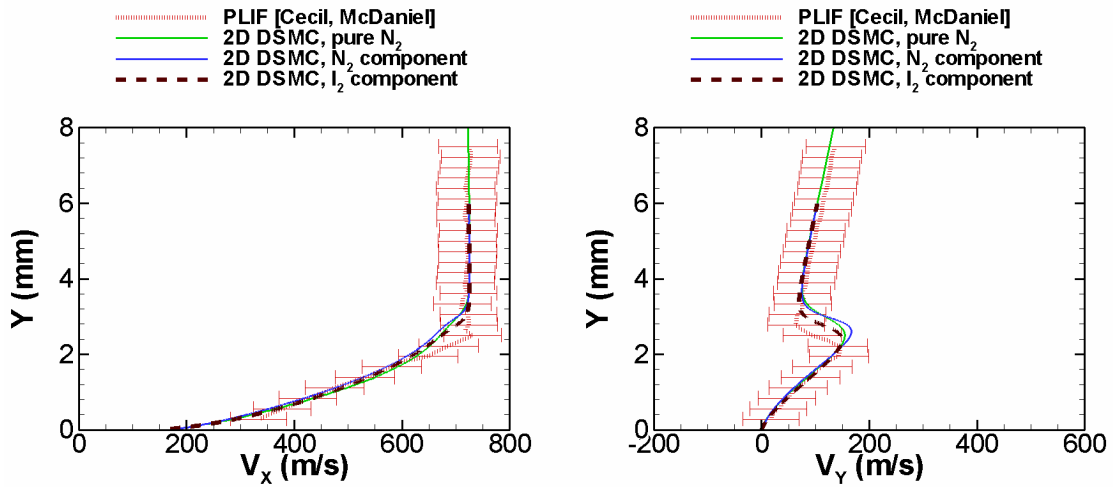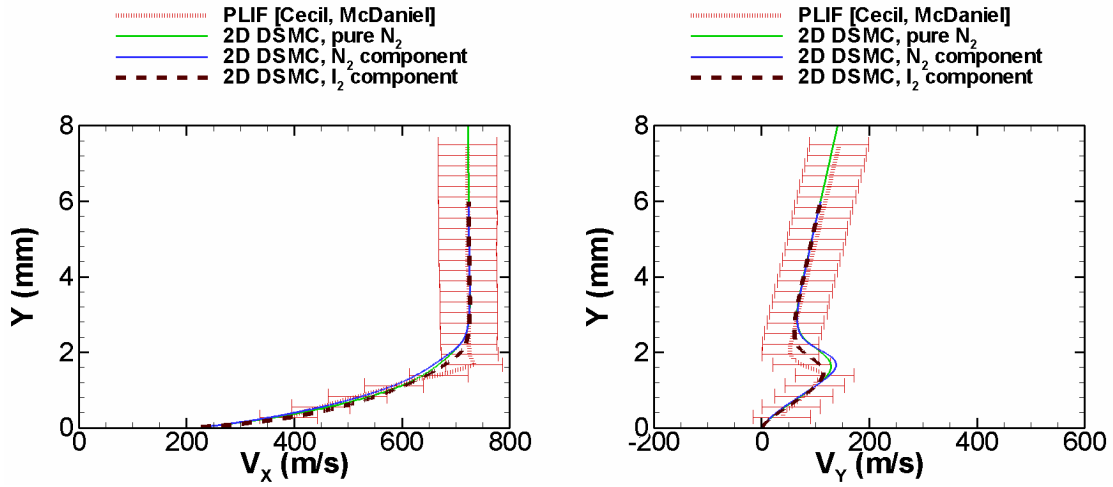
Figure 5.11 Continued

For the V_x profiles, largest differences between the nitrogen and the iodine profiles occur at x= 2.5 mm, however, the profiles converge near the surface and display the same slip velocity. The differences are mainly due to the larger inertia of iodine causing it to maintain a slightly larger x velocity component as it blows over the flat plate. Beyond x =

(e) *Boundary layer profiles at x = 10 mm*

(f) *Boundary layer profiles at x = 12.5 mm*
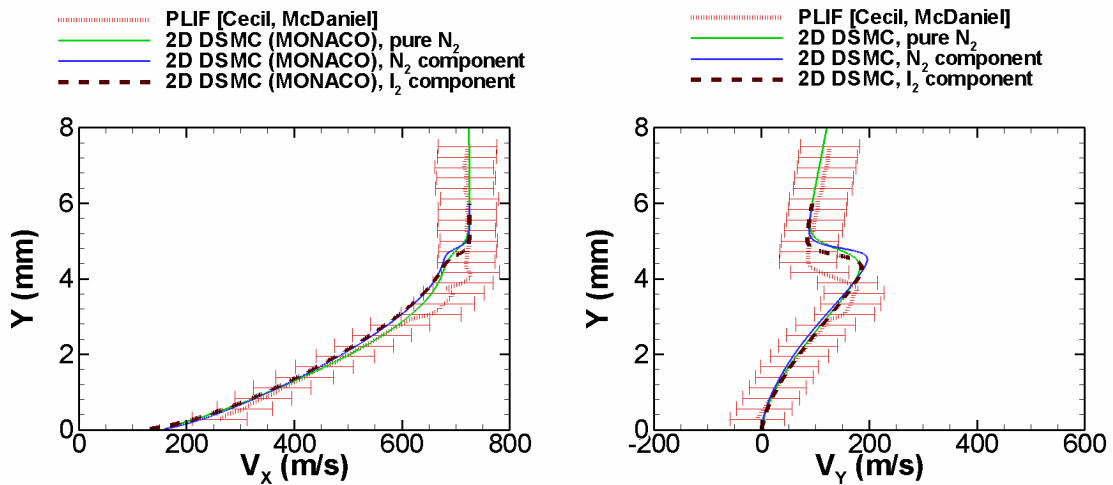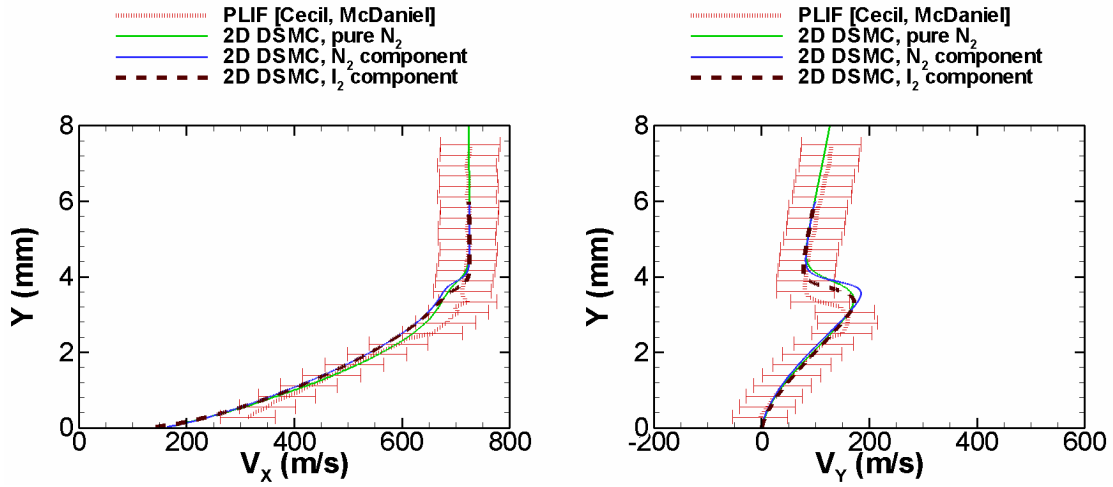
Figure 5.11 Concluded

2.5 mm, the differences between the nitrogen and iodine V_x profiles are insignificant.

Differences between the nitrogen and iodine V_y profiles occur only at the "knee" caused by the diffuse oblique shockwave. These differences are greatest at $x = 2.5$ mm, more significant than in the V_x profiles, and again decrease beyond $x = 2.5$ mm. These differences are again mainly due to the larger inertia of the iodine, in this case, slowing its ascent caused by the boundary layer expansion underneath the diffuse oblique shockwave. The differences between the nitrogen and iodine V_y profiles account for some of the differences between pure nitrogen simulation and the windtunnel data in these profiles. However, at $x \geq 10$ mm, the effect of iodine is no longer sufficient to translate the entire "knee" within the windtunnel data uncertainty envelope.

In summary, the seeded iodine simulations indicate that the iodine merely slightly affects the V_x profiles within the boundary layer at $x \leq 2.5$ mm because of the small ($\sim 10^{-4}$) mixture ratio of iodine to nitrogen; this corroborates the PLIF measurements of the nitrogen flow. For the V_y profiles, the seeded iodine profiles are distinct where the diffuse shock resides and account for some of the differences between the pure nitrogen simulation and windtunnel test data. The distinction is mainly due to the larger molecular weight of the iodine. In the relatively small segments where there are differences, the iodine profiles generally provide closest agreement with the windtunnel data, as expected. The inertia effects decrease as x increases beyond 2.5 mm. The result of these effects is to increase the computed accommodation level which gives the overall best agreement between the DSMC and measured data, however, rounded to one decimal place, $a_M = \sigma_t \approx 0.9$ remains the optimized estimate for the gas-surface accommodation.

In conclusion, the seeded iodine simulation revealed the following: the larger molecular weight and collision cross section of iodine cause an order of magnitude increase in simulation expense over the pure nitrogen simulations; the larger seeded iodine inertia partly explains differences in the pure nitrogen simulations and windtunnel test measurements; and because the overall differences are slight, the seeded iodine simulation substantiates the pure nitrogen simulations and accredits the PLIF measurements.

5.5.7 Analysis of thermal nonequilibrium in the boundary layer

In the contour and boundary layer simulation plots, the flow velocity is the local mean molecular velocity. The PLIF boundary layer plots also involve the local mean molecular velocity which is an accurate representation of bulk velocity in translational equilibrium. A system of molecules in translational equilibrium has each of their velocity components distributed in a Gaussian distribution, that is, a normal distribution. This is a Maxwellian velocity distribution. For rarefied transitional flows, there may be regions with translational nonequilibrium. A system of molecules in translational nonequilibrium has at least one of their velocity components distributed in a non-normal distribution, e.g., a distribution with multiple peaks or with a skewed shape. Thus, the mean molecular velocity is not generally an adequate representation of the molecular velocity distribution in translational nonequilibrium. Thus, in translational nonequilibrium attention is given to the anisotropic translational temperature tensor components. The degree to which the velocity distribution is Maxwellian indicates the utility of employing the mean velocity to represent the bulk velocity of the local system of gas molecules. The extent of translational nonequilibrium is indicated by differences in component translational

temperatures or differences between the mean and most probable local molecular velocities. Knowledge of where the mean velocity is an inaccurate representation due to translational nonequilibrium enables a more accurate interpretation of the corresponding flow conditions. Hence, molecular velocity distribution statistics and distribution shape and translational temperature profiles are examined at specified points to gauge for translational nonequilibrium and to explicitly illustrate the relation among these metrics. In addition, rotational temperature profiles are examined to gauge for rotational nonequilibrium within the flow field. In the following analysis, full gas-surface accommodation is assumed because it yields the greatest amount of thermal translational nonequilibrium in that it statistically incurs the greatest changes in normal and tangential kinetic energy and in rotational energy. Since the Maxwell and CLL models are equivalent at full gas-surface accommodation, the results from the Maxwell model are arbitrarily chosen for the analysis that follows and are referred to as the full gas-surface accommodation results. The analysis begins with examining the spatial variation of thermal nonequilibrium in the x direction at selected y; and then, ends with examining the spatial variation of thermal nonequilibrium in the y direction at selected x.

Table 5.6 presents statistics of molecular velocity probability distributions at selected computational cells along the x direction and next to the flat plate at $y = 0$ mm. These cells have their centers at a height of $y = 0.06$ mm from the surface. The statistics have various trends associated with increasing x position. The number of samples lowers with x because of fewer simulation molecules associated with the lower density in the expanded flow. The variation of percentage difference between the mean and most

Table 5.6   **2D DSMC statistics of molecular velocity distributions at $y = 0$ mm for various values of x with full gas-surface accommodation**

x (mm)	No. of Samples	ξ_x S. D.[*]	Mean	M. P.[†]	%Diff[‡]	ξ_y S. D.	Mean	M. P.	%Diff
0	6,441,210	217.8	636.0	747.0	16.1	109.2	16.5	9.6	52.3
2.5	4,387,893	335.7	403.4	705.2	54.5	204.3	6.6	-35.5	290.9
5.0	3,299,356	333.2	251.2	394.0	44.3	234.6	3.4	-69.3	220.9
7.5	2,752,768	326.8	201.1	308.3	42.1	256.2	1.4	-109.0	205.0
20	1,255,890	299.3	217.1	258.7	17.5	273.3	-6.6	-147.5	182.9

[*]standard deviation   [†]most probable value   [‡]percentage difference between Mean and M. P.

probable values suddenly increases at $x = 2.5$ mm and subsequently lowers with x. This percentage difference indicates the degree of translational nonequilibrium, which in this case is due to the initial wave of rebounding molecules from the flat plate surface. At equilibrium, the percentage difference is zero by definition. The cause of the tendency towards equilibrium, after the initial disturbance of reflected molecules, is attributed to more evenly balanced forward and backward scatter from adjacent cell boundaries, at positions further into the interior of the surface, which is due to continued collisions caused by scattered molecules. The larger percentage difference and standard deviation of the ξ_y distributions is attributed to the more significant change in the normal component of momentum due to collision with the surface. The standard deviation, which is indicative of the distribution spread, does not necessarily vary directly with the percentage difference: whereas, direct variation is found for the ξ_x distributions, inverse variation is found for the ξ_y distributions, between $x = 2.5$ and 20 mm; that is, as x increases from 2.5 mm, the standard deviation in the ξ_y distribution increases, while the respective percentage difference between the mean and most probable value decreases.

Figures 5.12 (a) through (d) illustrate the normalized probability distributions, corresponding to Table 5.6. At the computational cell adjacent to the leading edge, $x = 0$ mm, both the ξ_x and ξ_y distributions are near normal. Here, they are not significantly

affected by surface reflected molecules because the cell length is approximately equal to the local mean-free-path. The degree of translational nonequilibrium described by the

(a) ξ_x distributions

(b) ξ_y distributions

x = 0, 2.5 and 5.0 mm

(c) ξ_x distributions
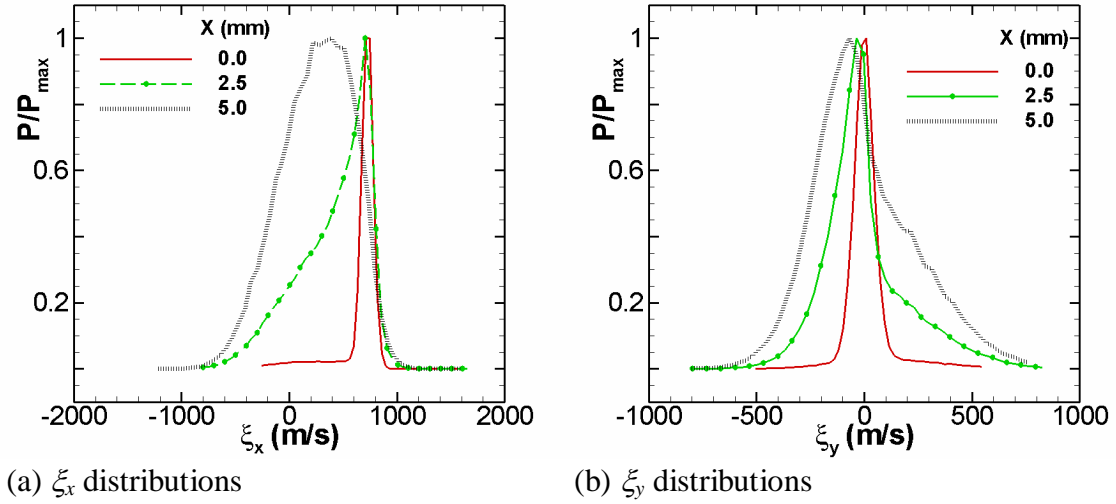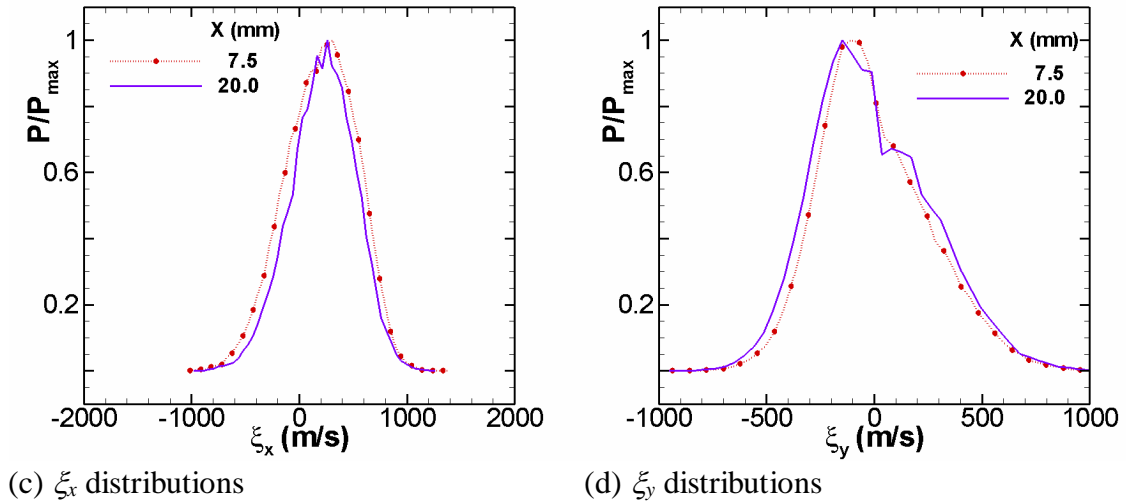
(d) ξ_y distributions

x = 7.5 and 20.0 mm

Figure 5.12 2D DSMC spatial variation of probability distributions of molecular velocity along x and next to surface, y = 0 mm, for full gas-surface accommodation

distribution shape agrees with the trend in percentage difference between the mean and the most probable values. The trend reflects the evolution of the balance between forward scatter from the surface to the left of the left boundary of a computational cell and backward scatter from the surface to the right of the right boundary of the cell. At $x = 2.5$ mm, the ξ_x distributions are significantly skewed. At $x = 5.0$ mm, the ξ_x distribution are only slightly skewed. By $x = 7.5$ mm, the ξ_x distributions have returned to a near normal shape. Molecules that traverse this distance will encounter an average of roughly 21 collisions, according to the computed local mean-free-path values. In contrast with the ξ_x distributions, the ξ_y distributions remain in translational nonequilibrium along the entire length of the flat plate beyond the leading edge. Observation of the ξ_y distributions in Figs. 5.12 (b) and (d) reveal that the influence of surface reflection slowly increases from an enlarged tail at $x = 2.5$ mm to a second peak at $x = 20$ mm. The two peaks at $x = 20$ mm are due to the incident number flux and the surface reflected number flux. The rise of the second peak is also due to the presence of a backward facing step at $x = 20$, associated with the end of the flat plate model and the beginning of the sting, shown in Fig. 5.5. The backward facing step causes the flow to abruptly expand. This deflects the bulk velocity streamlines slightly downward within a few mean-free-paths of the backward facing step; hence, causes incident flux distribution to shift further toward negative ξ_y and expose the peak of the reflected flux distribution. It is also possible that a recirculation vortex in the backward facing step causes small numbers of simulation molecules to backscatter into the last computational cell before the backward facing step; and hence, contribute to the positive ξ_y distribution.

Another view of translational nonequilibrium is given by profiles of x and y translational temperature. These are translational temperatures associated with the x and y random molecular speeds and given by Eqns. 2.2, shown in Chapter 2. Figures 5.13 (a) and (b) illustrate the variation of translational and rotational temperatures at two distances above the flat plate surface. The profiles at $y = 0$ mm represent the computational cells within one mean-free-path of the flat plate and indicate there is considerable translational and rotational nonequilbrium. The translational nonequilibrium is demarcated by the differences among the total translational temperature, and the x and y translational temperatures. By definition, these temperatures are all equal for translational equilibrium. Ahead of the flat plate, $x < 0$, it is seen that the flow is essentially in translational equilibrium. As the molecules cross over the leading edge, translational and rotational nonequilibrium suddenly appear among them. In addition, the temperatures abruptly rise.

(a) $y = 0$ mm   (b) $y = 2.0$ mm
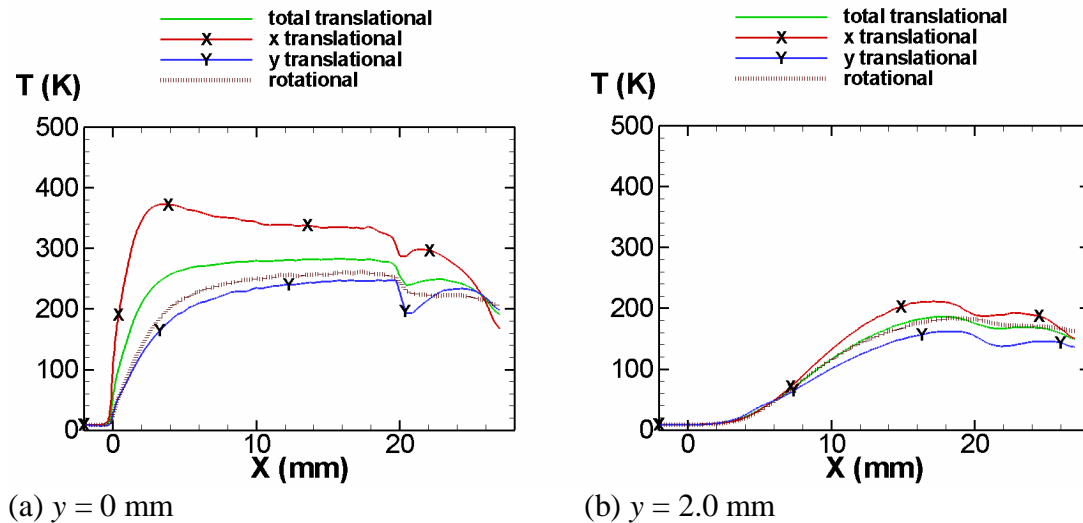
Figure 5.13 2D DSMC translational and rotational temperature profiles along x at two heights y above the flat plate using full gas-surface accommodation

The rise in temperatures is attributed to the much warmer surface temperature (300 K) than the freestream temperature ($\approx$ 9 K). Afterwards, the temperatures of the molecules near the surface approach the uniform flat plate temperature as they collide with additional scattered molecules. The rise in the translational nonequilibrium is attributed to collisions incurred by surface scattered molecules, as described above by the molecular velocity distributions. This causes the continued flow of molecules to experience a reduction in the mean molecular speed $\overline{\xi_x}$; hence, an increase in the random molecular speed $\xi'_x = \xi_x - \overline{\xi}_x$ and hence an increase in T_x. Since most of the flow momentum is directed along x, the change in the mean vertical molecular speed due to the scattered molecules is smaller; hence, a smaller increase in T_y occurs. The slower changes in rotational temperature than in the translational temperature is attributed to the slower rotational relaxation rate than the translational relaxation rate, predicted by quantum mechanics. The extent of the themal nonequilibrium is indicated by size of the differences in the component temperatures. Beyond the leading edge and diffuse shock, the thermal nonequilibrium steadily diminishes as the flow progresses further over the flat plate because of continued collisions and thus energy exchanges.

Further above the flat plate, as shown in Fig. 5.13 (b), rotational nonequilibrium does not appear significantly, however, translational nonequilibrium still appears, though to a lesser extent and with smoother changes. At y = 2.0 mm, the rise in translational nonequilibrium is due to the diffuse shockwave, located about 4.0 mm downstream of the leading edge because it is oblique. The effect of the backward facing step is diffused, while the extent of translational nonequilibrium appears frozen as gas blows past the flat plate.

The analysis of nonequilibrium now shifts to the examination of the vertical spatial variation at specified locations x. Consideration is again first given to the molecular velocity distributions. Figures 5.14 (a) and (b) present the evolution of molecular velocity distributions with y, at two positions along the plate, $x = 2.5$ and 20 mm, respectively.
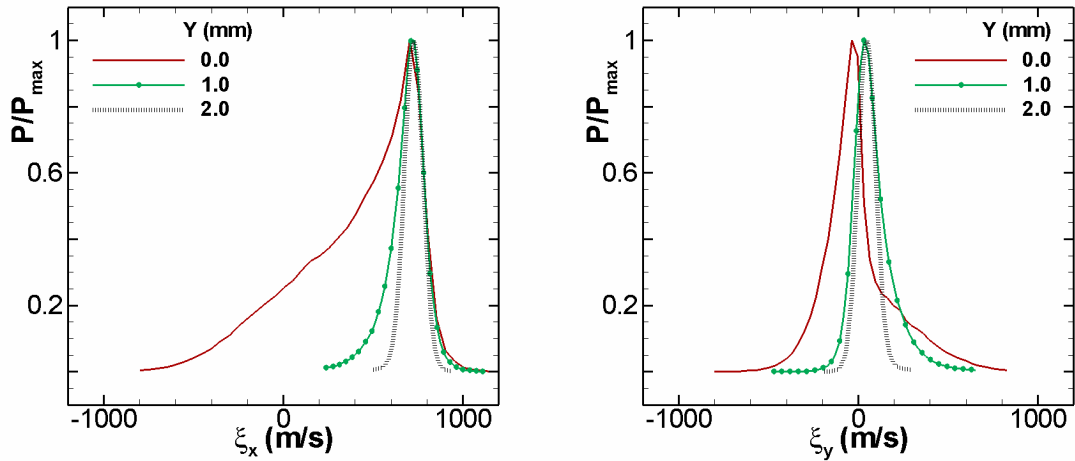
(a) *Simulated molecular velocity distribtutions of full accommodation at x = 2.5 mm*
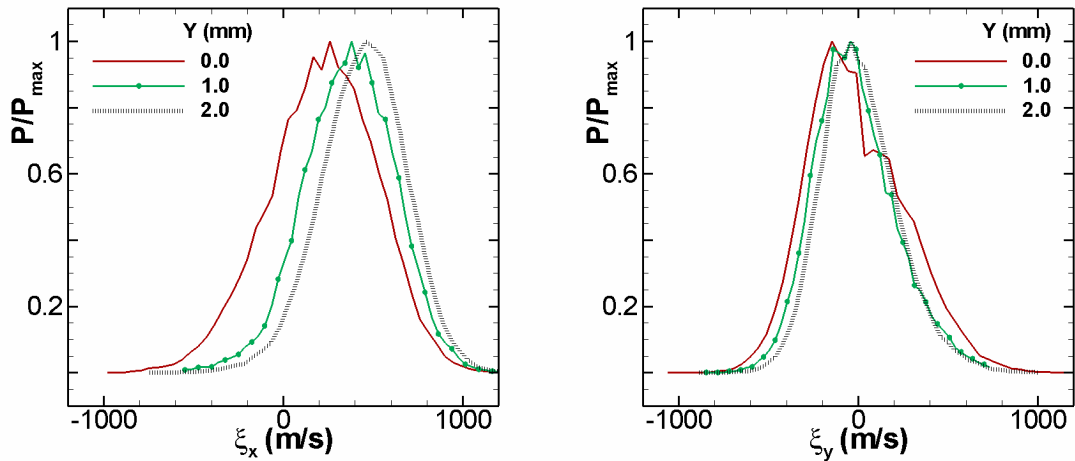
(b) *Simulated molecular velocity distribtutions of full accommodation at x = 20 mm*

Figure 5.14 2D DSMC spatial variation along y of molecular velocity probability distributions within boundary layer for full gas-surface accommodation

Three of the examined distributions are plotted. At $x = 2.5$ mm, both the ξ_x and ξ_y distributions evolve toward equilibrium as y increases. The rate of this evolution is greater than that of the ξ_x distributions with x along the surface, given the smaller increments in y, c.f. Fig. 5.12. This is expected because the presence of molecules reflected directly from the surface decreases with vertical distance from the surface. Table 5.7 (a) provides the corresponding statistics. Again, the number of samples reflects the gas density, and the percentage difference between the mean and most probable values reflects the level of translational nonequilibrium. Smaller values of percentage difference occur at $y \geq 1.0$ mm, where the distributions are near normal, for both the ξ_x and ξ_y distributions.

At $x = 20$ mm and $y = 0$ mm, the ξ_x distribution is already near normal. As y increases, the ξ_x distribution remains near normal, as shown in Fig. 5.14 (b) and Table 5.7 (b). In contrast, at $x = 20$ mm and $y = 0$ mm, the ξ_y distribution is skewed and has two peaks. The source of the two peaks are due to incident and reflected number fluxes and the

Table 5.7 **2D DSMC statistics of molecular velocity distributions at $x = 2.5$ and 20 mm for various values of y with full gas-surface accommodation**

x (mm)	No. of Samples	ξ_x S. D.[*]	Mean	M. P.[†]	% Diff[‡]	ξ_y S. D.	Mean	M. P.	% Diff
(a) $x = 2.5$ mm									
0	4,387,893	335.7	403.4	705.2	54.5	204.3	6.6	-35.5	290.1
0.3	6,540,059	250.3	540.9	713.9	27.6	171.2	40.9	2.4	177.7
0.5	8,533,708	189.4	599.6	706.2	16.3	148.4	69.9	21.0	107.7
1.0	9,800,428	118.6	668.7	729.7	8.7	116.7	81.6	33.7	82.9
2.0	7,946,681	57.8	733.5	730.8	1.1	59.7	52.0	48.4	7.2
(b) $x = 20$ mm									
0	1,255,890	299.3	217.1	258.7	17.5	273.3	-6.6	-147.5	182.9
0.3	1,304,345	274.8	281.5	228.8	20.7	260.8	-20.8	-108.7	135.8
0.5	1,346,391	269.3	311.0	319.4	2.7	250.8	-23.6	-67.5	93.4
1.0	1,385,069	255.9	365.5	382.2	4.5	234.2	-14.4	-4.2	110.3
2.0	1,741,867	237.9	444.8	457.5	2.8	215.6	12.5	-39.4	385.6

[*]standard deviation   [†]most probable value   [‡]percentage difference between Mean and M. P.

influence of the backward facing step, as previously described when discussing Fig. 5.12. At $y = 0.3$ mm, the skew is slightly reduced and the second peak disappears. By $y = 1.0$ mm, the ξ_y distributions are only slightly skewed, but has two peaks again. From $y = 0.5$ to 2.0 mm, the percentage difference between the mean and most probable values indicates an increase in nonequilibrium for the ξ_y distribution with y. This is explained by the deflection of the nearby bulk velocity streamlines and contours due to the backward facing step, that is, the end of the flat plate model, at $x = 20$ mm, illustrated in Fig. 5.5.

Finally, the associated temperature profiles are examined. Figures 5.15 (a) and (b) illustrate variation of translational and rotational temperatures with y at $x = 2.5$ and 20 mm. As expected, there is no significant nonequilibrium in the freestream above the boundary layer. At $x = 2.5$ mm, the distributions indicate that translational and rotational nonequilibrium gradually appears upon descent through the diffuse shock and becomes substantial upon approach to the surface. The temperature itself increases "exponentially" from the freestream above the diffuse shock to the surface because of the large difference between the freestream and flat plate surface temperature, and the high velocity of the flow. At $x = 20$ mm, Fig. 5.15 (b) shows no significant rotational nonequilibrium, however, it shows a slight amount of translational nonequilibrium, mostly in the y direction and with a gradual change in extent within the boundary layer. These observations agree with those of the horizontal temperature profiles, c.f. Fig. 5.13, and the molecular velocity distributions previously discussed. The cause of the translational nonequilbrium is again due to larger increases in ξ_x' than in ξ_y', and the cause of the rotational nonequilibrium is due to the slower rotational relaxation rate.

(a) $x = 2.5$ mm
(b) $x = 20$ mm
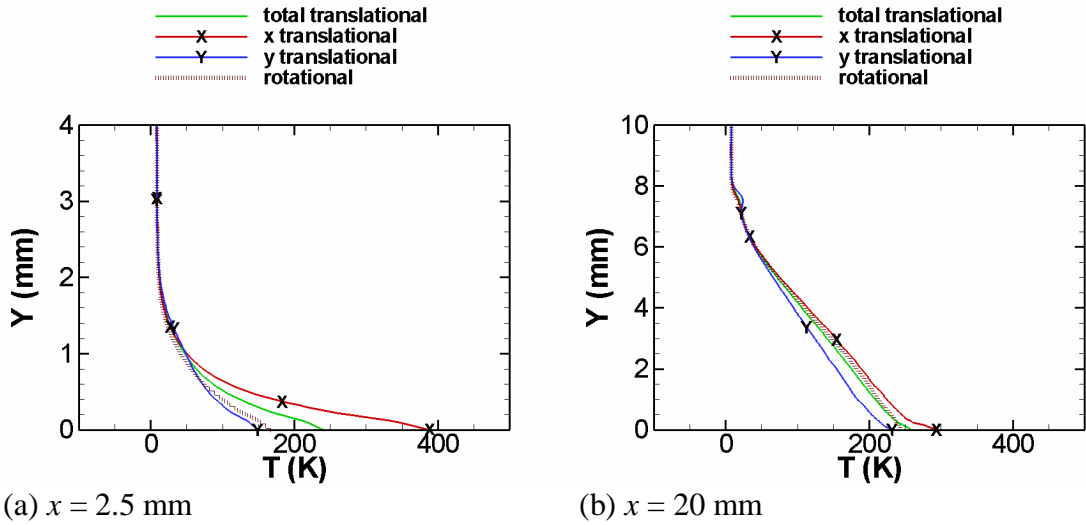
Figure 5.15 2D DSMC translational and rotational temperature profiles along y at two distances x from the flat plate leading edge using full gas-surface accommodation

In conclusion, translational and rotational nonequilibrium is found within the boundary layer. The translational nonequilibrium trends are consistent among the molecular velocity distribution statistics and distribution shape, and the translational temperature profiles. The molecular distributions reveal that the translational nonequilibrium is due to collisions with surface scattered molecules. The translational temperature distributions reveal that nonequilibrium occurs because of larger increases in ξ'_x than in ξ'_y due to the larger momentum along x. The rotational temperature distributions reveal that the rotational nonequilibrium agrees with the slower rotational relaxation rate than the translational relaxation rate. The greatest amount of nonequilibrium occurs within 10 local mean-free-paths from the leading edge and 1 local mean-free-path above the flat plate surface. Gradual evolution toward translational and rotational equilibrium occurs because of continued collisions in the undisturbed boundary layer.

5.6 Apollo 6 Flight Simulations Using the Two Models

The assessment of the Maxwell and CLL gas-surface interaction models by simulations of a flat plate windtunnel test enabled detailed, relatively inexpensive analysis and satisfactory comparison with real physical data. The assessment of the two models is completed here by applying them to a spaceflight application. The simulation set-up for the Apollo 6, 110 km entry trajectory point, provides an adequate framework for fulfilling this final part of the assessment. Therefore, the basic conditions described in Section 4.2 are employed. The isothermal wall condition defined in Section 4.3, which was determined to be adequate in Chapter 4, is selected. Case 3 of table 4.3 is repeated, forming two additional cases, denoted as cases 6 and 7, where the optimum values of a_M and σ_t found from the flat plate simulations are selected to place a connection with these simulations. Table 5.8 summarizes the two Apollo 6 flight simulation cases. In case 6, the levels of rotational and vibrational energy accommodation are equal and represented by the internal energy accommodation coefficient a_{E_int}. This coefficient is set equal to the Maxwell accommodation coefficient a_M, which governs the translational mode of molecular thermal energy. In case 7, a_{E_int} carries the same definition, however, in conjunction with the CLL model. The size of each simulation case is the same as listed in Table 4.2, in Chapter 4; however, in these cases, double the number of processors, 32 instead of 16, was used, resulting in nearly half the simulation time. The parallel efficiency of case 6 is about 98% based on the 16 processor runtime of 15 hr. The simulation wall time spent by each simulation is listed in Table 5.8. These wall times show that numerical expense of the CLL model is similar to that of the Maxwell model.

Note, because the wall times are dependent on the parallel computing system's communication efficiency during the time of simulation, these times are representative.

Table 5.8   **Apollo 6 flight simulation cases for assessing the two gas-surface interaction models using the isothermal wall temperature, $T_{w,i} = 830$ K**

Case	Gas-surface interaction model and accommodation	Simulation wall time
6	Maxwell, $a_M = 0.875$, $a_{E\_int} = 0.875$	7.68 hr
7	CLL, $\sigma_t = 0.875$, $\sigma_n = 1.000$, $a_{E\_int} = 0.875$	7.29 hr

The assessment of the gas-surface interaction models using space capsule reentry simulations begins with an examination of the translational temperature contours near the space capsule. Figures 5.16 (a) and (b) compare the contours that result from using the Maxwell and CLL gas-surface interaction models. The overall appearance of each contour plot is similar; however, in the compression region ahead of the vehicle, lower translational temperatures result from the CLL model. The changes in the peak
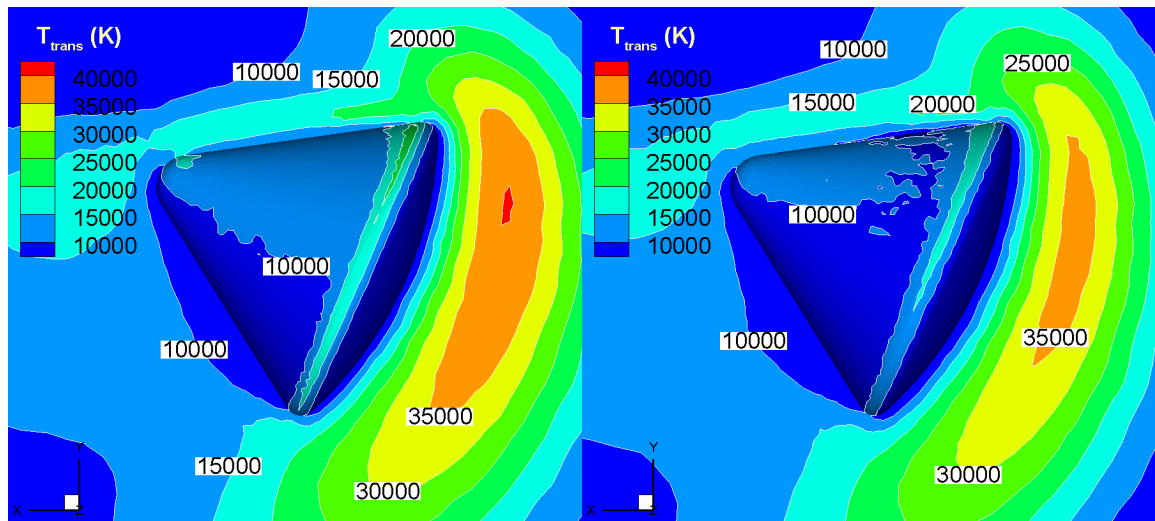
(a) Case 6 (Maxwell)   (b) Case 7 (CLL)

Figure 5.16   Contour plots of translational temperature at symmetry surface of three-dimensional Apollo 6 flight simulations using the Maxwell and CLL gas-surface interaction models

translational temperatures, as well as in the peak rotational and vibrational temperatures, are listed numerically in Table 5.9. There are slight effects on the peak field temperatures as a consequence of switching the gas-surface interaction model.

Table 5.9   Effects of gas-surface interaction models on maximum field temperatures found within compression region (K)

Case	*Translational*	*Rotational*	*Vibrational*
6 (Maxwell)	40,342	5,898	2,295
7 (CLL)	36,900	5,581	2,154
Increase	− 8.5 %	− 5.3 %	− 6.1 %

The differences in the peak field temperatures in the compression region are due to differences in the way each gas-surface interaction model scatters molecules. These differences are indicated by Figs. 5.17 (a) and (b), which are scattering plots from the flat plate windtunnel test simulations associated with a_M and $\sigma_t = 87.5\%$. The plots are of the non-normalized probability distributions. They indicate that the Maxwell model results in

(a) $x = 0$ mm   (b) $x = 5.0$ mm
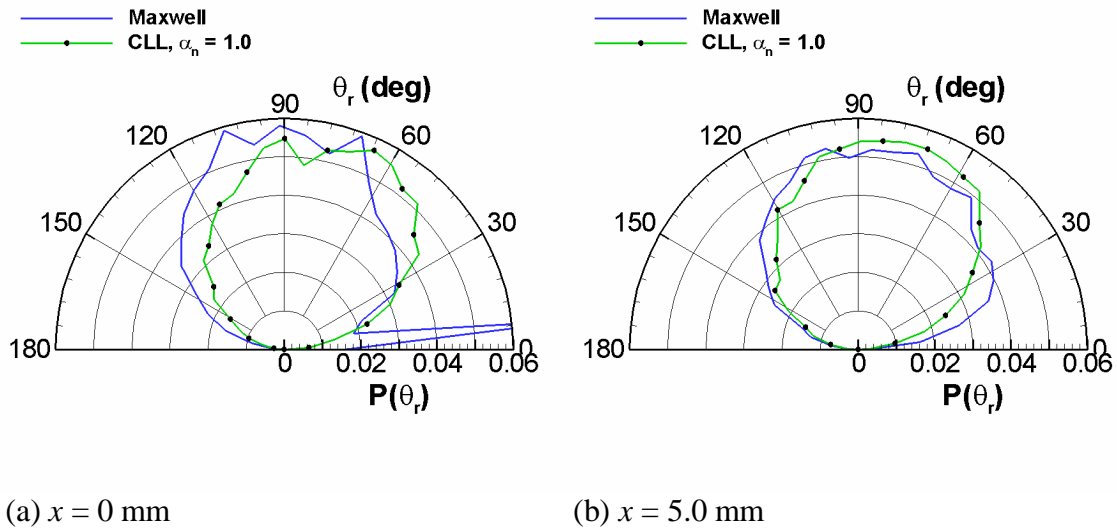
Figure 5.17   2D DSMC probability distributions of scattering angle at two locations on flat-plate surface, $y = 0$ mm, from windtunnel test simulations using a_M and $\sigma_t = 87.5\%$

greater backscatter, and thus, causes a wave of more energetic inter-gas collisions in the near field and the greater peak field temperatures in the compression region.

The assessment using these flight simulations concludes with an examination of the aerodynamics and surface heating. The associated data are listed in Table 5.10. Switching the gas-surface interaction models slightly affects drag and pitching moment. The pressure contribution to the pitching moment is slightly decreased and affected slightly more than the shear contribution. These contributions destructively interfere. Lift and Stanton number are affected to a much greater extent. The pressure and shear components of lift constructively interfere. Each is decreased to a similar extent. The range of effects is caused by the various differences in the gas-surface interaction models. Any one of these differences does not appear to stand out. These results further demonstrate the sensitivity of rarefied aerothermodynamic analysis to gas-surface interaction model; and thus, the merit of having the correct gas-surface interaction model for these conditions.

Table 5.10   Effects of gas-surface interaction models on aerodynamics and surface heating

Case	C_D	C_L	L/D	C_{MO}	St_{max}
6 (Maxwell)	1.68	0.266	0.158	0.113	0.746
pressure[*]	1.40	0.528		0.091	
shear	0.28	−0.261		0.021	
7 (CLL)	1.66	0.233	0.140	0.110	0.852
pressure	1.35	0.513		0.086	
shear	0.31	−0.280		0.024	
Increase (%)	− 1.4	− 12.5	− 11.3	− 2.6	14.3
pressure	−2.8	−5.5		−5.0	
shear	1.4	−6.9		2.4	

[*]pressure and shear components of C_D, C_L and C_{MO} are listed below the total values,
 percentage increases are relative to total values of case 6

5.7   Summary and Conclusions

This study began with a review of gas-surface interaction models since the Maxwell model. The review led to the decision to assess the Maxwell and the CLL gas-surface interaction models. These are two of the most commonly used models in use with DSMC. To examine the gas-surface interaction models, computational simulations were made of an existing windtunnel test study, performed by *Cecil and McDaniel* (2005), involving a free jet expansion of nitrogen used to generate rarefied hypersonic flow over a flat plate. They measured the velocity components, near the flat plate, with planar laser induced fluorescence (PLIF) of seeded iodine, within a nitrogen flow. A detailed study was made of the flat plate boundary layer flow, with MONACO simulations employing a nonuniform inflow condition emulating the windtunnel test.

Prior to embarking on the gas-surface interaction analysis, simulations of the windtunnel test flow near the flat plate were performed using continuum compressible boundary layer theory. These simulations demonstrated the necessity of using a kinetic computational approach to simulate the windtunnel test near equilibrium conditions by showing large differences in boundary layer velocity and temperature profiles between the continuum boundary layer theory and the DSMC method. Substantial differences in skin friction and Stanton number were also revealed between these computational approaches.

The second part of the DSMC study involved an assessment of the effects of the different gas-surface interaction models and of varying the gas-surface accommodation on the flat plate flow simulations. This was done by examining molecular distributions and boundary layer velocity profiles. For molecular velocity distributions, the Maxwell

145

and CLL gas-surface interaction models gave similar ξ_x distributions, but distinct ξ_y distributions, at partial levels of gas-surface accommodation. In addition, scattering distributions were examined. The Maxwell model resulted in distributions with unrealistic peaks due to specular reflection; whereas, the CLL model resulted in petal-shaped distributions, similar to observations of molecular beam studies, reported in the literature. Moreover, while the Maxwell scattering distributions experienced abrupt changes with increasing accommodation and position, the CLL distributions varied smoothly. Hence, for no significant additional cost, the CLL model gave more realistic scattering distributions. For boundary layer velocity profiles, the computed set of profiles encompassed the PLIF data, except for $x > 12.5$ mm, where an adverse pressure gradient appeared due to windtunnel test flow phenomena outside the specified computational domain. The Maxwell and CLL models gave the same boundary layer profiles at 50 to 100% gas-surface accommodation, based on Maxwell's fraction and CLL's tangential momentum accommodation coefficient. Finally, 90% gas-surface accommodation yielded the overall best agreement between the simulations and the PLIF data; this result is consistent with physical reasoning and the general trends found in the literature.

The study continued by examining the effects of the seeded iodine in the windtunnel tests. The corresponding DSMC computations were an order of magnitude more expensive than the pure nitrogen computations because the iodine mean-free-path was an order of magnitude smaller than the nitrogen mean-free-path due to the larger molecular weight and collision cross section of the iodine. The iodine velocity was very similar to the nitrogen velocity field, as expected from the $\sim 10^{-4}$ mixture ratio of iodine to nitrogen. Differences in the profiles are mainly due to the larger inertia of the seeded iodine and

partly explain differences in the pure nitrogen simulations and windtunnel test measurements. Because the overall differences are slight, the seeded iodine simulation affirms the pure nitrogen simulations and accredits the PLIF measurement procedure.

The fourth part of the study was an analysis of thermal nonequilibrium in the flow field. Translational and rotational nonequilibrium is found within the boundary layer. The translational nonequilibrium trends are consistent among the molecular velocity distribution statistics and distribution shape, and the translational temperature profiles. The molecular distributions reveal that the translational nonequilibrium is due to collisions with surface scattered molecules. The translational temperature distributions reveal that translational nonequilibrium occurs because of larger increases in random molecular speed parallel to the flat plate ξ'_x than random molecular speed perpendicular to the flat plate ξ'_y due to the larger momentum along the direction x parallel to the flat plate. The rotational temperature distributions reveal that the rotational nonequilibrium is consistent with the slower rotational relaxation rate than the translational relaxation rate. The greatest amount of nonequilibrium occurs within 10 mean-free-paths from the leading edge and 1 mean-free-path above the flat plate surface. Gradual evolution toward translational and rotational equilibrium occurs because of continued collisions in the undisturbed boundary layer.

The study concluded with an assessment of the gas-surface interaction models using Apollo 6 flight simulations. The simulations involved the conditions presented in Chapter 4 and the optimum Maxwell and CLL interaction parameters determined in Section 5.5.5. Maximum field temperatures and vehicle aerothermodynamic properties were examined. Significant differences between the simulations using the Maxwell and CLL models were

observed for the field temperatures, lift and Stanton number. These results further demonstrated the sensitivity of rarefied aerothermodynamic analysis to the gas-surface interaction model; and thus, the merit of having the correct gas-surface interaction model for these conditions.

CHAPTER VI

GENERAL SUMMARY AND FUTURE WORK

6.1   Overview

Motivated by escalating efforts to advance space transportation, computational simulation capabilities for rarefied and hypersonic flight conditions are becoming increasingly relevant. Among the few classes of computational approaches for examining rarefied gas dynamics, the most widely used approach, for spatial scales relevant to suborbital spaceflight, is the direct simulation Monte Carlo (DSMC) method. Although the DSMC method has been under development for over forty years, there are still many areas where improvements can be made. In the search for a definitive thesis goal and as a consequence of the analysis tools developed for achieving this goal, several aspects of DSMC analysis were examined beginning from the analysis of aerodynamic coefficients and culminating with the assessment of gas-surface interaction models, the associated numerical models of interactions between gas molecules and solid surfaces. To finalize this dissertation, the major results and conclusions are summarized here and suggestions for future work related to this research are proposed.

6.2   Summary of Results and Conclusions

In Chapter 3, the aerodynamic properties of drag, lift, pitching moment, and lift-to-drag ratio, of entry vehicle windtunnel test models within a hypersonic, rarefied nitrogen gas environment were analyzed using three-dimensional DSMC computations. Modified Newtonian and free molecular flow models were used to develop procedures to compute the aerodynamic properties computed by the MONACO DSMC code. The aerodynamic analysis procedures were applied to three dimensional simulations of windtunnel tests of a blunted cone and a small scale model of the Apollo Command Module. Good agreement was found between the measured and DSMC data of a blunted cone; however, this was not the case for the Apollo Command Module. Consequently, the possibility of discrepant Apollo windtunnel test measurements was examined by additional axisymmetric simulation studies. These simulations determined that freestream Mach number and reservoir conditions were measured with sufficient accuracy and that the test section flow could have been affected by windtunnel wall boundary layer interference. However, simulations including the windtunnel wall boundary are not possible because the available references [*Potter et al.* (1964), *Potter et al.* (1962)] do not provide sufficient details of the windtunnel geometry. In conclusion, aerodynamic integration procedures were validated and a sensitivity study suggested that the 1960's windtunnel results of the ACM are potentially affected by wall boundary layer interference, and have not been further analyzed in this thesis.

In Chapter 4, a sensitivity study was executed on the aerothermodynamics of the Apollo Command Module (ACM) at the 110 km entry trajectory point of the Apollo 6 mission. The study examined the significance of three physical mechanisms: gas-surface

150

accommodation, surface radiation and flow chemistry. To evaluate the effects of the changes in these physical mechanisms, Mach number contours, temperature contours, peak field temperatures, surface heating and aerodynamic coefficients were monitored. The first two mechanisms were examined by four simulation cases entailing two gas-surface accommodation conditions and two surface temperature conditions. To examine the sensitivity of the aerothermodynamics to flow chemistry, one of the inert simulations was rerun with MONACO chemistry procedures activated. The sensitivity study of the 110 km entry trajectory point of the Apollo 6 revealed that: changes in the gas-surface thermal accommodation significantly affect the aerothermodynamics; the addition of surface radiative equilibrium does not significantly affect the aerothermodynamics; and the inclusion of chemistry does not significantly affect the aerothermodynamics. Thus, because of the significance of gas-surface interactions found under these reentry conditions and because the behavior of gas-surface interactions under rarefied hypersonic conditions is not well understood, the research in this thesis was directed toward improving the understanding and simulation of gas-surface interactions under hypersonic rarefied conditions.

Chapter 5 began with a review of gas-surface interaction models since Maxwell. The review led to the decision to assess the Maxwell and the CLL gas-surface interaction models, which are two of the most commonly used models in use with DSMC. To examine the gas-surface interaction models, computational simulations were made of an existing windtunnel test study, performed by *Cecil and McDaniel* (2005), involving a free jet expansion of nitrogen used to generate rarefied hypersonic flow over a flat plate. They

measured the velocity components, near the flat plate, with planar laser induced fluorescence (PLIF) of seeded iodine, within a nitrogen flow.

A detailed study was made of the flat plate boundary layer flow, with MONACO simulations employing a nonuniform inflow condition emulating the windtunnel test. The study provided a detailed understanding of the effects of gas-surface interactions and seeded iodine on the velocity field, and of the thermal nonequilibrium within the boundary layer. First, 2D DSMC simulations provided good agreement with PLIF windtunnel test boundary layer velocity profiles, using a proper specification of gas-surface accommodation, with either the Maxwell or the CLL gas-surface interaction model; however, the CLL model is physically more realistic and has little additional computational expense. Second, the seeded iodine simulations affirmed the pure nitrogen simulations and the PLIF measurement procedures. Third, significant translational and rotational nonequilibrium near the surface and near the leading edge of the flat plate was found by observations of molecular velocity distribution statistics and distribution shape and by observations of translational and rotational temperature profiles. The molecular distributions revealed that the translational nonequilibrium was due to collisions with surface scattered molecules. The translational temperature distributions revealed that translational nonequilibrium occurred because of larger increases in random molecular speed parallel to the flat plate than random molecular speed perpendicular to the flat plate due to the larger momentum along the direction parallel to the flat plate. The rotational temperature distributions revealed that the rotational nonequilibrium was consistent with the slower rotational relaxation rate than the translational relaxation rate.

To conclude the assessment of the gas-surface interaction models, the Apollo 6 reentry condition at 110 km was revisited. Maximum field temperatures and vehicle aerothermodynamic properties were examined. Significant differences between the simulations using the Maxwell and CLL models were observed for the field temperatures, lift and Stanton number. These results further demonstrated the sensitivity of rarefied aerothermodynamic analysis to gas-surface interaction model; and thus, the merit of having the correct gas-surface interaction model for these conditions.

6.3   Suggestions for Future Work

The work presented in this thesis enlightened various areas for further research related to the computational simulation of transitional and rarefied gas dynamics experienced by spaceflight. Three general categories have been identified where further work can be made: program processing, gas-surface interactions and simulation studies involving comparisons with real physical data. Efforts that will provide progress in each of these areas are proposed here.

6.3.1 Program processing

To improve the program processing, two projects have been identified. These projects fall under the subcategories of parallel domain decomposition and grid generation. These may or may not be particular to the MONACO DSMC code. Currently, the parallel domain decomposition automatically assigns computational mesh regions to computer processors based on the number of simulation molecules in order to balance the load of simulation molecules among the processors. However, this single criterion does not minimize the communication load between processors. Consider a parallel simulation,

involving two processors, of a uniform gas flow through a right circular cylindrical computational mesh, as shown in Fig. 6.1 (a). The current criterion allows for the possibility of partition boundaries cutting through regions of large number flux between partitions, as shown in Fig. 6.1 (b). The large number flux leads to a large communication overhead between processors. The communication between processors can be reduced by optimizing the placement of partition boundaries such that the number flux between partitions is minimized throughout the computational domain. With the additional criterion, the partition boundaries in the example case would slice through the computational domain streamwise to the flow and parallel to the cylindrical wall, instead of across the flow streamlines and perpendicular to the cylindrical walls, as shown in Fig. 6.1 (c). In this case, if the freestream velocity $\mathbf{V}_\infty$ is much greater than the freestream most probable molecular speed $\xi'_{mp,\infty}$, then the streamwise partitioning scheme would

(a) Basic geometry   (b) Crosswise partitioning   (c) Streamwise partitioning
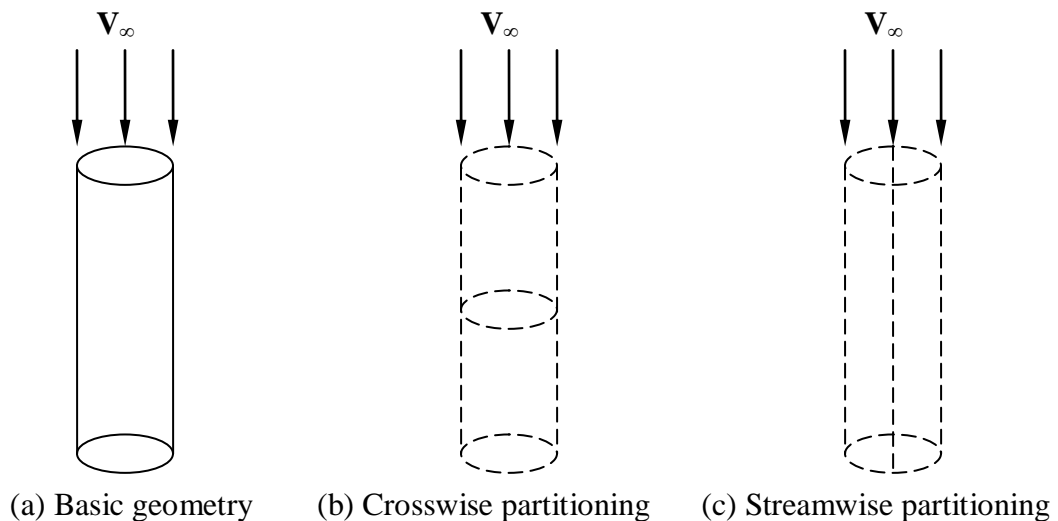
**Figure 6.1   Partitioning scheme for a parallel simulation involving two processors
for a uniform flow traversing a right circular cylindrical domain**

reduce the communication, provided that the total number flux across the interprocessor partition boundary for the streamwise partitioning scheme is less than for the crosswise scheme. This condition is generally met for rarefied hypersonic flow simulations; hence, minimizing communication based on number flux is applicable for DSMC simulations of rarefied hypersonic flow.

Regarding grid generation, there are three projects that can be addressed. These automatic grid adaptation, the degree of adaptation and automatic moving grid boundaries. As discussed in Chapter 2, the grid adaptation for the simulations reported in this thesis was performed manually. Manual adaptation was performed for the two-dimensional grids to avoid unpredictable convergence roadblocks with an in-house grid adaptation code when used with general geometries. Manual adaptation was performed for the three-dimensional grids because no three-dimensional grid adaptation code is available within the research group. Automatic grid adaptation reduces simulation set-up time and can result in better grid adaptation, particularly, for three-dimensional grids. Consequently, it is recommended that automatic grid adaptation capabilities be developed for two and three dimensional grids based on a more robust grid generation code than the presently available in-house grid generation code.

The degree of adaptation in DSMC is based on the criterion discussed in Chapter 2 that the computational cell size be no larger than the local-mean-free path. In regions of large macroscopic gradients, *Bird* (1994) generally recommends $\Delta s < \lambda / 3$ and $\Delta t \ll \tau$. Statistically this is sufficient. However, to satisfy any doubts it would be interesting to test whether further refinements produce any differences in the aerodynamic results of

windtunnel test or flight simulations. In this spirit, one may also perform sensitivity studies regarding the number of simulation molecules and the frequency of sampling.

Automatic moving grid boundaries are desired for simplifying grid generation for studies involving several slightly distinct simulations, such as multiple simulations of a flight vehicle at varying angle-of-attack. The angle-of-attack study would involve an initial domain boundary configuration, with the vehicle at zero angle-of-attack. Then, the vehicle surface would be rotated by a desired increment and the computational cells would be regenerated with a default pattern to provide initial results for grid adaptation for a second simulation, if necessary. This procedure could also be extended to simulate vehicle movements for dynamic stability studies.

6.3.2 Gas-surface interaction modeling

Six projects have been identified to improve the understanding and modeling of gas-surface interactions. First, the visualization of scattering distributions can be extended to three-dimensions. In order to do this with the MONACO DSMC code, the procedures to extract probability distributions must be modified to work for three-dimensional simulations because they currently only work with two dimensional simulations. This modification would also enable the visualization of three dimensional molecular velocity distributions. Second, the velocity extraction procedures can be extended to include the extraction of temperature and internal energy components. This would enable the visualization of temperature and energy distributions at specified points in space or along a solid surface for incident and reflected molecules. Third, the CLL model implemented into MONACO is the basic form. Extensions to this form are available [*Lord* (1991 and 1995)] and would enable additional case studies about the CLL model. These extensions

involve a broader range of translational energy accommodation conditions, rotational energy accommodation according to the form of the CL kernel, and vibrational energy accommodation according to a modified form of the CL kernel, which describes a discrete energy distribution. Fourth, an investigation on nonuniform distributions of gas-surface accommodation may lead to better agreement between DSMC and windtunnel boundary layer velocity profiles at all positions over the surface of interest. Fifth, existing gas-surface interaction models can be modified to handle the variation of accommodation with surface temperature or a new model can be introduced that inherently has this flexibility. Finally, existing gas-surface interaction models can be modified to handle the variation of accommodation with other surface properties, such as surface roughness and mean molecular spacing, or a new model can be introduced that inherently has these flexibilities.

6.3.3 Simulation studies involving comparisons with real physical data

The aerodynamic analysis studies of Chapter 3 serendipitously brought to attention potential errors in some of the hypersonic windtunnel test data from the 1960s. It is recommended that additional aerodynamic simulation analysis studies be performed when new rarefied hypersonic windtunnel test data of this kind becomes available. It is desired that extensive windtunnel geometry and flow conditions be acquired to enable comprehensive numerical simulation of the entire windtunnel test section.

Gas-surface interaction simulation studies would benefit from additional simple model configurations such as the flat plate study of *Cecil and McDaniel* (2005); see also *Seldon et al.* (2007). The flat plate windtunnel tests described in Chapter 5 provided field velocity data; however, field temperature data was not available, at least at the time when

the analysis was performed. Hence, it is desired to acquire field temperature laboratory data to also perform parametric studies involving the variation of boundary layer temperature profiles with gas-surface accommodation. In addition, it is desired to access velocity and temperature and/or energy molecular probability distribution data from future laboratory experiments. For gas-surface interaction modeling, it is particularly helpful to have available surface scattering probability distributions of velocity, temperature and energy. This would enable the most direct assessment of probability based gas-surface interaction models.

Gas-surface interaction simulation studies would also benefit from rarefied flight data programs. The Apollo 6 flight simulations in Chapters 4 and 5 involved a trajectory point suitable for a sensitivity study involving changes to physical models in the DSMC simulation. There are few public documents containing reentry trajectory data sufficient to produce a DSMC simulation. As usual, the Apollo 6 documents provided no aerodynamic flight data throughout the rarefied portion of the entry trajectory. Hence, data from other suborbital flight data collection programs are necessary in order to make comparisons between flight data and DSMC simulations using various gas-surface interaction conditions. Along with the benefit to Earth atmosphere spacecraft design, these comparisons are a step toward improving prediction capabilities of spaceflight near general atmosphere compositions. With continued exploration efforts to extraterrestrial atmospheres, such as the Martian atmosphere, the studies must be extended to incorporate the gas compositions of these atmospheres. Studies such as these would likely provide unique information or at least provide a check on similar studies performed elsewhere.

BIBLIOGRAPHY

BIBLIOGRAPHY

A. A. Agbormbai. A Statistical Theory for Gas Surface Interactions in Rarefied
Hypersonic Flows. I.C. Aero Report 88–01, Imperial College of Science and
Technology, London, 1988.

A. A. Agbormbai. Reciprocity Theory of Vibrationally Excited Many-Body Gas Surface
Interactions. *35th AIAA Thermophysics Conference*, AIAA Paper 2001-2964,
American Institute of Aeronautics and Astronautics, Reston, Virginia, 2001.

B. J. Alder and T. E. Wainwright. Molecular Dynamics by Electronic Computers.
*Proceedings of the International Symposium on Transport Processes in Statistical
Mechanics*, edited by I. Prigogine, Interscience Publishers, New York, pages 97–131,
1958.

D. A. Anderson, J. C. Tannehill and R. H. Pletcher. *Computational Fluid Mechanics and
Heat Transfer*. McGraw-Hill Book Company, New York, 1984.

J. D. Anderson. *Hypersonic and High Temperature Gas Dynamics*. McGraw-Hill Book
Company, New York, 1989.

J. J. Bertin. *Hypersonic Aerothermodynamics*. American Institute of Aeronautics and
Astronautics, Washington, District of Columbia, 1994.

G. A. Bird. Approach to Translational Equilibrium in a Rigid Sphere Gas. *Physics of
Fluids*, 6:1518–1519, 1963.

G. A. Bird. Monte Carlo Simulation of Gas Flows. *Annual Review of Fluid Mechanics*,
10:11–31, 1978.

G. A. Bird. Simulation of Multi-Dimensional and Chemically Reacting Flows.
Proceedings of the 11th International Symposium on Rarefied Gas Dynamics, edited
by R. Campargue, Commissariat a L'Energie Atomique, Paris, 1979.

G. A. Bird. Monte Carlo Simulation in an Engineering Context. *Progress in Aeronautics
and Astronautics*, Vol. 74, edited by S. S. Fisher, American Institute of Aeronautics
and Astronautics, New York, pages 239–255, 1981.

G. A. Bird. *Molecular Gas Dynamics and the Direct Simulation of Gas Flows*. Clarendon Press, Oxford, 1994.

G. A. Bird. Forty Years of DSMC, and Now? *Proceedings of the 22nd International Symposium on Rarefied Gas Dynamics*, edited by T. J. Bartel and M. A. Gallis, American Institute of Physics, Melville, New York, pages 372–380, 2001.

G. A. Bird. The DS2V/3V Program Suite for DSMC Calculations. *Proceedings of the 24th International Symposium on Rarefied Gas Dynamics*, edited by M. Capitelli, American Institute of Physics, Melville, New York, pages 541–546, 2005.

P. Bond. *The Continuing Story of the International Space Station*. Springer, New York, 2002.

L. Borgnakke and P. S. Larsen.Statistical Collision Model for Monte Carlo Simulation of Polyatomic Gas Mixture. *Journal of Computational Physics*, 18:405–420, 1975.

I. D. Boyd, G. C. Pham-Van-Diep and E. P. Muntz. Monte Carlo Computation of Nonequilibrium Flow in a Hypersonic Iodine Wind Tunnel. *AIAA Journal*, 32(5):964–970, 1994.

D. E. Boylan and B. J. Griffith. Simulation of the Apollo Command Module at Re-entry Altitudes. *Proceedings of the 3rd National Conference on Aerospace Meteorology*, American Meteorological Society, Boston, pages 370–378, 1968.

D. E. Boylan and J. L. Potter. Aerodynamics of Typical Lifting Bodies under Conditions Simulating Very High Altitudes. *AIAA Journal*, 5:226–232, 1967.

J. L. Brown. Turbulence Model Validation for Hypersonic Flows. *8th AIAA/ASME Joint Thermophysics and Heat Transfer Conference*, Institute of Aeronautics and Astronautics, Reston, Virginia, 2002.

J. M. Burt. *Monte Carlo Simulation of Solid Rocket Plumes at High Altitude*. Dissertation for Ph.D. (Aerospace Engineering), University of Michigan, Ann Arbor, 2006.

J. M. Burt. Post doctoral work, University of Michigan, Nov. 2006.

J. M. Burt and I. D. Boyd. Evaluation of a Particle Method for the Ellipsoidal Statistical Bhatnagar-Gross-Krook Equation. AIAA Paper 2006-989, *44th AIAA Aerospace Sciences Meeting and Exhibit*, American Institute of Aeronautics and Astronautics, Reston, Virginia, 2006.

P. Butterworth-Hayes. Space Tourism Race Speeds Up. *Aerospace America*, 45(8):4–6, 2007.

C. Cai. Private communication, March 2005.

F. Cajori. *Sir Isaac Newton's Mathematical Principles of Natural Philosophy and His System of the World*. University of California Press, Berkeley, 1934.

P. Cazin. French Space Plane Research, from Hermes to Transatmospheric Vehicles. AIAA Paper 89-5020, *1st AIAA National Aerospace Plane Conference*, American Institute of Aeronautics and Astronautics, Washington, District of Columbia, 1989.

D. E. Cecil and J. C. McDaniel. Private communication, March 2007.

D. E. Cecil and J. C. McDaniel. Planar Velocity and Temperature Measurements in Rarefied Hypersonic Flow Using Iodine LIF. *38th AIAA Thermophysics Conference*, AIAA Paper 2005-4695, American Institute of Aeronautics and Astronautics, Reston, Virginia, 2005.

C. Cercignani. Boundary Value Problems in Linearized Kinetic Theory. *SIAM-AMS Proceedings*, Vol. 1, edited by R. Bellman, G. Birkhoff, and I. Abu-Shumays, American Mathematical Society, Providence, Rhode Island, pages 249–268, 1969.

C. Cercignani. Scattering Kernels for Gas-Surface Interactions. *Transport Theory and Statistical Physics*, 2(1):27–53, 1972.

C. Cercignani. *Rarefied Gas Dynamics From Basic Concepts to Actual Calculations*. Cambridge University Press, Cambridge, England, 2000.

C. Cercignani and A. Frezzotti. Numerical Simulations of Supersonic Rarefied Gas Flows Past a Flat Plate: Effects of the Gas-Surface Interaction Model on the Flowfield. *Progress in Aeronautics and Astronautics*, Vol. 118, edited by E. P. Muntz, D. P. Weaver and D. H. Campbell, American Institute of Aeronautics and Astronautics, Washington, District of Columbia, pages 552–566, 1989.

C. Cercignani and M. Lampis. Kinetic Models for Gas-Surface Interactions. *Transport Theory and Statistical Physics*, 1(2):101–114, 1971.

C. Cercignani and M. Lampis. New Scattering Kernel for Gas-Surface Interaction. *AIAA Journal*, 35(6):1000–1011, 1997.

C. Cercignani, M. Lampis and A. Lentati. A New Scattering Kernel in Kinetic Theory of Gases. *Transport Theory and Statistical Physics*, 24(9):1319–1336, 1995.

P. E. Ceruzzi. *A History of Modern Computing*. 2nd Edition, The MIT Press, Cambridge, Massachusetts, 2003.

S. Chandrasekhar. *Newton's Principia for the Common Reader*. Oxford University Press, New York, 1995.

R. Chen, R. K. Argawal, F. G. Cheremisin and Y. Bondar. A Comparative Study of Navier-Stokes, Burnett, DSMC, and Boltzmann Solutions for Hypersonic Flow Past 2-D Bodies. AIAA Paper 2007-205, *45th AIAA Aerospace Sciences Meeting and Exhibit*, American Institute of Aeronautics and Astronautics, Reston, Virginia, 2007.

H. K. Cheng. Perspectives on Hypersonic Viscous Flow Research. *Annual Review of Fluid Mechanics*, 25:455–484, 1993.

H. K. Cheng and G. Emanuel. Perspective on Hypersonic Nonequilibrium Flow. *AIAA Journal*, 33(3):385–400, 1995.

P. Collins. The Coming Space Industry Revolution and Its Potential Global Impact. *Journal of Space Technology and Science*, 6(2):21–33, 1990.

S. R. Cook, M. A. Hoffbauer and J. B. Cross. Generating velocity and angular distribution functions of molecules scattered off of surfaces from measurements of forces exerted on surfaces by incident gases. *19th AIAA Advanced Measurement and Ground Testing Technology Conference*, AIAA Paper 96–2227, American Institute of Aeronautics and Astronautics, Reston, Virginia, 1996.

S. F. de Córdoba. 100 km. Altitude Boundary for Astronautics…, http://www.fai.org:81/astronautics/100km.asp, 2004.

P. Coue. The Beginning of Hermes Spaceplane (1976-1985). *54th International Astronautical Congress*, IAC-03-IAA.2.P.02, International Astronautical Federation, Paris, France, 2003.

R. N. Cox. General Characteristics of Hypersonic Flow Fields. *Journal of the Royal Aeronautical Society*, 63:503–508, 1959.

R. S. Crowder and J. D. Moote. Apollo Entry Aerodynamics. *Journal of Spacecraft*, 6(3):302–307, 1969.

H. M. Deitel and P. J. Deitel. *C How to Program*. Prentice Hall, Upper Saddle River, New Jersey, 2001.

D. DePasquale, A. C. Charania and J. R. Olds. The Emerging Orbital Space Tourism Industry: New Insight into Demand and Prospects for Success. *AIAA Space 2006 Conference*, AIAA Paper 2006-7478, American Institute of Aeronautics and Astronautics, Reston, Virginia, 2006.

R. W. Detra, N. H. Kemp and F. R. Riddell. Addendum to Heat Transfer to Satellite Vehicles Reentering the Atmosphere. *Jet Propulsion*, 27(12):1256–1257, 1957.

S. Dietrich and I. D. Boyd. Scalar and Parallel Optimized Implementation of the Direct Simulation Monte Carlo Method. *Journal of Computational Physics*, 126:328–342, 1996.

Engineering Village, Elsevier Information, http://www.ei.org, New York, 2007.

P. S. Epstein. On the Air Resistance of Projectiles. *Proceedings of the National Academy of Sciences of the United States of America*, 17(9):532–547, 1931.

J. A. Fay and F. R. Riddell. Theory of Stagnation Point Heat Transfer in Dissociated Air. *Journal of the Aeronautical Sciences*, 25(2):73–85 and 121, 1958.

Fédération Aéronautique Internationale (FAI). Sporting Code, Section 8 Astronautics, Switzerland, 2003.

N. C. Freeman. Non-equilibrium Flow of an Ideal Dissociating Gas. *Journal of Fluid Mechanics*, 4(4):407–425, 1958.

T. I. Gombosi. *Gaskinetic Theory*. Cambridge University Press, Cambridge, England, 1994.

B. J. Griffith. Comparison of Data from the Gemini Flights and AEDC-VKF Wind Tunnels. *AIAA 5th Aerospace Sciences Meeting*, AIAA Paper 67-166, American Institute of Aeronautics and Astronautics, New York, Jan. 1967.

B. J. Griffith. Comparison of Aerodynamic Data from the Gemini Flights and AEDC-VKF Windtunnels. *Journal of Spacecraft*, 4(7):919–924, July 1967.

B. J. Griffith and D. E. Boylan. Reynolds and Mach Number Simulation of Apollo and Gemini Re-entry and Comparison with Flight. *Specialists' Meeting on Hypersonic Boundary Layers and Flow Fields of the Fluid Dynamics Panel of AGARD*, North Atlantic Treaty Organization, Paris, pages 8-1–8-21, 1968.

K. Grinter. Apollo Program. http://www-pao.ksc.nasa.gov/kscpao/history/apollo/apollo.htm, 2005.

W. D. Hayes and R. F. Probstein. *Hypersonic Flow Theory*. Academic Press, New York, 1959.

W. D. Hayes and R. F. Probstein. *Hypersonic Flow Theory*. 2nd Edition, Academic Press, New York, 1966.

B. L. Haas and I. D. Boyd. Models for Direct Monte Carlo Simulation of Coupled Vibration-Dissociation. *Physics of Fluids A*, 5(2):478–489, 1993.

S. J. Henderson and J. A. Menart. Adding Chemical Equilibrium to a Parallel, Unstructured Euler/Navier-Stokes Flow Solver. AIAA Paper 2006-3736, *36th AIAA Fluid Dynamics Conference and Exhibit*, American Institute of Aeronautics and Astronautics, Reston, Virginia, 2006.

T. A. Heppenheimer. The Space Shuttle Decision NASA's Search for a Reusable Space Vehicle. NASA SP-4221, National Aeronautics and Space Administration, Washington, District of Columbia, 1999.

E. R. Hillje. Entry Flight Aerodynamics from Apollo Mission AS-202. NASA TN D-4185, National Aeronautics and Space Administration, Washington, District of Columbia, 1967.

E. R. Hillje and R. Savage. Status of Aerodynamic Characteristics of the Apollo Entry Configuration. *AIAA Entry Vehicle Systems and Technology Meeting*, AIAA Paper 68-1143, American Institute of Aeronautics and Astronautics, New York, 1968.

J. J. Hinchen and W. M. Foley. Scattering of Molecular Beams by Metallic Surfaces. *Proceedings of the 4th International Symposium on Rarefied Gas Dynamics*, Vol. 2, edited by J. H. de Leeuw, Academic Press, New York, pages 505–517,1966.

C. Hirsch. *Numerical Computation of Internal and External Flows*. 2nd Edition, Elsevier, Burlington, Massachusetts, 2007.

F. C. Hurlbut. Two Contrasting Modes for the Description of Wall-Gas Interactions. *Progress in Astronautics and Aeronautics*, Vol. 158, edited by B. D. Shizgal and D. P. Weaver, American Institute of Aeronautics and Astronautics, Washington, District of Columbia, pages 494–506, 1992.

F. C. Hurlbut and F. S. Sherman. Application of the Nocilla Wall Reflection Model to Free-Molecule Kinetic Theory. *Physics of Fluids*, 11(3):486–496, 1968.

HyperMesh. Version 7.0, Altair Engineering Inc., Troy, Michigan, 2004.

M. S. Ivanov and S. F. Gimelshein. Computational Hypersonic Rarefied Flows. *Annual Review of Fluid Mechanics*, 30:469–505, 1998.

E. Josyula and W. F. Bailey. Vibration-Dissociation Coupling Using Master Equations in Nonequilibrium Hypersonic Blunt-Body Flow. *Journal of Thermophysics and Heat Transfer*, 15(2): 157–167, 2001.

K. C. Kannenberg and I. D. Boyd. Development of an Object-Oriented Parallel DSMC Code for Plume Impingement Studies. *30th AIAA Thermophysics Conference*, AIAA Paper 95-2052, American Institute of Aeronautics and Astronautics, Washington, District of Columbia, 1995.

B. W. Kernighan and D. M. Ritchie. *The C Programming Language*. Prentice Hall, Englewood Cliffs, New Jersey, 1988.

A. D. Ketsdever and E. P. Muntz. Gas-Surface Interaction Model Influence on Predicted Performance of Microelectromechanical System Resistojet. *Journal of Thermophysics and Heat Transfer*, 15(3):302–307, 2001.

E. D. Knechtel and W. C. Pitts. Experimental Momentum Accommodation on Metal Surfaces of Ions Near and Above Earth-Satellite Speeds. *Proceedings of the 6th International Symposium on Rarefied Gas Dynamics*, Vol. 2, edited by L. Trilling and H. Wachman, Academic Press, New York, pages 1257–1278, 1969.

K. Koura and H. Matsumoto. Variable Soft Sphere Molecular Model for Air Species. *Physics of Fluids*, 4:1083–1085, 1992.

I. Kuščer. Reciprocity in Scattering of Gas Molecules by Surfaces. *Surface Science*, 25:225–237, 1971.

D. B. Lee and W. D. Goodrich. The Aerothermodynamic Environment of the Apollo Command Module During Superorbital Entry. NASA TN D-6792, 1972.

L. Lees. Hypersonic Flow. *Proceedings of the 5th International Aeronautical Conference*, Institute of the Aeronautical Sciences, Los Angeles, pages 241–276, 1955.

D. R. Lide, editor. *CRC Handbook of Chemistry and Physics*, Internet Version 2007 (87th Edition), <http:/www.hbcpnetbase.com>, Taylor and Francis, Boca Raton, Florida, 2007.

A. Linan and I. Da Riva. Chemical Nonequilibrium Effects in Hypersonic Aerodynamics. ICAS PAPER 32, *3rd International Council of the Aeronautical Sciences*, Stockholm, Sweden, 1962.

R. G. Lord. Application of the Cercignani-Lampis Scattering Kernel to Direct Simulation Monte Carlo Calculations. *Proceedings of the 17th International Symposium on Rarefied Gas Dynamics*, edited by A. E. Beylich, VCH, Weinheim, Germany, pages 1427–1433, 1991.

R. G. Lord. Some Extensions to the Cercignani-Lampis Gas-Surface Scattering Kernel. *Physics of Fluids A: Fluid Dynamics*, 3(4):706–710, 1991.

R. G. Lord. Some Further Extensions of the Cercignani-Lampis Gas-Surface Interaction Model. *Physics of Fluids*, 7(5):1159–1161, 1995.

MathCad 8 Professional. MathSoft Inc., Cambridge, Massachussetts, 1998.

J. C. Maxwell. On Stresses in Rarified Gases Arising from Inequalities of Temperature. *Philosophical Transactions of the Royal Society of London*, 170:231–256, 1879.

R. A. Millikan. Coefficients of Slip in Gases and the Law of Reflection of Molecules from the Surfaces of Solids and Liquids. *The Physical Review*, 21(3):217–238, 1923.

T. K. Minton, M. Tagawa and G. M. Nathanson. Energy Accommodation in Hyperthermal Gas-Surface Collisions: Aerobraking in Planetary Atmospheres. *Journal of Spacecraft and Rockets*, 41(3):389–396, 2004.

K. Moe. Satellite Drag Coefficients at 150 to 500 km. *Advances in the Astronautical Sciences*. 119(2):1197–1206, 2005.

K. Moe, M. M. Moe and S. D. Wallace. Improved Satellite Drag Coefficient Calculations from Orbital Measurements of Energy Accommodation. *Journal of Spacecraft and Rockets*, 35(3):266–272, 1998.

J. N. Moss. Private communication, Dec., 2005.

J. N. Moss, C. E. Glass and F. A. Greene. DSMC Simulations of Apollo Capsule Aerodynamics for Hypersonic Rarefied Conditions. *9th AIAA/ASME Joint Thermophysics and Heat Transfer Conference*, AIAA Paper 2006-3577, American Institute of Aeronautics and Astronautics, Reston, Virginia, 2006.

Ch. Mundt. Calculation of Hypersonic, Viscous, Non-equilibrium flows around Reentry Bodies Using a Coupled Boundary Layer/Euler Method. AIAA Paper 92-2856. *AIAA 27th Thermophysics Conference*, American Institute of Aeronautics and Astronautics, Washington, District of Columbia, 1992.

R. D. Neumann. Defining the Aerothermodynamic Methodology. *Hypersonics, Volume I: Defining the Hypersonic Environment*, edited by J. J. Bertin, R. Glowinski, and J. Periaux, Birkäuser Boston, Boston, Massachussetts, 1989.

S. Nocilla. On the Interaction between Stream and Body in Free-Molecule Flow. *Proceedings of the 2nd International Symposium on Rarefied Gas Dynamics*, edited by L. Talbot, Academic Press, New York, pages 169–208, 1961.

S. Nocilla. The Surface Re-Emission Law in Free Molecule Flow. *Proceedings of the 3rd International Symposium on Rarefied Gas Dynamics*, Vol. 2, edited by J. A. Laurmann, Academic Press, New York, pages 327–346, 1963.

C. Ollivier-Gooch. *GRUMMP Version 0.3.0 User's Guide*. Department of Mechanical Engineering, University of British Columbia, Vancouver, 2005.

E. S. Oran, C. K. Oh and B. Z. Cybyk, Direct Simulation Monte Carlo: Recent Advances and Applications. *Annual Review of Fluid Mechanics*, 30:403–441, 1998.

S. Owen. A Survey of Unstructured Mesh Generation Technology. http://www.andrew.cmu.edu/user/sowen/survey/index.html, 2007.

C. Park. *Nonequilibrium Hypersonic Aerothermodynamics*. Wiley, New York, 1990.

P. Pesavento. Russian Space Shuttle Projects 1957-1994. *Spaceflight*, 37:226, 1995.

J. M. Picone, A. E. Hedin, D. P. Drob and A. C. Aikin, NRLMSISE-00 Emperical Model of the Atmosphere: Statistical Comparisons and Scientific Issues. *Journal of Geophysical Research*, 107(A12):SIA 15-1–SIA 15-16, 2002.

S. B. Pope. *Turbulent Flows*. Cambridge University Press, New York, 2000.

J. L. Potter, G. D. Arney Jr., W. H. Carden and M. Kinslow. Gasdynamic Diagnosis of High-Speed flows Expanded from Plasma States. *IEEE Transactions on Nuclear Science*, NS-11(1):145–157, 1964.

J. L. Potter, G. D. Arney Jr., W. H. Carden and M. Kinslow. Irreversible Flow in Reservoir and Throat Sections of Wind Tunnels with Constricted-Arc Heaters. *Proceedings of AGARD Fluid Dynamics Panel Specialists' Meeting*, AGARDograph 84, Technical Editing and Reproduction Ltd., London, pages 379–412, 1964.

J. L. Potter, M. Kinslow, G. D. Arney Jr. and A. B. Bailey. Initial Results from a Low-Density Hypersonic Wind Tunnel. *Progress in Astronautics and Rocketry: Hypersonic Flow Research*, Vol. 7, edited by F. R. Riddell, Academic Press, New York, pages 599–624, 1962.

A. Poukhov. Russian Aerospace Plane TU-2000. AIAA Paper 93-5055, *AIAA/DGLR 5th International Aerospace Planes and Hypersonics Technologies Conference*, American Institute of Aeronautics and Astronautics, Washington, District of Columbia, 1993.

Pro/ENGINEER Wildfire. Version 2.0, Parametric Technology Coorporation, Needham, Massachussetts, 2004.

M. J. Quinn. *Parallel programming in C with MPI and OpenMP*. McGraw-Hill, Boston, 2004.

M. Rasmussen. *Hypersonic Flow*. Wiley, New York, 1994.

R. Reagan. State of the Union Address, Feb. 4, 1986.

F. Rogier and J. Schneider. A Direct Method for Solving the Boltzmann Equation. *Transport Theory and Statistical Physics*, 23(1-3):313–338, 1994.

C. J. Roy and F. G. Blottner. Review and Assessment of Turbulence Models for Hypersonic Flows: 2D/Axisymmetric Cases. AIAA Paper 2006-713, *44th Aerospace Sciences Meeting and Exhibit*, American Institute of Aeronautics and Astronautics, Reston, Virginia, 2006.

W. F. N. Santos. Influence of Gas-Surface Interaction on Hypersonic Aerothermodynamic Performance of Flat-Nose Power-Law Bodies. *44th AIAA Aerospace Sciences Meeting and Exhibit*, AIAA Paper 2006-1194, American Institute of Aeronautics and Astronautics, Reston, Virginia, 2006.

L. C. Scalabrin. Private communication, July, 2007.

S. A. Schaaf. Mechanics of Rarefied Gases. *Encyclopedia of Physics: Fluid Dynamics II*, Vol. 8, edited by S. Flűgge and C. Truesdell, Springer-Verlag, Berlin, pages 591–624, 1963.

S. A. Schaaf and P. L. Chambré. *Flow of Rarefied Gases*. Princeton University Press, Princeton, New Jersey, 1961.

R. Schamberg. A New Analytic Representation of Surface Interaction for Hyperthermal Free-Molecule Flow with Application to Satellite Drag. *Proceedings of the Heat Transfer and Fluid Mechanics Institute*, Stanford University Press, Palo Alto, California, pages 1–14, 1959.

T. E. Schwartzentruber. *A Modular Particle-Continuum Numerical Algorithm for Hypersonic Non-equilibrium Flows*. Dissertation for Ph.D. (Aerospace Engineering), University of Michigan, Ann Arbor, 2007.

T. E. Schwartzentruber, L. C. Scalabrin and I. D. Boyd. A Modular Particle–Continuum Numerical Method for Hypersonic Non-Equilibrium Gas Flows. *Journal of Computational Physics*, 225(1):1159–1174, 2007.

N. Seldon, C. Ngalande, S. Gimelshein and A. Ketsdever. Experimental Compuatational Observation of Radiometric Forces on a Plate. *39th AIAA Thermophysics Conference*, AIAA Paper 2007-4403, American Institute of Aeronautics and Astronautics, Reston, Virginia, 2007.

L. H. Sentman. *Free Molecule Flow Theory and Its Application to the Determination of Aerodynamic Forces*. LMSC-448514, Lockheed Missiles and Space Co., Sunnyvale, California, 1961.

F. Sharipov. Application of the Cercignani-Lampis Scattering Kernel to Channel Gas Flows. *Proceedings of the 22nd International Symposium on Rarefied Gas Dynamics*, edited by T. J. Bartel and M. A. Gallis, American Institute of Physics, Melville, New York, pages 347–353, 2001.

Q. Sun. *Information Preservation Methods for Modeling Micro-Scale Gas Flows*. Dissertation for Ph.D. (Aerospace Engineering), University of Michigan, Ann Arbor, 2003.

Tecplot. Version 10.0, Tecplot Inc., Bellevue, Washington, 2004.

J. F. Thompson. National Grid Project. *Computing Systems in Engineering*, 3(1–4):393–399, 1992.

N. Tsuboi and Y. Matsumoto. DSMC Simulation with Gas-Surface Interaction Models in Hypersonic Rarefied Flow. *Proceedings of the 22nd International Symposium on Rarefied Gas Dynamics*, edited by T. J. Bartel and M. A. Gallis, American Institute of Physics, Melville, New York, pages 331–338, 2001.

S. Utah and H. Arai. Monte Carlo Simulation of Reentry Flows Based Upon a Three-Temperature Model. *Proceedings of the 23rd International Symposium on Space Technology and Science*, Vol. 1, Japan Society for Aeronautical and Space Sciences, Tokyo, pages 1209–1214, 2002.

P. Vijayakumar, Q. Sun and I. D. Boyd. Detailed Models of Vibrational-Translational Energy Exchange for the Direct Simulation Monte Carlo Method. *Physics of Fluids*, 11(8):2117–2126, 1999.

W. G. Vincenti and C. H. Kruger, Jr. *Introduction to Physical Gas Dynamics*. Krieger Publishing Company, Malabar, Florida, 1965.

W. L. Wang. *A Hybrid Particle/Continuum Approach for Nonequilibrium Hypersonic Flows*. Dissertation for Ph.D. (Aerospace Engineering), University of Michigan, Ann Arbor, 2004.

W. L. Wang and I. D. Boyd. Predicting Continuum Breakdown in Hypersonic Viscous Flows. *Physics of Fluids*, 15(1):2003.

E. P. Wenaas. Equilibrium Cosine Law and Scattering Symmetry at the Gas-Surface Interface. *The Journal of Chemical Physics*, 54(1):376–388, 1971.

F. M. White. *Viscous Fluid Flow*. 2nd Edition, McGraw-Hill, New York, 1991.

J. D. Whitfield and B. J. Griffith. Hypersonic Viscous Drag Effects on Blunt Slender Cones. *AIAA Journal*, 2(10):1714–1722, 1964.

J. Wilson, editor. The Vision for Space Exploration. National Aeronautics and Space Administration, http://www.nasa.gov/mission_pages/exploration/main/index.html, 2007.

J.-S. Wu, K.-C. Tseng and C.-H. Kuo. Application of Local Mesh Refinement in the DSMC Method. *Proceedings of the 22nd International Symposium on Rarefied Gas Dynamics*, edited by T. J. Bartel and M. A. Gallis, American Institute of Physics, Melville, New York, pages 417–425, 2001.

X PRIZE Foundation. Ansari X PRIZE, http://www.xprize.org/xprizes/ansari_x_prize.html, Santa Monica, California, 2006.

N. Yamanishi, Y. Matsumoto and K. Shobatake. Multistage Gas-Surface Interaction Model for the Direct Simulation Monte Carlo Method. *Physics of Fluids*, 11(11):3540–3552, 1999.

S. M. Yen. Numerical Solution of the Nonlinear Boltzmann Equation for Nonequilibrium Gas Flow Problems. *Annual Review of Fluid Mechanics*, 16:67–97, 1984.